



Cite this: *Chem. Soc. Rev.*, 2023, 52, 3873

# Recent progress in the development of fluorescent probes for imaging pathological oxidative stress

Yujie Geng,<sup>a</sup> Zhuo Wang,<sup>id</sup> <sup>\*</sup>a Jiaying Zhou,<sup>a</sup> Mingguang Zhu,<sup>a</sup> Jiang Liu<sup>a</sup> and Tony D. James<sup>id</sup> <sup>\*</sup>bc

Oxidative stress is closely related to the physiopathology of numerous diseases. Reactive oxygen species (ROS), reactive nitrogen species (RNS), and reactive sulfur species (RSS) are direct participants and important biomarkers of oxidative stress. A comprehensive understanding of their changes can help us evaluate disease pathogenesis and progression and facilitate early diagnosis and drug development. In recent years, fluorescent probes have been developed for real-time monitoring of ROS, RNS and RSS levels *in vitro* and *in vivo*. In this review, conventional design strategies of fluorescent probes for ROS, RNS, and RSS detection are discussed from three aspects: fluorophores, linkers, and recognition groups. We introduce representative fluorescent probes for ROS, RNS, and RSS detection in cells, physiological/pathological processes (e.g., Inflammation, Drug Induced Organ Injury and Ischemia/Reperfusion Injury etc.), and specific diseases (e.g., neurodegenerative diseases, epilepsy, depression, diabetes and cancer, etc.). We then highlight the achievements, current challenges, and prospects for fluorescent probes in the pathophysiology of oxidative stress-related diseases.

Received 27th February 2022

DOI: 10.1039/d2cs00172a

rsc.li/chem-soc-rev

## 1. Introduction

The oxidation–reduction process covers the basic process of almost all life functions from bioenergy to metabolism, so the oxidation–reduction homeostasis is very important for ensuring good health.<sup>1</sup> In general, physiological levels of oxidants/reducing agents are important as redox signals, which are essential for maintaining a healthy body. However, excessive

<sup>a</sup> State Key Laboratory of Chemical Resource Engineering, College of Chemistry, Beijing Advanced Innovation Center for Soft Matter Science and Engineering, Beijing University of Chemical Technology, Beijing, 100029, China.  
E-mail: wangzhuo77@mail.buct.edu.cn

<sup>b</sup> Department of Chemistry, University of Bath, Bath BA2 7AY, UK.  
E-mail: t.d.james@bath.ac.uk

<sup>c</sup> School of Chemistry and Chemical Engineering, Henan Normal University, Xinxiang 453007, China



Yujie Geng

Yujie Geng received his BS degree in chemistry from Henan University of Technology in 2017. He is pursuing his PhD degree in chemistry under the supervision of Prof. Zhuo Wang in Beijing University of Chemical Technology. His current research interests are in the development of new fluorescent probes for brain imaging and sensing analytes.



Zhuo Wang

Zhuo Wang is Professor at the College of Chemistry in Beijing University of Chemical Technology. Her research interests include the design and synthesis of organic functional molecules for bio-imaging and bio-analysis, and organic-nano composite materials for disease treatment. She has received several prestigious awards for young career investigators including the Excellent Young Scientist Foundation of NSFC, AMS-NSFC Newton Advanced Fellowship, Lu Jiaxi Young Talent Award from CAS, Beijing Science and Technology Award.



levels of oxidants can destroy biological molecules (such as deoxyribose, nucleic acids, proteins, lipids, *etc.*) causing oxidative damage and signal disturbances,<sup>2,3</sup> which could potentially induce serious diseases (Fig. 1). Generally, the excessive production of oxidants and the serious imbalance of antioxidant consumption in organisms are collectively referred to as oxidative stress.<sup>4</sup> Reactive oxygen species (ROS) and reactive nitrogen (RNS) are the two most important types of oxidants in the human body. They can be produced through a variety of endogenous and exogenous processes, and the negative effects are generally counteracted by reactive sulfur species (RSS), thereby forming a special redox homeostasis in the body (Fig. 1).<sup>5,6</sup>

Normal physiological activities in organisms or external stimuli will induce the production of free radicals, which are highly active molecules or species.<sup>7</sup> Free radicals possess a single or multiple unpaired electrons in the valence (outermost) electronic orbitals. When these unpaired electrons meet with oxygen molecules/nitric oxide in the organism, ROS/RNS will be generated. Therefore, ROS and RNS (RONS) refer to reactive radicals and non-radical derivatives of oxygen and nitrogen,

respectively.<sup>8,9</sup> It is generally believed that reactive oxygen species specifically include superoxide anion ( $\text{O}_2^{\bullet-}$ ), hydrogen peroxide ( $\text{H}_2\text{O}_2$ ), ozone ( $\text{O}_3$ ), singlet oxygen ( $^1\text{O}_2$ ), alkoxyl ( $\text{RO}^\bullet$ ), lipid peroxy radical ( $\text{ROO}^\bullet$ ), carbonate ( $\text{CO}_3^{\bullet-}$ ) radicals, hypochlorous acid ( $\text{HClO}$ ), hypobromous acid ( $\text{HBrO}$ ) and hydroxyl radicals ( $^\bullet\text{OH}$ ). Amongst them,  $\text{O}_2^{\bullet-}$  is one of the initial reactive oxygen species produced in cells, which is mainly produced by the reaction of electrons provided by nicotinamide adenine dinucleotide phosphate (NADPH) oxidase and oxygen during respiration (Scheme 1).<sup>10</sup> At the same time,  $\text{O}_2^{\bullet-}$  can generate  $\text{O}_2$  and  $\text{H}_2\text{O}_2$  through the disproportionation reaction in the presence of superoxide dismutase (SOD) and water (Scheme 1).  $\text{H}_2\text{O}_2$  is an important signaling molecule and oxidant in the organism. However, abnormally high levels of  $\text{H}_2\text{O}_2$  in the presence of redox active metal ions like  $\text{Fe(II)}$  or  $\text{Cu(I)}$  can generate  $^\bullet\text{OH}$  through the Fenton and Haber–Weiss reaction, which can cause damage to biomolecules (Scheme 1).<sup>11,12</sup> In addition, due to the presence of chloride, bromide, and myeloperoxidase (MPO) in neutrophils,  $\text{H}_2\text{O}_2$  can be converted into hypochlorous acid or hypobromous acid, which are extremely



Jiaying Zhou

Jiaying Zhou obtained her BS Degree from the School of Chemistry and Chemical Engineering, University of Jinan (2016–2020). She is pursuing an MS degree in Chemistry under the supervision of Prof. Zhuo Wang in Beijing University of Chemical Technology. Her research interests are focused on probes for sensing Reactive Oxygen species (ROS) and Reactive Nitrogen species (RNS).



Mingguang Zhu

Mingguang Zhu obtained his BS degree in 2021 from the Beijing University of Chemical Technology. He is currently a postgraduate student under the guidance of Professor Wang Zhuo in Beijing University of Chemical Technology. His research focuses on the design and synthesis of new fluorescent probes.



Jiang Liu

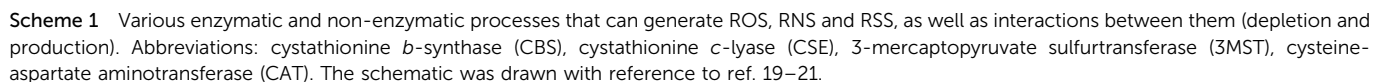
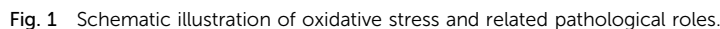
Jiang Liu received her MS degree in Chemistry from Beijing University of Chemical Technology (China) in 2022. She is pursuing a PhD degree in Beijing University of Chemical Technology. Her research focuses on the exploration of new nanomaterials for reactive oxygen species scavenging.



Tony D. James

Tony D. James is Professor at the University of Bath and Fellow of the Royal Society of Chemistry. He was a Royal Society University Research Fellow (1995–2000), Wolfson Research Merit Award holder (2017–2022) and was awarded the Daiwa-Adrian Prize (2013), the CASE Prize (2015), the MSMLG Czarnik Award (2018) and Frontiers in Chemistry Diversity Award. (2020). His research interests include many aspects of supramolecular chemistry, including probes for redox imbalance and theranostic systems. His h-index is 82 (Google Scholar) and he was listed by Clarivate as a Highly Cited Researcher in 2022.







strong and destructive ROS (Scheme 1).<sup>13</sup> RNS include peroxynitrite (ONOO<sup>−</sup>), nitric oxide (NO or NO<sup>•</sup>), nitrogen dioxide radical (NO<sub>2</sub><sup>•</sup>), nitrite (NO<sub>2</sub><sup>−</sup>), *S*-nitrosothiol (RSNO) and nitroxide (HNO), *etc.* Amongst them, NO is an important signaling molecule,<sup>14</sup> and is irreplaceable in the collaborative work between cells in regulating human metabolism. ONOO<sup>−</sup> is produced by diffusion-controlled reaction of O<sub>2</sub><sup>•−</sup> and nitric oxide and has relatively strong oxidizing properties (Scheme 1).<sup>15</sup> Active sulfur RSS refers to a species that contains sulfur atoms and has redox activity in the organism, and mainly includes biological thiols, hydrogen sulfide (H<sub>2</sub>S), disulfide (RSSR), polysulfides (R<sub>2</sub>S<sub>*n*</sub>/H<sub>2</sub>S<sub>*n*</sub>, *n* > 2), sulfur dioxide/sulfurous acid salt/bisulfite (SO<sub>2</sub>/SO<sub>3</sub><sup>2−</sup>/HSO<sub>3</sub><sup>−</sup>), thienyl radical (RS<sup>•</sup>) and sulfenic acid.<sup>16</sup> Biological thiols (RSH) mainly includes glutathione (GSH), cysteine (Cys), and homocysteine (Hcy). RSH is an important reducing agent for the organism, and plays an important role in maintaining the redox balance. H<sub>2</sub>S is considered to be the third endogenous gaseous transmitter after NO and CO.<sup>17</sup> Polysulfides are a class of sulfur-containing compounds that are widely found in prokaryotic and eukaryotic cells, and they are oxidation products of H<sub>2</sub>S (Scheme 1).<sup>18</sup>

Meanwhile, biological and clinical methods have been used to prove that oxidative stress is closely related to the pathological process of a variety of diseases, such as inflammation, neurodegenerative diseases and cancer.<sup>22–25</sup> Due to the short life time, high reactivity, and transient characteristics of RONSS (ROS, RNS, and RSS) in organisms, a deeper understanding and direct evidence of the link between RONSS and disease pathophysiology is not available. At present, the clinical judgment of oxidative stress in patients is mainly through the determination of the redox products produced by RONSS and the downstream functional markers of RONSS-induced damage. For example, a typical method is to determine the glutathione/GSSG and cysteine/cystine redox couple in the patient's plasma,<sup>26,27</sup> as well as to determine the level of oxidized nucleosides in the urine (Judging the oxidative damage of DNA/RNA in cells).<sup>28,29</sup> Unfortunately, these assays are susceptible to other pathological and physiological factors. At the same time, it is not possible to directly observe the dynamic process of oxidative stress in the patient's body in real time and determine which type of oxidant/reducing agent plays a decisive role in the pathophysiological process.<sup>30</sup> Therefore, these methods cannot meet the requirements of biologists for the study of pathological oxidative stress in cells/tissues and *in vivo*. Fluorescence based imaging technologies that combine confocal imaging, two-photon imaging and *in vivo* imaging can provide non-invasive, real-time, and high-resolution images of cells and animals, and as such have gradually become powerful support tools for basic biomedical research.<sup>31–36</sup>

We and other researchers have reviewed fluorescent probes for RONSS detection over the last few years.<sup>37–41</sup> These reviews focus mainly on probe design (selection of fluorophore and recognition groups), sensing mechanisms and performance evaluation, but provide little generalization or detail on biomedical applications. In 2019, Kim *et al.* discuss ROS and RNS fluorescence imaging in relation to pathophysiological processes, but ignore the

essential role of RSS in redox homeostasis.<sup>42</sup> In addition, RONSS fluorescent probes in the NIR II region and FL/PA dual-mode probes and dual-responsive probes are not included in the previous reviews. These three types of probes are receiving more and more attention due improved applicability. Notably, the field of fluorescent probes is facing a number of challenges. For example, the development of novel RONSS recognition groups is stalling, single-function fluorescent probes (non-NIR and unidirectional detection) are saturated, and many probes have similar biomedical applications (arthritis, peritonitis and liver injury). We believe that some guidance is urgently needed in this area to avoid stagnation in the development of improved probes.

As a commonly occurring pathological state, oxidative stress is closely related to human physiological and pathological activity, lifespan and many diseases. Fluorescent probes, a useful tool for biomedical research, can provide imaging information for the study of pathological oxidative stress. In this review we summarize representative RONSS fluorescent probes used for biomedical research published over the past six years. Based on the different pathological models, these probes are divided into three categories: (i) dual-response fluorescent probes for the monitoring of RONSS and flux of related active species in cells; (ii) fluorescent probes for RONSS imaging in pathological processes, including visualization of inflammation and organ damage, and evaluation of drug toxicity and safety of surgical procedures; (iii) fluorescent probes for RONSS imaging in oxidative stress-related disease models, involved in pathology studies, drug screening and evaluation of treatment efficacy. The links between oxidative stress and inflammation, organ damage, Alzheimer's disease, Parkinson's disease, epilepsy, depression, diabetes, and cancer are also introduced. At the same time, the design concepts, basic operational conditions for the probes and future development directions are outlined. Such research is a vital resource to provide the theoretical basis and intuitive evidence for the prevention of related diseases, drug design and postoperative diagnosis. Therefore, we anticipate that this review will provide appropriate guidance for chemical, biological, and medical researchers as well as drug discovery scientists.

## 2. Design of fluorescent probes for RONSS imaging

Fluorescent probes can detect target compounds using weak molecular interaction or chemical reactions.<sup>43</sup> Molecular fluorescent probes are typically composed of three parts: a fluorophore, a linker and a recognition group. As far as the recognition mechanism is concerned, traditional design strategies provide optical recognition for detection through the interaction (including coordination and inclusion) of fluorescent probes with analytes (Fig. 2(a)).<sup>44</sup> However, the design of lock-and-key molecular recognition and binding in the recognition of proteins is not suitable for most RONSS fluorescent probes.<sup>44,45</sup> Most ROS and RNS molecules are similar in physical size, and most of them have the characteristics of short lifespan, low concentration, and high reactivity in biological systems. As such chemical





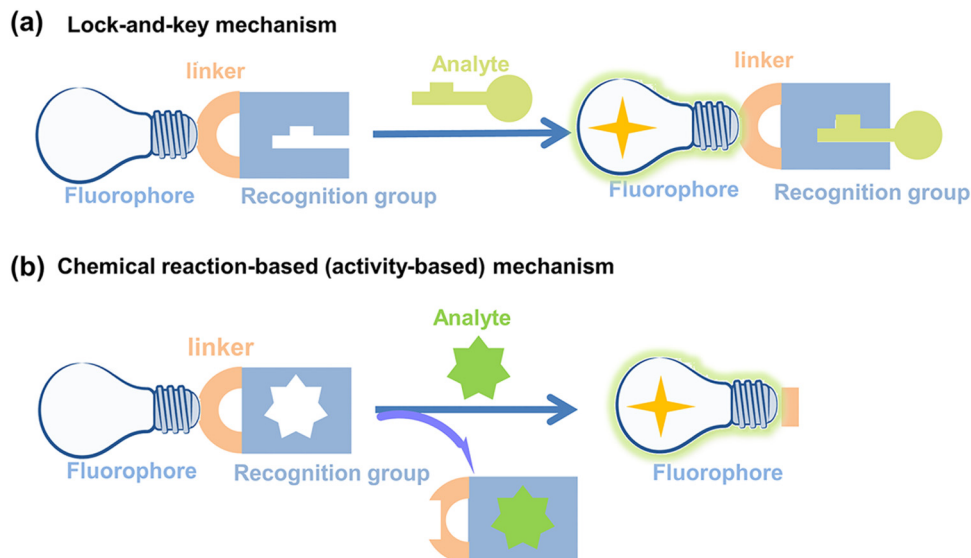


Fig. 2 Schematic illustration of (a) lock-and-key mechanism and (b) chemical reaction-based (activity-based) mechanism for fluorescent probes.

reaction-based (activity-based) fluorescent probes are ideal tools for real-time imaging of RONSS (Fig. 2(b)).<sup>46</sup> The sensing mechanisms used mainly include photoinduced electron transfer (PeT), intramolecular charge transfer (ICT), fluorescence resonance energy transfer (FRET), excited-state intramolecular proton transfer (ESIPT), and aggregation-induced emission (AIE). In this section, we will briefly introduce research progress for fluorophores, linkers and recognition groups related to RONSS.

## 2.1 Fluorophores

Hundreds of fluorescent probes have now been used to detect RONSS, almost all of which derive their primary fluorescent moieties from a number of classical fluorescent backbones and derivatives. They are chemically and photostable, while providing a wealth of modifiable structural sites. We selected six fluorophores that are widely used in the field of pathological RONSS imaging as examples.

**2.1.1 Rhodamine.** Rhodamine dyes are one of the classic fluorescent labeling reagents and exhibit many excellent photo-physical properties, including high fluorescence quantum yield and photostability.<sup>47</sup> The typical chemical structure of rhodamine contains three benzene rings (labeled B1/2/3 in Fig. 3(a)), and the heteroatom X is an oxygen atom. The dynamic equilibrium of the spironolactone and ring-opened forms determines the conjugated structure and spectral properties. In polar solvents, the opening of the spironolactone significantly improves the molar absorption coefficient and fluorescence quantum yield of rhodamine. In non-polar solvents, the formation of spironolactone interrupts the  $\pi$ -conjugated structure and results in low fluorescence quantum yield (Fig. 3(a)).<sup>48</sup> Based on this property, the controlled opening of spirolactams and thiolactones has been widely applied for the design RONSS-responsive fluorescent chemosensors.<sup>49</sup>

**2.1.2 Cyanine and hemicyanine.** Cyanine, as a class of widely used fluorescent dyes, have high molar absorptivity, high fluorescence quantum yield and significantly separated

absorption and emission wavelengths.<sup>50</sup> Classic cyanine dyes contain two nitrogen-containing heterocycles, one of which is positively charged (Fig. 3(b)). The two nitrogen-containing heterocycles are linked by a conjugated polymethine chain containing an odd number of carbons.<sup>51</sup> Since both excitation and emission wavelengths ( $\lambda_{\text{ex}}/\lambda_{\text{em}} = 750 \text{ nm}/780 \text{ nm}$ ) are in NIR-I, the indole heptamethine cyanine has attracted significant attention (Fig. 3(b)). Cyanine-based fluorescent dyes can be designed by introducing different recognition group to replace the structural core (R) and the different *N*-substituted side chains ( $R_1$  and  $R_2$ ) (Fig. 3(b)). A series of NIR fluorescent dyes for monitoring the dynamic levels of RONSS in cells and *in vivo* based on the heptamethine cyanine fluorophore have been developed.<sup>52</sup>

As an exceptional fluorophore over the past decade, hemicyanines are widely used to study the dynamic changes of RONSS levels in complex biological systems due to their easy structural modification and excellent biocompatibility.<sup>53,54</sup> Generally, the hemicyanine structure consists of three parts: (i) a nitrogen-containing heterocycle with a positive charge as an electron acceptor; (ii) electron donor (*e.g.*, hydroxyl, methoxy, amino or amine group); (iii) conjugated structure connecting the two parts.<sup>51</sup> Hemicyanine dyes are donor- $\pi$ -acceptor (D- $\pi$ -A) systems. Significantly, many research groups have developed novel functionalized hemicyanine frameworks. In 2012, Lin *et al.* reported a new class of hemicyanine fluorescent dyes (O-HD) with NIR excitation and emission wavelengths and a modifiable terminal hydroxyl group (Fig. 3(c)).<sup>55</sup>

**2.1.3 Boron-dipyrromethene (BODIPY).** The first BODIPY compound was reported in 1968, this class of dyes has significant molar extinction coefficient, excellent fluorescence quantum yield, and good photostability. BODIPY has been used for imaging the biomarkers of oxidative stress.<sup>56</sup> Traditional BODIPY dyes contain two symmetrical pyrrole rings with a six-membered boron nitrogen heterocycle (Fig. 3(d)), and BODIPY exists as a stable conjugated planar structure. The spectral properties can be



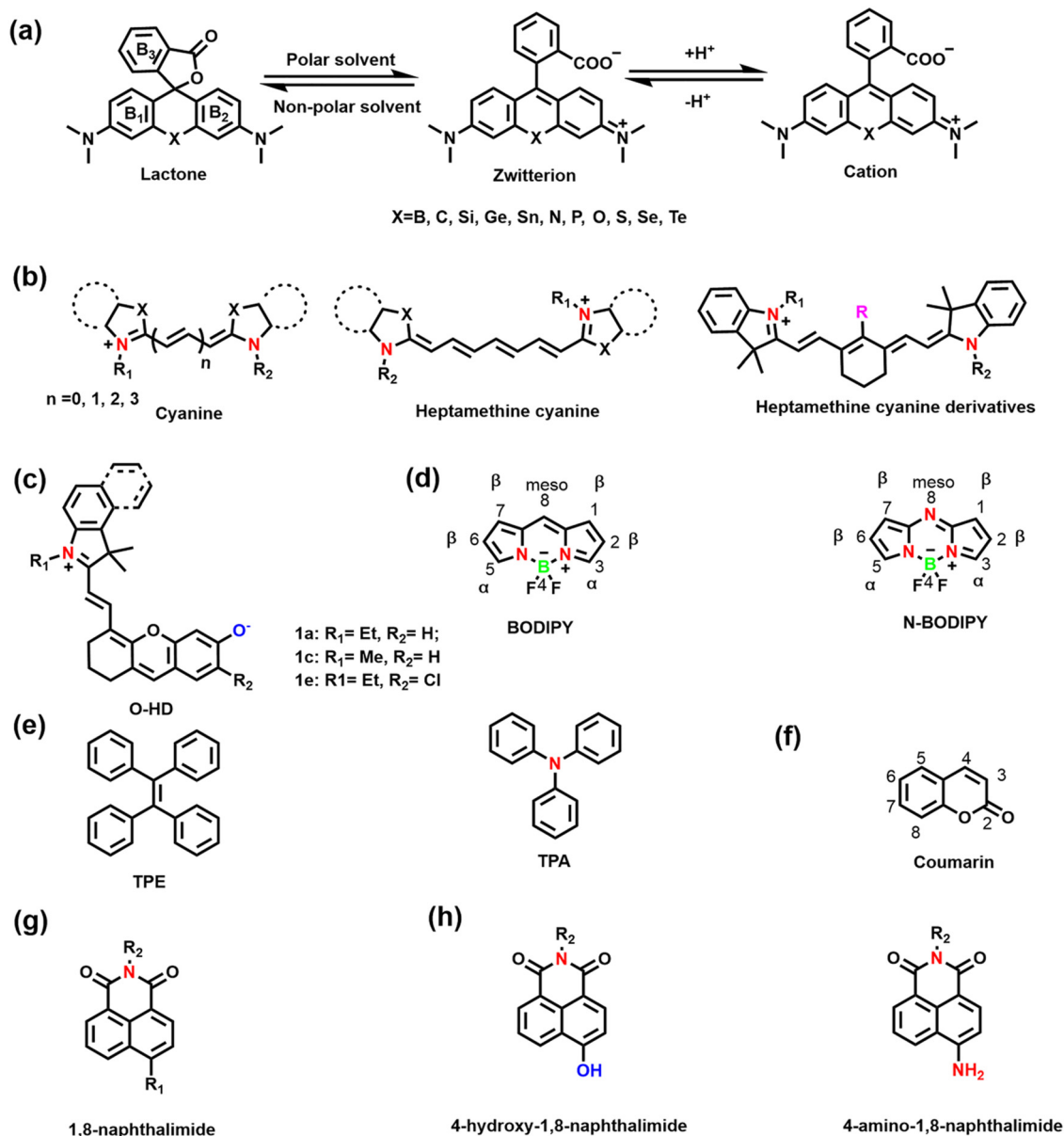


Fig. 3 (a) Schematic illustration of Rhodamine structure and equilibrium of Rhodamine between spirolactone and ring-opening form. (b) Schematic illustration of cyanine structures and heptamethine cyanine dyes. (c) The structure of hemicyanine fluorescent dyes (1a–1e). (d) Schematic illustration of BODIPY frameworks and N-BODIPY. (e) Schematic illustration of TPE and TPA frameworks. (f) Schematic illustration of coumarin framework. (g) Schematic illustration of 1,8-naphthalimide framework. (h) Molecular structure of 4-hydroxy-1,8-naphthalimide and 4-amino-1,8-naphthalimide.

fine-tuned by adjusting the substituents at  $\alpha$  and  $\beta$  positions on the BODIPY framework. Through the replacement of carbon atoms at the meso sites with N atoms, the Stokes shift can be significantly improved while retaining the excellent properties of BODIPY.<sup>57</sup>

**2.1.4 Aggregation-induced emission fluorogens.** Traditional fluorescent molecules emit light in dilute solution, but as their concentration increases, fluorescence quenching occurs due to intermolecular  $\pi$ – $\pi$  interactions.<sup>58</sup> This phenomenon is termed aggregation-caused quenching (ACQ). The ACQ effect limits the concentration of traditional fluorescent dyes that can be used for *in vitro* and *in vivo* imaging.<sup>59</sup> The emergence of

aggregation-induced emission fluorogens (AIEgens) solves the problem of reduced luminescence when fluorescent dyes exist as aggregates/clusters.<sup>60</sup> The mechanism of AIE has been explained as restricted intramolecular rotation (RIR) caused by various intermolecular interactions.<sup>61</sup> Tetraphenylene and triphenylamine have the characteristics of easy structural modification, simple synthesis, and easy regulation of spectral properties (Fig. 3(e)) and have been widely used in cancer diagnosis/therapy, bacterial/cellular imaging and the detection of oxidative stress biomarkers.<sup>62–65</sup>

**2.1.5 Coumarin dyes.** Coumarins, with the structure of 2H-chromen-2-one motif exhibit good biocompatibility, excellent photophysical properties, easy structural modification and



regulation of optical properties (Fig. 3(f)).<sup>66</sup> Since coumarin exhibits short-wavelength excitation and emission wavelengths, the introduction of electron-donating groups (such as hydroxyl, amino and diethylamine groups, *etc.*) at the 6-position/7-position or the introduction of an electron-accepting group at the 3-position/4-position can significantly increase the push-pull electron effect in the molecule, which results in red-shifted fluorescence.<sup>67</sup> In addition, FRET-based fluorescent probes can be co-constructed using coumarin with other fluorophores and have been widely used for the imaging of biomarkers associated with oxidative stress in cells.<sup>68–70</sup>

**2.1.6 1,8-Naphthalimide.** The 1,8-naphthalimide dye exhibits good chemical stability, high resistance to photobleaching and large Stokes shift.<sup>71</sup> 1,8-Naphthalimide is an electron-deficient system, in which the naphthalene ring acts as a  $\pi$  bridge and the imide part acts as an electron acceptor. Generally,  $R_1$  is an electron donor, and  $R_2$  is an organelle targeting group or an analyte-responsive group (Fig. 3(g)).<sup>72,73</sup> Based on the strong electron-donating ability and easy modification of the hydroxyl and amino groups, 4-amino-1,8-naphthalimide and 4-hydroxy-1,8-naphthalimide have garnered significant interest in the field of RONSS sensors (Fig. 3(h)).<sup>74,75</sup>

## 2.2 Linker

The linker is the bridge between the fluorophore and the recognition group, which is crucial for the optical properties of small molecule based fluorescent sensors. The linker used for fluorescent probes suitable for RONSS detection can be divided into four categories: (i) C–C/N/S single bonds or  $\pi$  bridges; (ii) ether bonds (such as O, S, Se, Te, *etc.*); (iii) ester bonds and amide bonds; (iv) pyridinium/quinolinium. In the presence of analytes, changes of the conjugated structure and the formation of residual groups, including hydroxyl, carboxyl, amino/amine, or pyridine/quinoline, *etc.*, directly influences the spectral properties of the sensor.

## 2.3 Recognition groups

### 2.3.1 Recognition groups for ROS and RNS detection.

Among various ROS, the instability of the O–O bond enables  $H_2O_2$  to act as a two-electron electrophilic oxidant, while the  $\alpha$ -effect of adjacent nonbonding orbitals on the oxygen atoms enables  $H_2O_2$  to act as a nucleophile.<sup>76</sup> Some specific  $H_2O_2$ -recognition groups based on the amphiphilic reactivity of  $H_2O_2$  have been explored. The boronic ester/boronic acid and its benzyl derivatives can react with  $H_2O_2$  to form the corresponding phenol/amine group/amino group and has become the most widely utilized  $H_2O_2$  recognition group.<sup>44,77</sup> Nitrophenyldicarbonyl can be used for the recognition of  $H_2O_2$  by Baeyer–Villiger oxidation rearrangement reactions, and pentafluorobenzenesulfonyl can sense  $H_2O_2$  by an arylsulfonyl ester cleavage mechanism.<sup>78,79</sup>  $O_2^{\bullet-}$  is the one-electron reduction product of  $O_2$ , which can be used as the precursor of many reactive oxygen species.<sup>80</sup> Some specific recognition groups based on the oxidative and nucleophilic properties of  $O_2^{\bullet-}$  have been investigated. Recognition groups designed based on redox mechanisms include benzothiazole, indoline and catechol.<sup>81–83</sup> Recognition groups designed based

on nucleophilicity include 2,4-dinitrobenzenesulfonyl, trifluoromethanesulfonate and diphenylphosphinate.<sup>84–86</sup> While  $O_3$  can undergo a specific cycloaddition reaction with the terminal olefin of the 3-butenyl moiety to enable detection.

Hydroxyl radicals have the strongest oxidative properties, short lifespans and low physiological concentrations of all the ROS.<sup>87</sup> Compared with other ROS sensors,  $\bullet OH$  still lacks a universal and specific recognition group.<sup>88</sup> Several basic strategies can be used to design molecular fluorescence sensors for  $\bullet OH$ , including aromatic hydroxylation strategies; oxidative dehydrogenation strategies; and oxidation strategies of sulfur atoms.<sup>89–91</sup>  $HClO/Clo^-$  is an endogenous ROS with strong oxidizing properties. Based on the reaction mechanism (such as oxidation of chalcogenides or oxidative cleavage reaction), common recognition groups can be roughly divided into three categories: (i) lactam/lactone, such as hydrazide,  $N,N$ -dimethylcarbamoyl; (ii) various double bonds, such as oxime, malononitrile and hemicyanine; (iii) sulfur/selenium-containing groups, such as thioethers, thioacetals, thioesters and selenolactones.<sup>92,93</sup>

Nitric oxide is a reactive free radical with oxidizing and reducing properties. *o*-diamino aromatics are the most commonly used recognition groups, which can form triazole derivatives with NO under aerobic conditions.<sup>94</sup> In addition, *N*-nitrosation of aromatic amines is another common strategy.<sup>95</sup> Peroxynitrite is a short-lived, low-concentration and highly reactive endogenous RNS.<sup>96</sup> The common recognition groups for  $ONOO^-$  can be divided into four categories: (i) the boronic ester/boronic acid and its benzyl derivatives (the reaction speed of boronic acids or boronates with  $ONOO^-$  is much higher than for  $H_2O_2$ ); (ii) hydrazide; (iii) carbon–carbon double bonds; (iv) aromatic phenols (these electron-rich phenol groups need to be bound to *N*-aryl-containing fluorophores).<sup>96,97</sup>

Furthermore, off-target activities of different probes should be treated carefully, as this is often a significant and yet commonly omitted aspect of the reliability of the RONSS detection by fluorescent probes. RONS can be divided into highly reactive h-RONS (*e.g.*  $\bullet OH$ ,  $ONOO^-$ , and  $Clo^-$ ) and normally reactive n-RONS (*e.g.*  $H_2O_2$ ,  $O_2^{\bullet-}$ ,  $O_3$ , NO). The difference in oxidation between the RONS is an important basis for the selection of the recognition group. In general, there is little mutual interference between n-RONS. At the same concentration and time scales, n-RONS hardly interfere with the recognition of h-RONS. However, as h-RONS are highly oxidative and nucleophilic, they not only increase the likelihood of off-target recognition of n-RONS (*e.g.* boronic esters and derivatives are more reactive with  $ONOO^-$  than  $H_2O_2$ ), but also interfere with each other. For example, the oxidation properties of  $ONOO^-$  and  $HOCl$  are highly similar, but  $ONOO^-$  is more oxidizing.<sup>98</sup> Two recognition strategies are currently widely used in the field of fluorescence imaging of  $ONOO^-$ ,  $\bullet OH$  and  $HOCl$ , which includes cleavage of C=C double bonds and oxidation of chalcogenides. Therefore, the off-target activities of probes to identify h-ROS should be considered carefully in complex pathological environments.

**2.3.2 Recognition groups for RSS detection.** Compounds containing sulfhydryl groups are referred to as thiols.<sup>99</sup> Biothiols include cysteine (Cys), homocysteine (Hcy) and glutathione (GSH). Due to the strong nucleophilicity of the sulfhydryl groups,





Michael addition reactions and cleavage reactions of sulfonate esters are often used to distinguish thiols. The typical recognition groups are maleimide and 2,4-dinitrobenzenesulfonyl.<sup>100,101</sup> The distinction between thiols mainly depends on the difference in the activity of the thiols and the different steric demands. Native chemical ligation (NCL), Michael addition reaction and addition-cyclization reactions are often used to distinguish Cys/Hcy from GSH. Commonly used recognition groups include thioesters, acrylates,  $\alpha,\beta$ -unsaturated ketones and aldehyde groups.<sup>102–105</sup> The structures of Cys and Hcy are very similar (they differ by one methylene group), as such probes for their successful discrimination are rare. In 2013, Guo *et al.* reported a chlorinated coumarin–hemicyanine dye with three potential reactive sites and achieved selective detection of Cys, Hcy and GSH in cells.<sup>106</sup> Recently, Song *et al.* reported a coumarin dye with a phenylethynyl group, and the presence of Cys or Hcy could induce different ratiometric fluorescence changes.<sup>107</sup>

H<sub>2</sub>S is the simplest biological thiol in living systems and has strong nucleophilic and reducing properties.<sup>108</sup> H<sub>2</sub>S can attack the electrophilic center of a conjugated structure through nucleophilic addition, so the positively charged indole salt of hemicyanine has been used as a recognition group.<sup>109,110</sup> In addition reduction-based azide, nitro and thiolysis-based nitrobenzoxadiazole (NBD) ether, and 2,4-dinitrophenyl ether have been used as H<sub>2</sub>S-recognition groups.<sup>111–114</sup> Hydrogen polysulfides (H<sub>2</sub>S<sub>*n*</sub>, *n* > 1) are the oxidized form of H<sub>2</sub>S, which are more nucleophilic and reducing.<sup>115</sup> The most commonly used recognition groups are divided into two categories according to the reaction mechanism. One is based on the aromatic nucleophilic substitution reaction, and the recognition groups are 2-fluoro-5-nitrobenzoic ester and phenyl 2-(benzoylthio) benzoate. The other one is based on the reduction reaction, and the recognition group has an aromatic nitro group.<sup>116–118</sup> Sulfur dioxide (SO<sub>2</sub>) exists in aqueous solution as sulfite (SO<sub>3</sub><sup>2−</sup>) and hydrogen sulfite (HSO<sub>3</sub><sup>−</sup>).<sup>119</sup> Recognition groups designed for the strong nucleophilicity of SO<sub>2</sub> can be divided into four categories: (i) levulinate; (ii)  $\alpha,\beta$ -unsaturated ketones; (iii) aldehyde groups; (iv) carbon–carbon double bonds (nucleophilic addition to C=C bonds is a common strategy).<sup>120–123</sup>

The RSS assay also requires vigilance for off-target activity of the probes. The nucleophilicity, reducibility and molecular structure of the different RSS are the basis for the selection of

the recognition groups. Some biological thiols are generally less reactive than H<sub>2</sub>S/H<sub>2</sub>S<sub>*n*</sub>, but they are very abundant in cells (*e.g.* 1–10 mM for GSH and 30–200  $\mu$ M for Cys). Therefore, when assessing the off-target activity of RSS probes, physiological concentration levels of interferents need to be considered (Table 1).

### 3. Fluorescent probes for oxidative stress imaging in cells

RONSS are ubiquitous in cells, and involved in numerous biological mechanisms including cell protection, apoptosis, signal transduction, inflammation and cancer.<sup>124</sup> Physiological levels of RONSS are essential for the correct performance of cell functions, but long-term exposure to high levels of RONSS can damage organelles and ultimately induce cell apoptosis and various diseases. Importantly, these diseases are not caused by a single factor, and involve changes in the levels of multiple RONSS and related species. Therefore, the detection of multiple RONSS in cells is of significant interest for understanding the pathology of the disease. Over the past few decades, enzyme-linked immunosorbent assays (ELISA), electrochemical analysis, mass spectrometry (MS) and high-performance liquid chromatography (HPLC) methods have been used to detect intracellular RONSS.<sup>125–130</sup> However, these methods have several disadvantages such as difficulty in sample preparation, require expensive instrumentation and are unsuitable for real-time analysis. In particular, the extraction of oxidative markers (such as deoxyribose, nucleic acids, proteins, lipids, *etc.*) often destroys the structure of cells and tissues making real-time analysis *in vivo* impossible. Compared with these detection technologies, fluorescent probes combined with a variety of imaging technologies can monitor the physiological and pathological conditions of cells in a non-invasive, real-time, highly-sensitivity and high-resolution manner.

Many diseases are not typically caused by a single factor, and the combined use of multiple sensors can cause numerous problems such as spectral overlap, analyte crosstalk, increased biotoxicity, photobleaching and localization since two species are involved. A promising solution is to use a single probe that

Table 1 Summary of recognition groups or strategies for ROS/RNS/RSS covered in this paper

ROS/RNS/RSS	Recognition groups or strategies
H <sub>2</sub> O <sub>2</sub>	• Boronic ester/boronic acid, nitrophenyldicarbonyl, pentafluorobenzenesulfonyl
O <sub>2</sub> <sup>•−</sup>	• Benzothiazole, indoline, catecho, 2,4-dinitrobenzenesulfonyl, trifluoromethanesulfonate, diphenylphosphinate
O <sub>3</sub>	• 3-Methylpyrazolone
•OH	• Aromatic hydroxylation strategies, oxidative dehydrogenation strategies, oxidation strategies of sulfur atoms
HClO/CLO <sup>−</sup>	• Lactam/lactone, such as hydrazide, <i>N,N</i> -dimethylcarbamoyl; various double bonds, such as oxime, malononitrile and hemicyanine; sulfur/selenium-containing groups, such as thioethers, thioacetals, thioesters and selenolactones
NO	• <i>o</i> -diamino aromatics, <i>N</i> -nitrosation of aromatic amines
ONOO <sup>−</sup>	• Boronic ester/boronic acid; hydrazide; carbon–carbon double bonds; aromatic phenols
Thiols	• Maleimide, 2,4-dinitrobenzenesulfonyl
Cys/Hcy	• Thioesters, acrylates, $\alpha,\beta$ -unsaturated ketones and aldehyde groups
H <sub>2</sub> S	• Indole salt, azide, nitrobenzoxadiazole (NBD) ether, 2,4-dinitrophenyl ether
H <sub>2</sub> S <sub><i>n</i></sub> , <i>n</i> > 1	• 2-Fluoro-5-nitrobenzoic ester, phenyl 2-(benzoylthio) benzoate
SO <sub>2</sub>	• Levulinate, $\alpha,\beta$ -unsaturated ketones, aldehyde groups, carbon–carbon double bonds



reacts with two analytes, called dual-responsive fluorescent probes.<sup>131</sup> Based on the recognition logic, dual-responsive probes for RONSS detection are currently classified into the following types: (i) reversible probes, which mean two analytes interact with the probes in a reversible manner; in general, the two analytes are RONS and RSS which can proceed *via* a reversible redox reaction; (ii) sequence-specific reaction probes can react with different analytes through sequenced chemical reactions; (iii) competitive probes, which rely on competitive reactions between the two analytes and the probe, with varying optical properties of the reaction products; (iv) composite probes, which have two fluorophores and recognition groups, but no spectral overlap between the excitation and emission wavelengths. In this section, we have selected some recent examples describing multi-species imaging (RONSS and related species).

### 3.1 ROS + RSS

$\text{H}_2\text{O}_2$  and  $\text{H}_2\text{S}$  are important redox signal molecules, and they jointly participate in many redox physiological and pathological processes.<sup>132</sup> In order to further explore the relationship

between the two signal molecules, Wang *et al.* developed a fluorescent probe (TCAB) that could detect  $\text{H}_2\text{S}$  and  $\text{H}_2\text{O}_2$  independently (Fig. 4(a)).<sup>133</sup> The short-wavelength emitting coumarin HCB and the long-wavelength emitting fluorophore TQC together served as the fluorophore, while the benzyl boronic ester and azide group served as the respective sensing units of  $\text{H}_2\text{O}_2$  and  $\text{H}_2\text{S}$ , respectively. In the presence of  $\text{H}_2\text{O}_2$ , the benzyl boronic ester is removed to generate the cyan, fluorescent dye TCA. In the presence of  $\text{H}_2\text{S}$ , the azido moiety was reduced to an amino derivative and undergoes 1,6-elimination,  $\text{C}=\text{C}$  double isomerization and subsequent spontaneous intramolecular cyclization to release two fluorophores simultaneously (HCB in the blue channel and TQC in the red channel). In addition, the probe was able to detect  $\text{H}_2\text{O}_2/\text{H}_2\text{S}$  reversibly. The sequence of  $\text{H}_2\text{O}_2\text{--H}_2\text{S}$  produced cyan and then red signals, while the reverse reaction sequence produced red and then cyan signals. This study facilitated the imaging of endogenous  $\text{H}_2\text{S}$  and  $\text{H}_2\text{O}_2$  in cells (Fig. 4(b)), which allowed the monitoring of  $\text{H}_2\text{O}_2$  and  $\text{H}_2\text{S}$  redox processes in living cells and organisms.

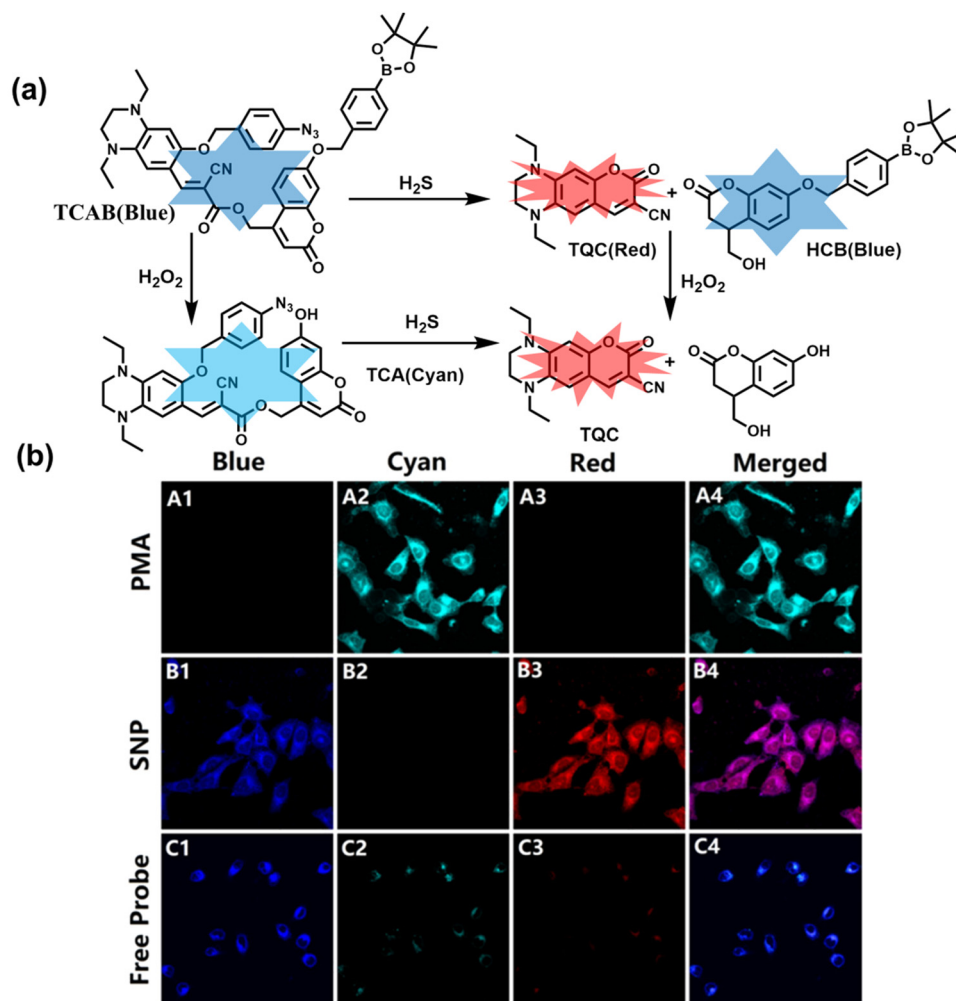


Fig. 4 (a) Structure and sensing mechanism of TCAB for the discrimination of  $\text{H}_2\text{O}_2$  and  $\text{H}_2\text{S}$ . (b) Confocal fluorescence images of endogenous  $\text{H}_2\text{O}_2/\text{H}_2\text{S}$  in living HeLa cells. SNP (sodium nitroprusside), Phorbol 12-myristate 13-acetate (PMA). Reproduced with permission from ref. 133. Copyright (2020) American Chemical Society.



As a member of RSS,  $\text{H}_2\text{S}_n$  is an important antioxidant in cells.<sup>134</sup> The interdependence and mutual restriction between  $\text{H}_2\text{S}_n$  and ROS promote redox homeostasis in cells. To better monitor the dynamic changes of redox in cells, Chen *et al.* developed a fluorescent probe (HCy-Mito) that could monitor the changes of  $\text{H}_2\text{S}_n$  and  $\text{O}_2^{\bullet-}$  in cells (Fig. 5(a)).<sup>135</sup> A heptamethine cyanine dye was chosen as the fluorophore. The oxidation of the N site in the cyanine platform was used to detect  $\text{O}_2^{\bullet-}$ , and *meta*-nitrophenol was used as a specific reaction site for  $\text{H}_2\text{S}_n$ . After HCy-Mito reacts with  $\text{O}_2^{\bullet-}$ , the fluorescence intensity was partially restored and a positively charged intermediate was generated. This intermediate could further react with  $\text{H}_2\text{S}_n$  in mitochondria to achieve complete recovery of the fluorescence intensity.

In addition, since HCy-Mito exhibited a degree of spectral overlap during imaging, Chen *et al.* developed an improved fluorescent probe (HCy-ONO) (Fig. 5(b)) and used it to explore the influence of intracellular  $\text{H}_2\text{S}_n$  and  $\text{O}_2^{\bullet-}$  on redox homeostasis under hypoxic conditions.<sup>136</sup> Cyanine was selected as the fluorophore and the recognition group for  $\text{O}_2^{\bullet-}$ , 1-(3-nitrophenyl) ethanol replaced the previously used *meta*-nitrophenol as the recognition group for  $\text{H}_2\text{S}_n$ . In the presence of  $\text{O}_2^{\bullet-}$ , HCy-ONO formed Cy-ONO with low fluorescence quantum yield. This intermediate could further react with  $\text{H}_2\text{S}_n$  to release a cyanine fluorophore with an enhanced Stokes shift. Cell imaging experiments indicated that cells with intermittent hypoxia exhibited a higher fluorescence signal in channel 1 (750 to 850 nm), but the fluorescence signal in channel 2 (600 to 700 nm) was significantly lower than that for continuous hypoxic cells. In addition, the apoptotic rate of intermittent hypoxic cells was higher than that

of persistent hypoxic cells. These results indicated that reoxygenation during intermittent hypoxia could induce  $\text{O}_2^{\bullet-}$  bursts and consume high levels of over-expressed  $\text{H}_2\text{S}_n$ , which is the main contributor for oxidative damage of cells.

As an important antioxidant in organisms,  $\text{SO}_2$  plays an important role in regulating the redox balance.  $\text{SO}_2$  is produced by the oxidative decomposition of  $\text{H}_2\text{O}_2$  and sulfur-containing amino acids in cells and exists as  $\text{HSO}_3^-$ .<sup>137</sup> In order to clarify the complex role of  $\text{H}_2\text{O}_2/\text{SO}_2$  in regulating oxidative stress, Wang *et al.* designed a benzothiazole-based cyanine fluorescent probe HBT-Cy (Fig. 5(c)).<sup>138</sup> The phenylthiophene and cyanine moieties resulted in the probe exhibiting dual emission bands at 450 nm and 590 nm under a single excitation of 390 nm. Interestingly, the fluorescence signal at 590 nm gradually disappears through the nucleophilic addition reaction between HBT-Cy and  $\text{HSO}_3^-$ , and the fluorescence signal was restored in the presence of  $\text{H}_2\text{O}_2$ . When HBT-Cy was co-cultured with human breast cancer cells, the cells exhibited bright red fluorescence and weak blue fluorescence. While the addition of an exogenous  $\text{SO}_2$  donor could increase the blue fluorescence and weaken the red fluorescence. This process was reversible with the changes of the dynamic levels of  $\text{SO}_2$  and  $\text{H}_2\text{O}_2$  in the cells.

In addition to being an endogenous reducing agent,  $\text{SO}_2$  also has a certain oxidizing ability.<sup>139</sup> In order to further understand the dual role of  $\text{SO}_2$  in oxidative stress, You *et al.* designed a dual response probe (MPIBA) for  $\text{SO}_2/\text{ClO}^-$  (Fig. 6(a)).<sup>140</sup> MPIBA (red fluorescence,  $\lambda_{\text{em}} = 625 \text{ nm}$ ) was composed of a fluorophore modified with phenanthrimidazole and malononitrile, which could react with  $\text{SO}_2/\text{ClO}^-$  to produce compound

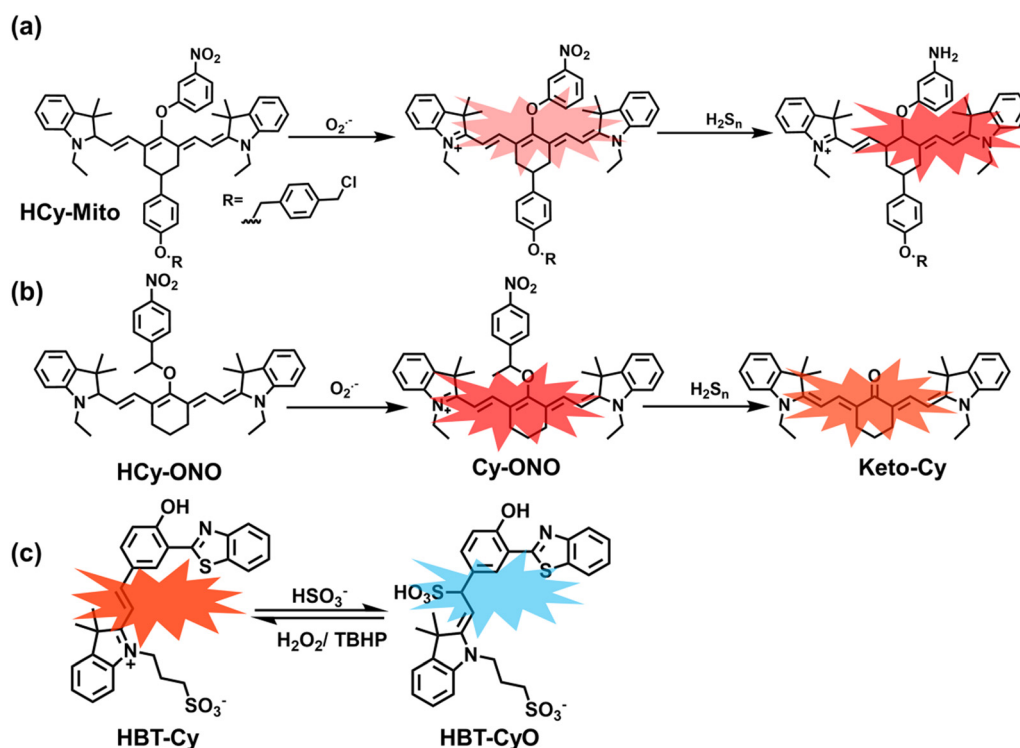


Fig. 5 (a) HCy-Mito based on heptamethine cyanine and its reactions with  $\text{H}_2\text{S}_n$  and  $\text{O}_2^{\bullet-}$ . (b) HCy-ONO based on heptamethine cyanine and its reactions with  $\text{H}_2\text{S}_n$  and  $\text{O}_2^{\bullet-}$ . (c) Benzothiazole-based cyanine fluorescent HBT-Cy and its reactions with  $\text{HSO}_3^-$  and  $\text{H}_2\text{O}_2$ .





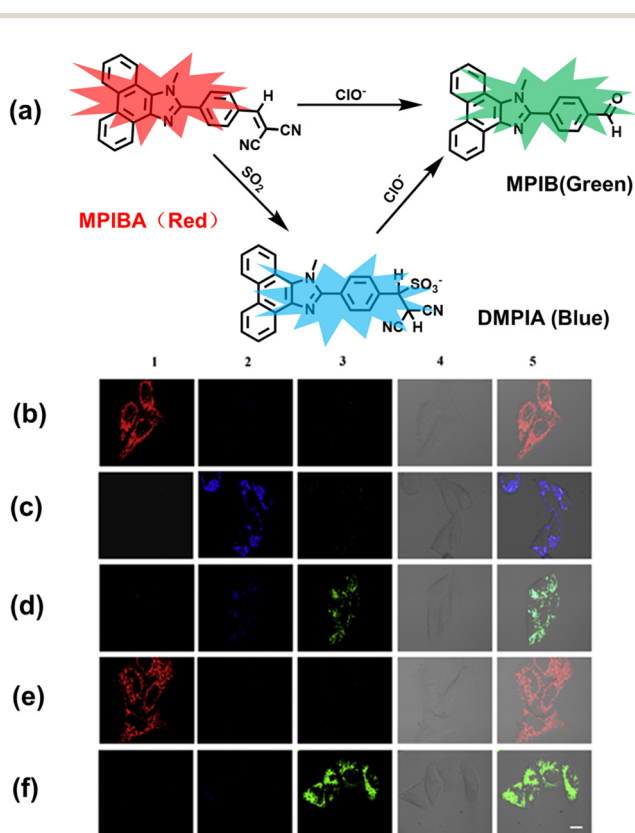
DMPIA (blue fluorescence,  $\lambda_{em} = 410$  nm) and MPIB (green fluorescence,  $\lambda_{em} = 500$  nm). Interestingly, DMPIA could still be oxidized by  $\text{HClO}$  to produce MPIB (Fig. 6(a)). In addition, MPIBA also had ultra-fast response speed ( $\text{SO}_2$ : < 60 s;  $\text{ClO}^-$ : within a few seconds) and high sensitivity (detection limit:  $\text{SO}_2$ : 3.5 nM;  $\text{ClO}^-$ : 12.5 nM). Finally, MPIBA was used to explore the dual role of  $\text{SO}_2$  in oxidative stress (Fig. 6(b–f)). Compared with the red fluorescence signal of the control group (Fig. 6(b) and (e)), bright blue fluorescence could be observed in HeLa cells treated with BTSA (an  $\text{SO}_2$  donor) (Fig. 6(c)). At the same time, an apoptosis rate of 6.5% indicated that excess  $\text{SO}_2$  results in cell oxidative damage. The cells treated with myeloperoxidase (MPO),  $\text{H}_2\text{O}_2$  and NaCl exhibited weak green fluorescence and weak blue fluorescence (Fig. 6(d)), indicating that  $\text{SO}_2$  could act as a reducing agent. Significantly, the cells treated with myeloperoxidase,  $\text{H}_2\text{O}_2$  and NaCl exhibited only bright green fluorescence (Fig. 6(f)), but the apoptotic rate exceeded 45.8%, suggesting that  $\text{ClO}^-$  could seriously damage the cells. These results confirmed the dual role of  $\text{SO}_2$  in cells under oxidative stress, where  $\text{SO}_2$  could exert both oxidative and anti-oxidative effects on cells.

### 3.2 RNS + RSS

As the most abundant thiol in organisms, glutathione (GSH) exists in millimolar concentrations in most cells.<sup>141</sup> While,  $\text{ONOO}^-$  is a RNS with strong oxidizing ability, and high levels of expression are detrimental to cell health. To monitor the close relationship between  $\text{ONOO}^-$  and GSH in cells, James *et al.* developed a fluorescent probe (GSH-PF<sub>3</sub>) using AND logic (Fig. 7(a)).<sup>142</sup> Fluorescein was selected as the fluorophore, and 2,4-dinitrobenzenesulfonyl and the boronic ester were used as the specific sensing units for GSH and  $\text{ONOO}^-$ , respectively. Since GSH-PF<sub>3</sub> exhibited AND logic, there was no significant change in fluorescence intensity when  $\text{ONOO}^-$  or GSH alone were present. However, when GSH-PF<sub>3</sub> was exposed to both analytes, the fluorescence intensity increased significantly (40 times). Importantly, by co-cultivating the probe with macrophages stimulated under different conditions, it was found that cells co-stimulated with lipopolysaccharide (LPS, which mediates cellular production of RONS) and an appropriate amount of caffeic acid (CA, a drug that elicits endogenous GSH) displayed bright fluorescence (Fig. 7(c)). However, the fluorescence intensity for single-stimulated cells was significantly lower.

Probes based on excited state intramolecular proton transfer (ESIPT) exhibit the advantages of large Stokes shift, ratiometric fluorescence and environmental sensitivity, James *et al.* subsequently developed an (ESIPT)-based “AND” logic system probe (GSH-ABAH) for imaging thiols and  $\text{ONOO}^-$  in cells (Fig. 7(b)).<sup>143</sup> The probe consisted of three parts: (i) ESIPT-based fluorophore 4-amino-2-(benzo[d]thiazol-2-yl) phenol (ABAH); (ii) benzyl boronic ester was the recognition unit for  $\text{ONOO}^-$  and blocked the ESIPT process; (iii) maleimide quenches the fluorescence by photoelectron transfer (PeT) and was selected as the GSH recognition unit. When co-cultured with macrophages supplemented with GSH or  $\text{ONOO}^-$  alone, GSH-ABAH exhibited minimal fluorescence. However, when the cells were co-cultured with GSH and SIN-1 ( $\text{ONOO}^-$ -donor) a strong fluorescence response was observed (Fig. 7(d)).

NO and  $\text{H}_2\text{S}$  are two vital gas signaling molecules in mammals, and the interplay between them is of great significance for understanding the pathological process of oxidative stress. Zhao *et al.* designed an activatable NIR-II fluorescent probe (BOD-NH-SC), which was used to visualize the intracellular dynamics of cellular NO and  $\text{H}_2\text{S}$  (Fig. 8).<sup>144</sup> BOD-NH-SC contained three parts: (i) *N*-methyl-2-methoxyaniline moiety as the NO-recognition site; (ii) 4-nitrobenzenethiol as  $\text{H}_2\text{S}$ -recognition site; (iii) boron dipyrromethene (BODIPY) was selected as the fluorophore. In the presence of NO, the *N*-nitroso product (BOD-NO-SC) generated a 214-fold increase in fluorescence at 655 nm. The process could be cycled, so it could accurately monitor the dynamics of NO and  $\text{H}_2\text{S}$  (Fig. 8(b)). Furthermore, the ability of BOD-NH-SC to detect endogenous NO/ $\text{H}_2\text{S}$  in cells was evaluated. The presence of endogenous NO in macrophages caused BOD-NH-SC to exhibit bright red fluorescence, while the NIR-II fluorescence was weak. However, after incubating with



**Fig. 6** (a) MPIBA modified with phenanthrimidazole and malononitrile and reactions with  $\text{ClO}^-$  and  $\text{HSO}_3^-$ . Confocal microscopic images were used to assess the dual role of intracellular  $\text{SO}_2$  in oxidative stress, HeLa cells were incubated with MPIBA (5  $\mu\text{M}$ ) for 30 min (b1–b5) and then incubated with 50  $\mu\text{M}$  BTSA for 60 min (c1–c5). 0.01 Units of MPO, 100  $\mu\text{M}$   $\text{H}_2\text{O}_2$  and 500 mM NaCl were added to cells and the mixture was further incubated for 1 h (d1–d5). HeLa cells were incubated with MPIBA (5  $\mu\text{M}$ ) for 30 min (e1–e5) and then with a media consisting of 0.01 Units of MPO, 100  $\mu\text{M}$   $\text{H}_2\text{O}_2$  and 500 mM NaCl for 1 h (f1–f5). Reproduced with permission from ref. 140. Copyright (2017) Elsevier B.V.



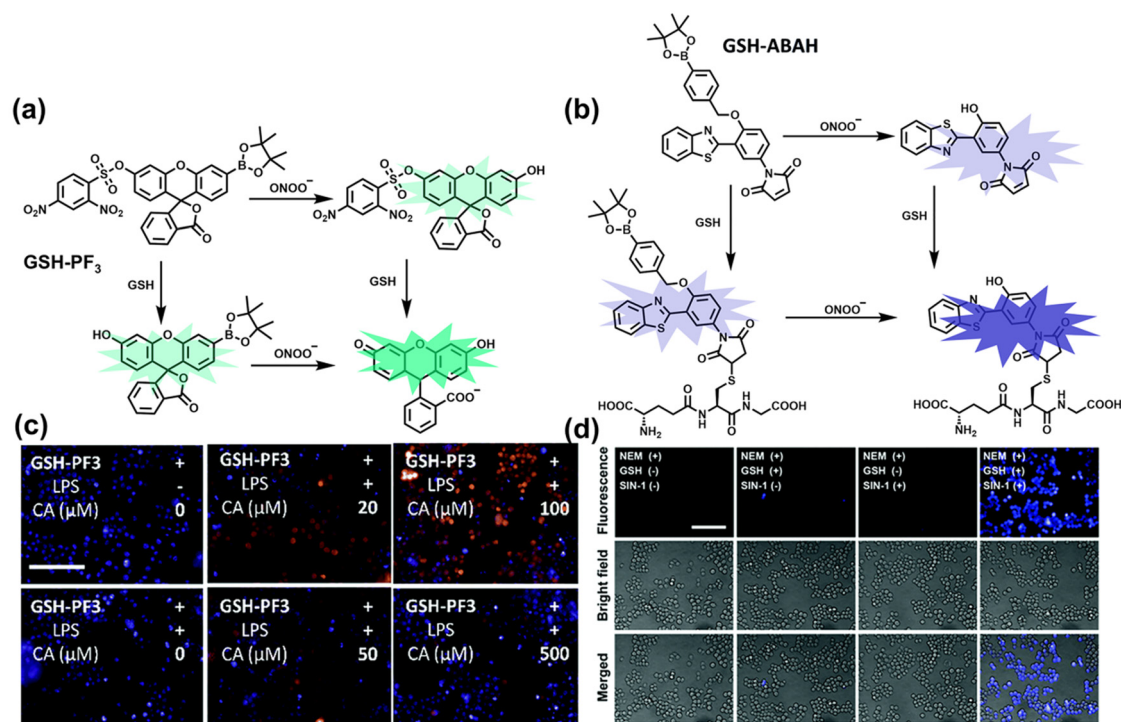


Fig. 7 (a) and (b) Fluorescence turn 'on' mechanism of GSH-PF<sub>3</sub> and GSH-ABAH in the presence of ONOO<sup>-</sup> and GSH. (c) Fluorescence imaging of RAW264.7 cells with GSH-PF<sub>3</sub> in the absence and presence of LPS, which elicits ONOO<sup>-</sup> and increasing caffeic acid. Reproduced with permission from ref. 142. from the Royal Society of Chemistry. (d) Fluorescence imaging of RAW264.7 cells with GSH-ABAH in the presence of exogenously added GSH and/or SIN-1. Reproduced with permission from ref. 143. from the Royal Society of Chemistry.

fluvastatin-stimulated macrophages (fluvastatin can stimulate cells to produce endogenous H<sub>2</sub>S), the fluorescence signal from the NIR-II channel increased by 16.2 times compared with the untreated cells.

### 3.3 RONS + related species

As the energy factory of life, oxidative stress and energy metabolism in mitochondria are vital biological events. Adenosine triphosphate is closely related to various physiological and pathological processes (apoptosis or necrosis).<sup>145</sup> Tian *et al.* reported a two-photon fluorescence-lifetime-based probe (TFP) (Fig. 9(a)), which could simultaneously measure H<sub>2</sub>O<sub>2</sub> and ATP levels in mitochondria.<sup>146</sup> In order to achieve dual fluorescence channel detection, rhodamine ( $\lambda_{\text{ex}} = 710 \text{ nm}$ ,  $\lambda_{\text{em}} = 550\text{--}650 \text{ nm}$ ) and naphthalimide derivatives ( $\lambda_{\text{ex}} = 710 \text{ nm}$ ,  $\lambda_{\text{em}} = 430\text{--}530 \text{ nm}$ ) were selected as the fluorophores. A benzyl boronic ester and diethylenetriamine were used as the recognition units for H<sub>2</sub>O<sub>2</sub> and ATP, respectively. Using fluorescence lifetime imaging, TFP exhibited a good linear relationship and selectivity for the detection of H<sub>2</sub>O<sub>2</sub> (LOD =  $68 \pm 5 \text{ nM}$ ) and ATP (LOD =  $33 \pm 2 \text{ μM}$ ). With its excellent imaging capabilities, TFP was used to visualize the dynamic changes of H<sub>2</sub>O<sub>2</sub> and ATP in neuronal mitochondria under different conditions (Fig. 9(b and c)). After being stimulated by O<sub>2</sub><sup>•-</sup> for a short period of time (8 min), the level of H<sub>2</sub>O<sub>2</sub> in neurons increased about 4-fold, while ATP decreased to 86% of the initial level. After replacing with new culture medium, ATP and H<sub>2</sub>O<sub>2</sub> in a parallel group returned to the initial levels within 16 min. However, long-term

(50 minutes) O<sub>2</sub><sup>•-</sup> (100 μM) stimulation can cause permanent oxidative damage and energy deficiency in neurons. Importantly, after 50 min of H<sub>2</sub>O<sub>2</sub> (100 μM) stimulation, the levels of mitochondrial H<sub>2</sub>O<sub>2</sub> and ATP still exhibited recovery. These results were ascribed to the fact that exogenous H<sub>2</sub>O<sub>2</sub> and O<sub>2</sub><sup>•-</sup> exhibit varying degrees of impact on mitochondrial function, whereas O<sub>2</sub><sup>•-</sup> displayed a more serious and negative impact.

Recently, based on rhodamine and 1,8-naphthalimide fluorophores, James *et al.* reported a probe (ATP-LW) that can simultaneously monitor changes in the levels of ATP and ONOO<sup>-</sup> in cells (Fig. 9(d)).<sup>147</sup> In the presence of ONOO<sup>-</sup>, the boronic ester was oxidatively removed to form 4-hydroxy-1,8-naphthalimide product NA-OH; in the presence of ATP, hydrogen bonding induced the opening of the spironolactone of rhodamine (Rh-Bpin). Due to the differences in emission between the two products, ATP-LW facilitated monitoring of the dynamic levels of ONOO<sup>-</sup> and ATP in the green ( $\lambda_{\text{ex}} = 488 \text{ nm}$ ,  $\lambda_{\text{em}} = 500\text{--}575 \text{ nm}$ ) and red ( $\lambda_{\text{ex}} = 514 \text{ nm}$ ,  $\lambda_{\text{em}} = 575\text{--}650 \text{ nm}$ ) channels, respectively. Moreover, ATP-LW was used to successfully visualize oxidative stress induced by oligomycin A (an ATP synthase inhibitor) in hepatocytes and an increase of ONOO<sup>-</sup> levels and reduction of ATP during APAP-induced hepatotoxicity. This research not only provided a general molecular design strategy for multi-species imaging, but also illustrated that mitochondrial oxidative stress was closely related to energy metabolism.

Simultaneous, and sequential detection of multiple analytes by a single fluorescent probe is an important and hot area for development. At present, there are relatively few dual-responsive probes. Almost all of them are based on cyanine, rhodamine,



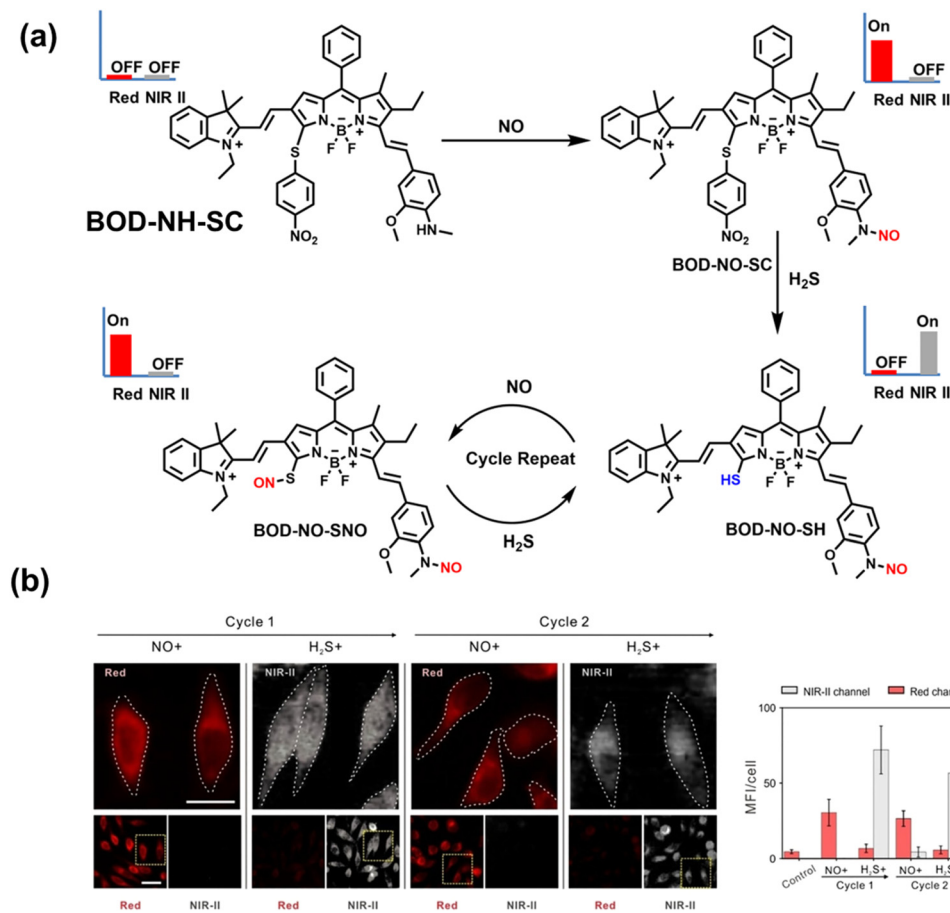


Fig. 8 (a) The mechanism for reversible detection of NO and H<sub>2</sub>S by BOD-NH-SC. (b) Using BOD-NH-SC to alternately image NO and H<sub>2</sub>S in HepG2 cell. Reproduced with permission from ref. 144. Copyright (2021) Wiley-VCH Verlag GmbH & Co. KGaA, Weinheim.

fluorescein and coumarin as the fluorophore skeleton, with RONSS recognition groups attached. Real-time monitoring of multiple target analytes in different disease models or designated areas of organisms is an important direction for development of this type of fluorescent probe in the future. For example, the simultaneous detection of A $\beta$  protein/Tau protein and RONSS in the brain is beneficial for the early diagnosis of neurodegenerative diseases; the simultaneous detection of enzymes and RONSS is beneficial for the diagnosis of tumors and inflammation, as well as pathological research; different RONSS assays in liver/kidney are beneficial for evaluating drug-induced organ damage and pathological studies of related diseases. Therefore, such multi-species assays may help improve the clinical value of fluorescent probes (Table 2).

## 4. Fluorescent probes for imaging inflammation and organ oxidative damage

When subjected to external stimuli, an organism protectively initiates some physiological reactions related to oxidative stress. Usually these physiological processes are beneficial, but continuous high levels of RONSS stimulation can induce a variety of diseases. Given that inflammation and oxidative

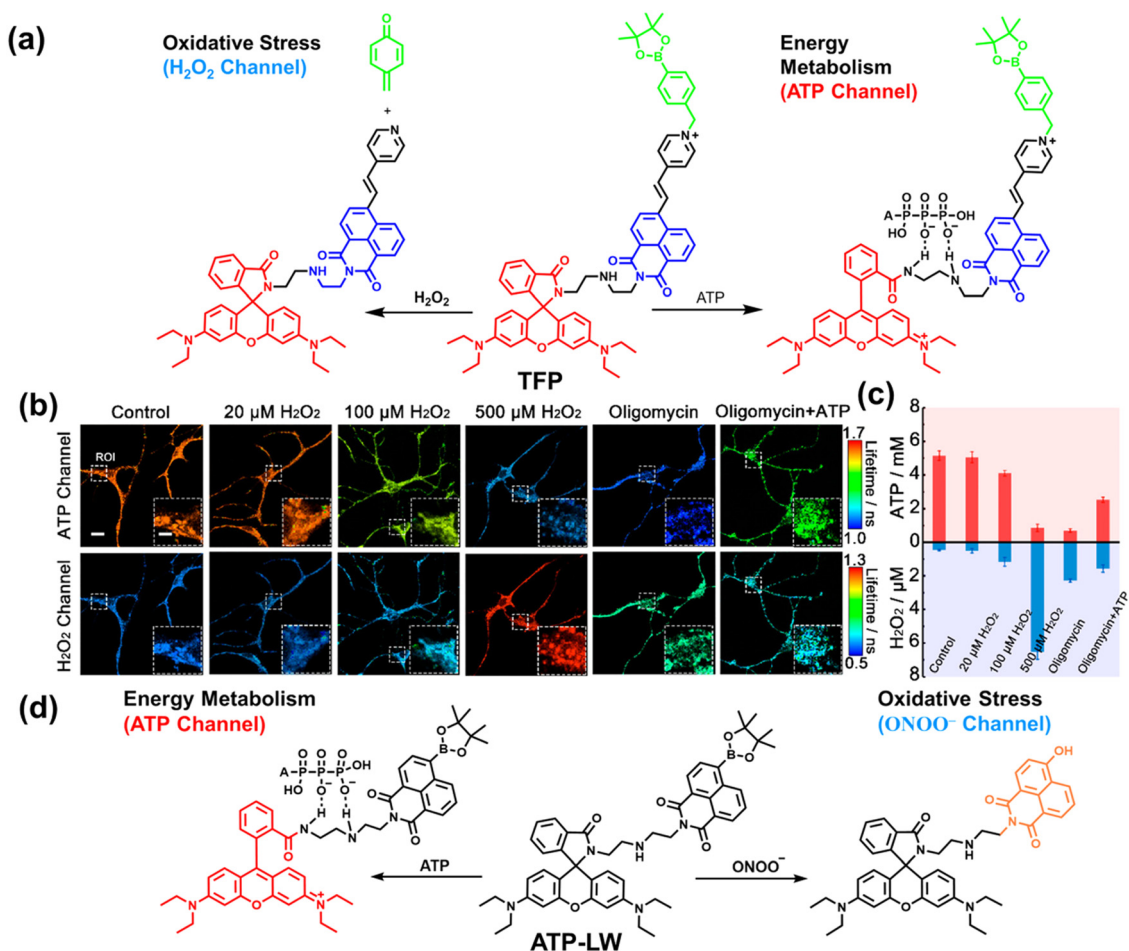
damage of organs are common physiological pathological processes, here we introduce some representative fluorescent probes for RONSS imaging of inflammation and organ injury induced by different conditions.

### 4.1 Inflammation

Inflammation is a nonspecific immune reaction when the body suffers any type of injury.<sup>148</sup> Inflammation cannot be regarded as a disease, but as a special biological process.<sup>149</sup> According to the way induced, inflammation can be divided into two types: infectious inflammation and aseptic inflammation. Infectious inflammation is mainly caused by the invasion of microorganisms such as bacteria, fungi, and viruses, while aseptic inflammation is related to chronic diseases, trauma, radiation, and chemical damage.<sup>150,151</sup> Importantly, both types of inflammation are closely related to oxidative stress.<sup>152</sup> When damage is detected, a cascade of signals lead to the recruitment of inflammatory cells, such as neutrophils and macrophages. These cells will produce RONS, proteases and growth factors leading to tissue destruction, fibroblast proliferation and fibrosis.<sup>153</sup> However, long-term exposure to high levels of oxidants inevitably causes oxidative damage to normal tissues and cells (such as protein oxidation and lipid peroxidation),







**Fig. 9** (a) Fluorescence turn 'on' mechanism of TFP in the presence of  $\text{H}_2\text{O}_2$ /ATP. (b) Fluorescence lifetime images of neurons with the addition of  $\text{H}_2\text{O}_2$  (20, 100, and 500  $\mu\text{M}$ ) and oligomycin (An ATP synthase inhibitor) in the channels of  $\text{H}_2\text{O}_2$  and ATP. (c) Summarized data for mitochondrial  $\text{H}_2\text{O}_2$  and ATP changes in neurons toward different treatments. Reproduced with permission from ref. 146. Copyright (2020) American Chemical Society. (d) Fluorescence turn 'on' mechanism of ATP-LW in the presence of  $\text{ONOO}^-$ /ATP.

and even cause chronic inflammatory diseases, such as cancer, diabetes, stroke, atherosclerosis and so on.<sup>154–159</sup> Therefore, monitoring and understanding inflammation can help us better understand these diseases and develop better treatments. As a direct result, a significant number of fluorescent probes are being explored for the real-time imaging of oxidative stress in various inflammation models.

**4.1.1 Infectious inflammation.** Bacterial infection can cause severe inflammation, which is one of the important health problems that affect people all over the world. Tang *et al.* designed an activatable fluorescent nanoprobe (TPE-IPB-PEG) with AIE emission characteristics that was used to accurately image  $\text{ONOO}^-$  at the site of inflammation in bacterially infected mice.<sup>160</sup> The small-molecule fluorescent probe (TPE-IPB) was composed of three parts: the host fluorophore a tetra-phenyl, the imine was the fluorescence quenching group and emission mediator, and the benzyl boronic ester was the recognition site for  $\text{ONOO}^-$  (Fig. 10(a)). In the presence of  $\text{ONOO}^-$ , the newly formed phenolic hydroxyl group could form an intramolecular hydrogen bond with the lone pair of electrons on the nitrogen atom of the imine, thereby inhibiting the

fluorescence quenching of the imine. Given that nanoparticles can preferentially accumulate in the inflammation area through EPR (Enhanced Permeability and Retention), a biocompatible lipid – PEG2000 was used to encapsulate TPE-IPB generating a uniform sphere with a diameter of about 30 nm (Fig. 10(b)). Through tail vein injection, the nanoparticles can effectively accumulate at the inflammation site of methicillin-resistant *Staphylococcus aureus* (MRSA) infected mice and generate a fluorescence output (Fig. 10(c)). According to tissue analysis, the fluorescence intensity of the sites infected with bacteria were at least 5.7-fold higher than that of other tissue regions. Significantly, by using antibiotics to treat the inflammation of the mice, the fluorescence intensity for the inflamed areas was significantly reduced. However, since the emission wavelength of the TPE-IPB cannot reach near-infrared wavelengths, its further application for *in vivo* imaging was limited.

**4.1.2 Aseptic inflammation.** Like inflammation induced by bacterial infection, aseptic inflammation is responsible for detrimental effects on people's health, and this type of inflammation often exists for a long time without acute symptoms. Rotenone, bacterial endotoxin lipopolysaccharide (LPS) and pro-inflammatory



**Table 2** Summary of references, chemical structures, maximum absorption/emission wavelengths (TP: two-photon), analytes, detection limit, and application in cells

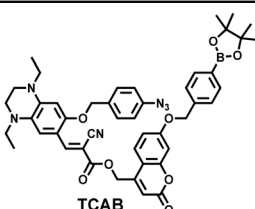
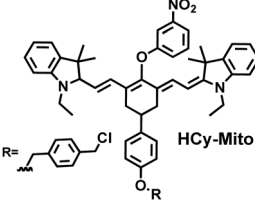
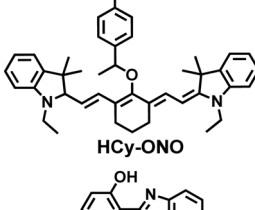
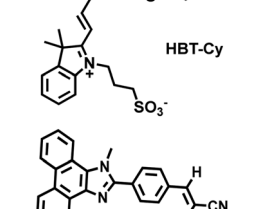
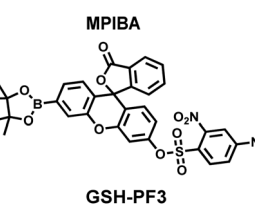
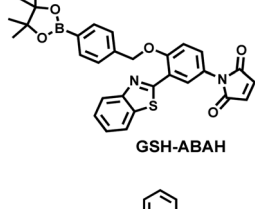
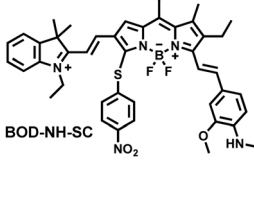

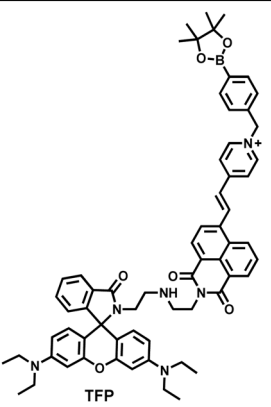
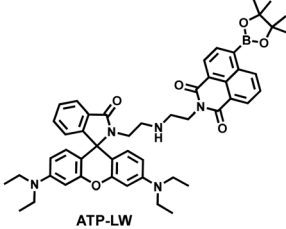
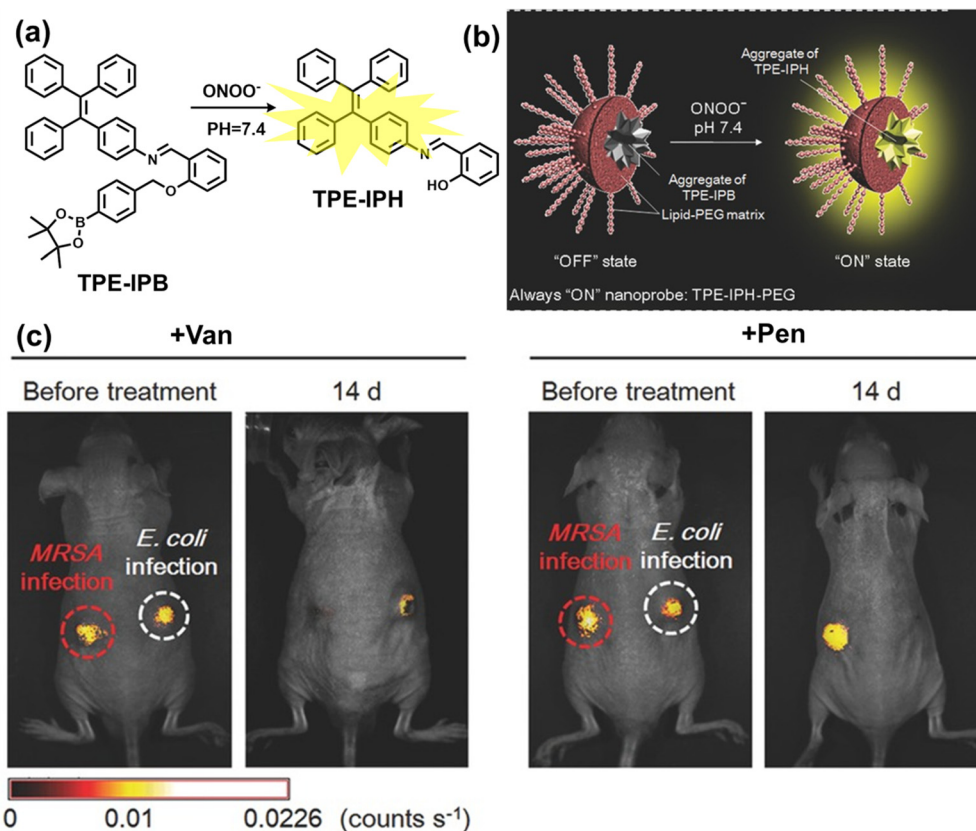
Ref.	Chemical structure	Analyte	Response time	Detection limit ( $\mu\text{M}$ )	$\lambda_{\text{ex}}/\lambda_{\text{em}}$ (nm)	Application in cells
133	 TCAB	$\text{H}_2\text{S}$ $\text{H}_2\text{O}_2$	80 min 120 min	0.058 0.044	325/413, 475/627 325; 486/413	Monitor dynamic $\text{H}_2\text{O}_2$ and $\text{H}_2\text{S}$ redox processes in living cells
135	 HCy-Mito	$\text{O}_2^{\bullet-}$ $\text{H}_2\text{S}_n$	10 min 10 min	0.05 0.08 $\mu$	730/780 730/770	Monitor dynamic $\text{H}_2\text{O}_2$ and $\text{H}_2\text{S}_n$ redox processes in living cells
136	 HCy-ONO	$\text{O}_2^{\bullet-}$ $\text{H}_2\text{S}_n$	150 s 5 min	0.09 0.1	730/785 500/635	Detection $\text{H}_2\text{O}_2$ and $\text{H}_2\text{S}_n$ in living cell models under continuous hypoxic and intermittent hypoxic conditions (IRI),
138	 HBT-Cy	$\text{HSO}_3^-$ $\text{H}_2\text{O}_2$	15 min 60 min	0.34 —	520/590 520/590	Reversible monitoring of changes in dynamic levels of $\text{SO}_2$ and $\text{H}_2\text{O}_2$ in cells.
140	 MPIBA	$\text{SO}_2$ $\text{ClO}^-$	60 s; Seconds	0.035 0.125	440/625 363/410 373/500	Explore the dual role of $\text{SO}_2$ in cells (oxidative stress)
142	 GSH-PF3	$\text{ONOO}^-$ GSH	— 5–10 min	— —	488/512 488/512	Monitor the co-existence of metabolically produced $\text{ONOO}^-$ and GSH living cells
143	 GSH-ABAH	$\text{ONOO}^-$ GSH	30 s 30 s	— —	390/451 390/451	Monitor the co-existence of metabolically produced $\text{ONOO}^-$ and GSH living cells
144	 BOD-NH-SC	NO $\text{H}_2\text{S}$	5 min 10 min	0.031 0.02	570/655 806/936	Reversible monitoring of changes in dynamic levels of NO and $\text{H}_2\text{S}$ in cells.



Table 2 (continued)

Ref.	Chemical structure	Analyte	Response time	Detection limit ( $\mu\text{M}$ )	$\lambda_{\text{ex}}/\lambda_{\text{em}}$ (nm)	Application in cells
146		$\text{H}_2\text{O}_2$ ATP	8 min 2 min	$0.068 \pm 0.005$ $33 \pm 2$	380/470 TP710/470 562/590 TP710/590	Visualization of the dynamic level changes of mitochondrial $\text{H}_2\text{O}_2$ and ATP induced by the superoxide anion ( $\text{O}_2^{\bullet-}$ ).
147		$\text{ONOO}^-$ ATP	1 min 100 min	0.026 63	450/562 488/568 520/587	Visualize an increase of $\text{ONOO}^-$ levels and depletion of ATP in cells during APAP-induced hepatotoxicity



**Fig. 10** (a) Fluorescence turn 'on' mechanism of TPE-IPB towards  $\text{ONOO}^-$ . (b) Schematic illustration of TPE-IPB-PEG and the performance after incubation with  $\text{ONOO}^-$ . (c) *In vivo* fluorescence images of both MRSA and *E. coli*-infected mice before and after antibiotic treatment for 14 days. Reproduced with permission from ref. 160. Copyright (2016) Wiley-VCH Verlag GmbH & Co. KGaA, Weinheim.



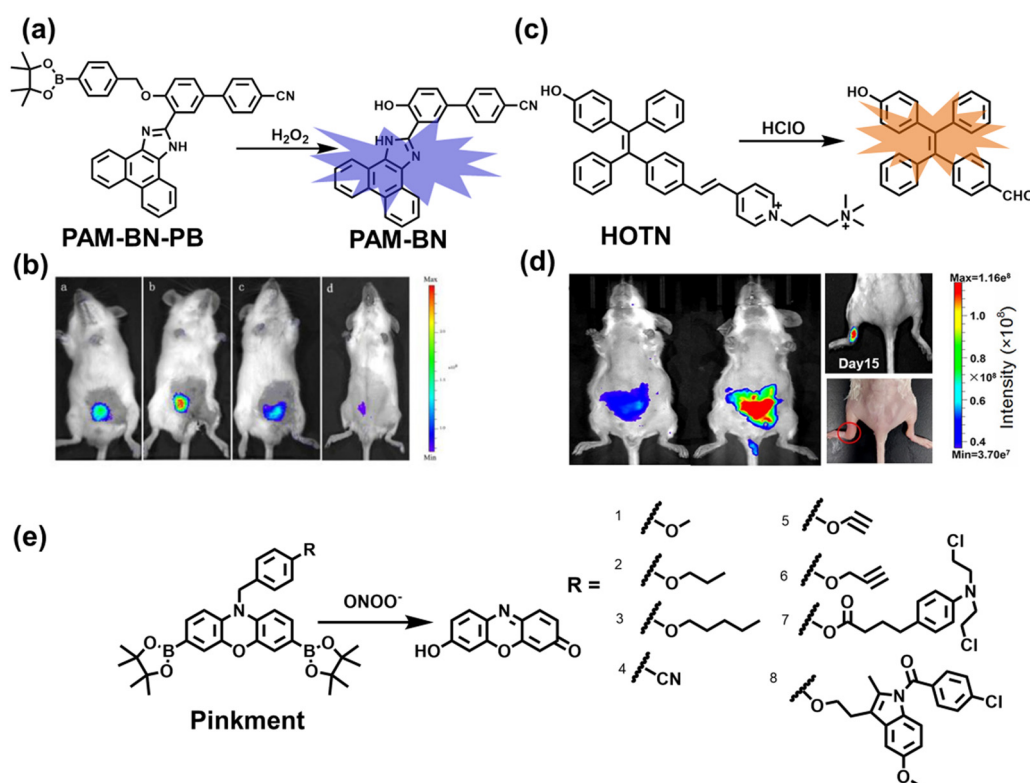


cytokine interferon- $\gamma$  (IFN- $\gamma$ ) are commonly used drugs to simulate aseptic inflammation in the laboratory.

Wang *et al.* reported a fluorescent probe (PAM-BN-PB) for the rapid imaging of  $\text{H}_2\text{O}_2$  in mice with peritonitis (Fig. 11).<sup>161</sup> PAM-BN-PB consists of three parts: phenanthroimidazole, benzonitrile and benzyl boronic ester (Fig. 11(a)). The strong electron withdrawing effect of benzonitrile accelerated the nucleophilic reaction of the phenyl borate with  $\text{H}_2\text{O}_2$ . Compared with the usual probes for detecting  $\text{H}_2\text{O}_2$ , PAM-BN-PB could shorten the response time to within 10 minutes. Importantly, by using this probe in a rotenone-induced peritonitis model, the fluorescence intensity of the mouse abdomen was significantly enhanced, which indicated a positive correlation between peritonitis and  $\text{H}_2\text{O}_2$  (Fig. 11(b)). Furthermore, Wang *et al.* reported a tetrastylene-based AIE fluorescent probe (HOTN) (Fig. 11(c)), which was used to visualize  $\text{HClO}$  signals in mouse models for peritonitis, arthritis, and liver cancer.<sup>162</sup> By attaching strong hydrophilic groups to the TPE backbone, the fluorescence intensity was almost completely quenched in an aqueous environment. In the presence of  $\text{HClO}$ , the pyridine salt and quaternary ammonium salt side chain undergoes oxidative cleavage to form a stable aldehyde group, the increase in hydrophobicity and the intermolecular hydrogen bond between the hydroxyl group and the aldehyde group significantly enhanced the AIE effect of HOTN, resulting in a significant increase in the fluorescence intensity ( $>1000$  times). HOTN

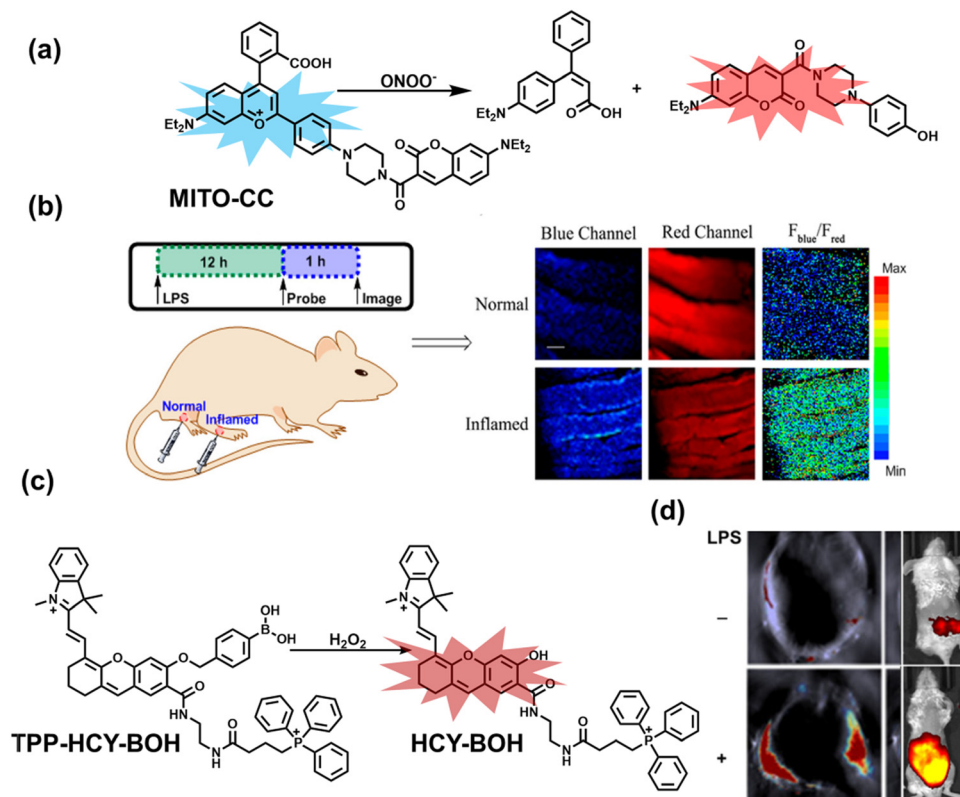
exhibited low detection limit ( $0.108\ \mu\text{M}$ ) and short response time (within a few seconds). Finally, this study successfully highlighted the use of fluorescent probes for monitoring the abdomen of peritonitis mice and the joints of the legs of arthritic mice (Fig. 11(d)).

James *et al.* developed a fluorescent platform called Pinkment for the visualization of  $\text{ONOO}^-$  in a LPS-induced peritonitis mouse model and the evaluation of the therapeutic effect of indomethacin.<sup>163</sup> Resorufin was chosen as the fluorophore due to its red-shift fluorescence and the easy functionalization of the scaffold, while a boronic ester served as the  $\text{ONOO}^-$  recognition group (Fig. 11(e)). Importantly, the benzyl unit could be functionalized with different functional units without affecting the selectivity towards ROS. Eight kinds of fluorescent probes with different substituents were prepared using this platform, all of which exhibited high selectivity and sensitivity for  $\text{ONOO}^-$ . Among them, Pinkment-2, 5, and 6 ( $R = 2, 5, 6$ ), were used to image exogenous and endogenous  $\text{ONOO}^-$  in HeLa and RAW 264.7 macrophages. Significantly, the fluorescence intensity of Pinkment-8 ( $R = 8$ ) conjugated with the indomethacin in inflammatory macrophages was significantly lower than the control group, indicating that this probe could reduce the inflammation by releasing indomethacin. In addition, the fluorescence intensity of alkyne-functionalized Pinkment-6 ( $R = 6$ ) in an acute inflammation mouse model was significantly higher than that of healthy mice, which provided direct evidence for a link between acute inflammation and  $\text{ONOO}^-$ .



**Fig. 11** (a) Structures of PAM-BN-PB and sensing mechanism for discrimination of  $\text{H}_2\text{O}_2$ . (b) PAM-BN-PB was used for fluorescence imaging of rotenone-induced peritonitis in mice. Reproduced with permission from ref. 161. Copyright (2017) American Chemical Society. (c) Structures of HOTN and sensing mechanism for discrimination of  $\text{ClO}^-$ . (d) Fluorescence imaging of HOTN in peritonitis and arthritis. Reproduced with permission from ref. 162. Copyright (2020) American Chemical Society. (e) Structures of Pinkment and sensing mechanism for discrimination of  $\text{ONOO}^-$ .





**Fig. 12** (a) Fluorescence turn 'on' mechanism of MITO-CC in the presence of ONOO<sup>-</sup>. (b) Fluorescence imaging of MITO-CC in mouse arthritis tissue and healthy tissue respectively. Reproduced with permission from ref. 165. Copyright (2017) American Chemical Society. (c) Fluorescence turn 'on' mechanism of TPP-HCY-BOH in the presence of H<sub>2</sub>O<sub>2</sub>. (d) TPP-HCY-BOH was used for photoacoustic and fluorescence imaging of peritonitis mice and healthy mice. Reproduced with permission from ref. 166. Copyright (2020) American Chemical Society.

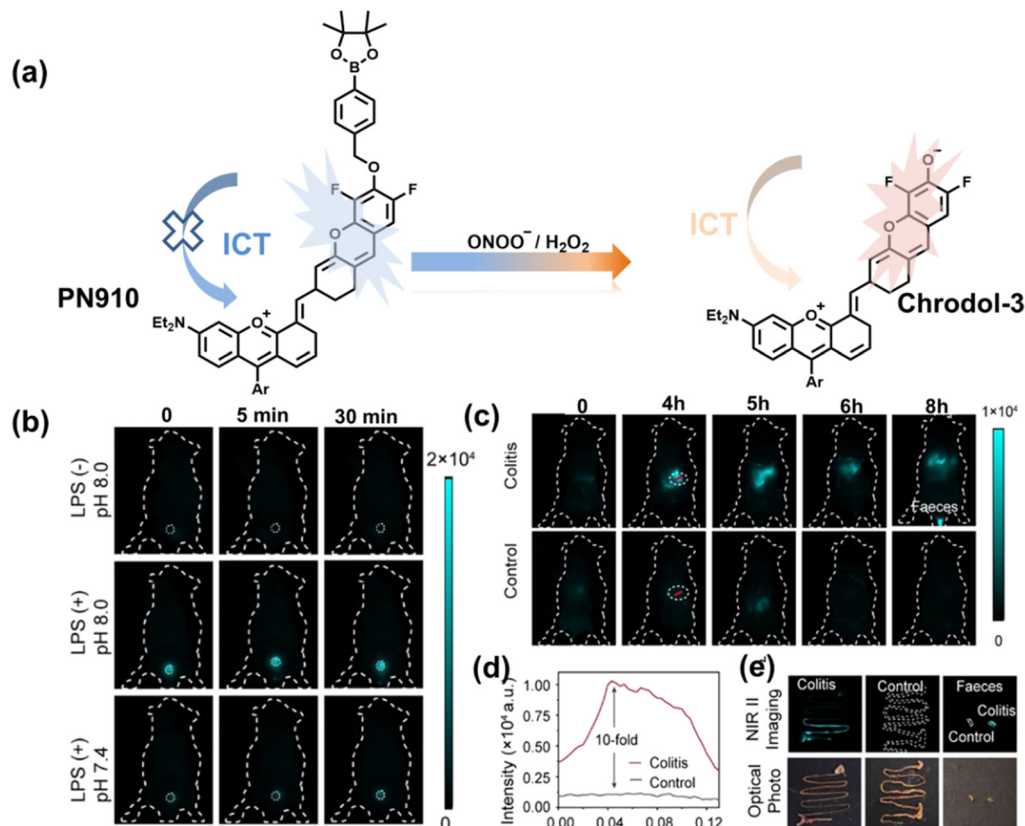
Ratiometric probes designed based on fluorescence resonance energy transfer (FRET) are ideal tools for the quantitative detection of biomolecules. The two emission bands facilitate calibration, and reduces false results caused by the dose, environment, and excitation intensity.<sup>164</sup> Chang *et al.* reported a two-photon ratiometric fluorescence probe (MITO-CC), for the ratiometric detection of ONOO<sup>-</sup> in cells and for inflammation mouse models (Fig. 12(a)).<sup>165</sup> MITO-CC was composed of two parts: a rhodamine derivative with good selectivity for ONOO<sup>-</sup> was selected as the energy acceptor, while coumarin with excellent optical properties was selected as the energy donor. When ONOO<sup>-</sup> was present, the emission peak of MITO-CC centered at 651 nm almost disappeared, while the emission peak at 451 nm was significantly enhanced. In addition, MITO-CC exhibited low detection limit (11.30 nM), rapid response time (within 20 s), good biocompatibility and excellent mitochondrial targeting ability. As such, MITO-CC was used for the ratiometric visualization of changes in the levels of ONOO<sup>-</sup> in LPS/IFN- $\gamma$ -stimulated cells, living liver tissues, and inflammation mouse models (Fig. 12(b)).

Although fluorescence imaging exhibits high sensitivity and contrast, most non-NIR fluorescent probes are unsuitable for *in vivo* imaging due to the limitation of the excitation and emission wavelengths, the depth of tissue penetration and the spatial resolution. Therefore, dual-modal probes with fluorescence and

photoacoustic imaging capabilities can combine the high spatio-temporal resolution of ultrasound with the high contrast of optical imaging. Hai *et al.* reported a mitochondrial targeting probe (TPP-HCY-BOH), which was successfully used for fluorescence/photoacoustic (FL/PA) dual-mode imaging of H<sub>2</sub>O<sub>2</sub> overproduction *in vivo* during inflammation.<sup>166</sup> TPP-HCY-BOH was composed of three parts: (i) NIR dye HCY with excellent fluorescence and photoacoustic properties as the fluorophore; (ii) benzyl boronic acid the recognition group for H<sub>2</sub>O<sub>2</sub>; (iii) positively charged triphenylphosphine (TPP) as the mitochondrial targeting group (Fig. 12(c)). TPP-HCY-BOH exhibited a low limit of detection (LOD = 0.348  $\mu$ M), good biocompatibility and excellent mitochondrial targeting (colocalization coefficient = 0.91). TPP-HCY-BOH was used to identify excess H<sub>2</sub>O<sub>2</sub> produced in mitochondria and achieved a 2.4-fold increase in fluorescence signal and a 4.7-fold increase in photoacoustic signal. Moreover, TPP-HCY-BOH was used for FL/PA dual-modal imaging of H<sub>2</sub>O<sub>2</sub> in LPS-induced acute abdominal inflammation of mice. Compared with the control group, the fluorescence signal was increased by 5.2-fold, while the photoacoustic signal was increased by 7.1-fold (Fig. 12(d)).

Additionally, due to the advantages of minimal background fluorescence and deep tissue penetration depth, fluorescence imaging in the second near-infrared window (NIR-II, 900–1700 nm) is a strong candidate for future diagnosis of pathological inflammation in the clinic. Zhang *et al.* recently reported a





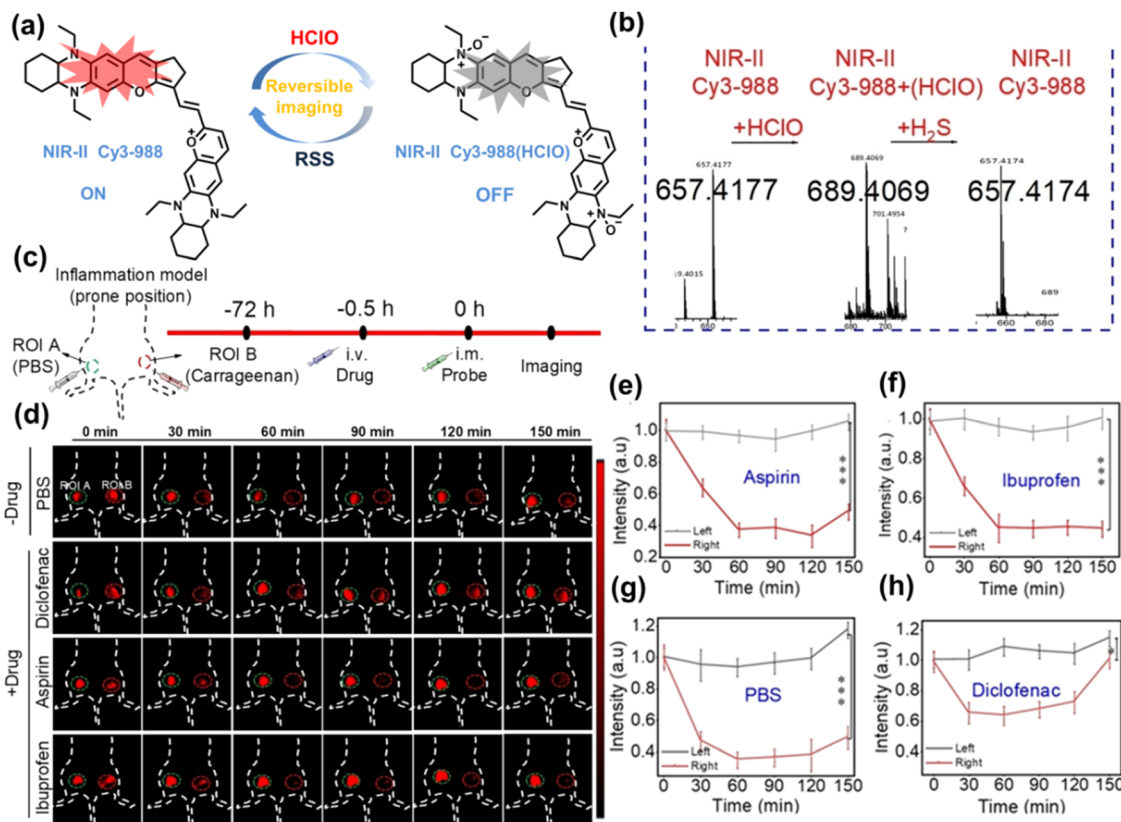
**Fig. 13** (a) Fluorescence turn 'on' mechanism of PN910 in an alkaline environment in the presence of  $\text{H}_2\text{O}_2/\text{ONOO}^-$ . (b) NIR-II fluorescence imaging of  $\text{H}_2\text{O}_2/\text{ONOO}^-$  in cystitis mice at different times and under different conditions. (c) NIR-II fluorescence imaging of  $\text{H}_2\text{O}_2/\text{ONOO}^-$  in colitis mice at different times and under different conditions. (d) The fluorescence intensity profiles (red line Rol) of colitis mice and healthy mice at 4 h. (e) *In vitro* NIR II fluorescence images and optical photographs of colons and feces from colitis mice and healthy mice. Reproduced with permission from ref. 167. Copyright (2021) Wiley-VCH Verlag GmbH & Co. KGaA, Weinheim.

dual-activatable fluorescent probe (PN910) in the NIR-II window, which could respond to  $\text{H}_2\text{O}_2$  and  $\text{ONOO}^-$  with high selectivity in an alkaline inflammatory environment (Fig. 13).<sup>167</sup> A series of hydroxyl-containing merocyanines with NIR-II fluorescence were prepared, which were named chrodol 1–3 according to the number of *ortho*-fluorines (0, 1, 2). Amongst them, chrodol 3 was selected as the fluorophore due to exhibiting the highest fluorescence quantum yield (0.34%) and excellent  $\text{pK}_a$  (6.40). A benzyl boronic ester was used as the recognition group for  $\text{H}_2\text{O}_2/\text{ONOO}^-$  (Fig. 13(a)). The probe could rapidly and selectively respond to low levels of  $\text{H}_2\text{O}_2$  and  $\text{ONOO}^-$  in an alkaline environment ( $\text{pH} > 7.4$ ). During the real-time imaging of cystitis, PN910 exhibited a 1.5-fold increase in fluorescence signal in a physiological environment ( $\text{pH} = 8.0$ ) (Fig. 13(b)). During the imaging of enteritis, the fluorescence signal in the colon of mice with acute colitis was almost 10 times higher than that of the control group (Fig. 13(c–e)). This research provides a unique method for real-time, high-contrast and non-invasive monitoring of RONS in an alkaline inflammatory environment *in vivo*.

Yuan *et al.* recently reported a new class of trimethine skeleton NIR-II fluorophores (NIR-II Cy3s), which could serve as an effective platform for the reversible monitoring of the  $\text{HClO}/\text{RSS}$ -mediated redox process in a pathophysiology environment

(Fig. 14a).<sup>168</sup> NIR-II Cy3-988, modified with the 1,4-diethyl-decahydroquinoxaline group at both the donor and acceptor ends, exhibited the longest excitation and emission wavelengths ( $\lambda_{\text{ex}}/\lambda_{\text{em}} = 988/1058 \text{ nm}$ ). In addition, the electron-rich nature of the 1,4-diethyl-decahydroquinoxaline group provides a reversible oxidation site within the probe. In the presence of  $\text{HClO}$ , the maximum absorption and emission peaks of NIR-II Cy3-988 are significantly reduced, while a new blue-shifted absorption band appeared at 824 nm. In the presence of  $\text{H}_2\text{S}$ , the absorption (980 nm) and fluorescence signal (1040 nm) of NIR-II Cy3-988 was recovered. This process can be effectively cycled 4 times and was demonstrated by high resolution mass spectrometry (Fig. 14b). The researchers further used NIR-II Cy3-988 to assess oxidative stress and the therapeutic effects of three drugs (aspirin, ibuprofen and diclofenac) in a model of acute inflammation (Fig. 14c and d). Compared to the left leg of mouse (healthy), the fluorescence intensity of the right hind leg (carrageenan-induced acute inflammatory model) experienced a rapid decrease over the first 30 min (Fig. 14e–h). This result indicated the presence of high levels of  $\text{HClO}$  in areas of acute inflammation. Notably, diclofenac exhibited the best anti-inflammatory effect, significantly restoring the carrageenan-induced reduction in NIR-II fluorescence signal. A plausible explanation was that diclofenac rapidly





**Fig. 14** (a) The mechanism for reversible detection of HClO and H<sub>2</sub>S by NIR-II Cy3-988; (b) the reversible mechanism of NIR-II Cy3-988 for HClO and H<sub>2</sub>S was investigated by high-resolution mass spectrometry. (c) Schematic of fluorescence imaging of carrageenan-induced acute inflammation and drug-mediated repair using NIR-II Cy3-988. (d) After treatment with PBS, diclofenac, aspirin, or ibuprofen, NIR-II fluorescence imaging of hind legs is performed at representative time points of carrageenan-induced acute inflammatory models. The left hind leg is the control group and the right hind leg is the experimental group. (e–h) After treatment with aspirin (e), ibuprofen (f), PBS (g) diclofenac (h), the fluorescence intensity of NIR-II Cy3-988 in the acute inflammatory model was at representative time points. Reproduced with permission from ref. 168. Copyright (2022) Wiley-VCH Verlag GmbH & Co. KGaA, Weinheim.

inhibited the recruitment of neutrophils to reduce myeloperoxidase (MPO) and macrophage accumulation.

As a common pathological and physiological process, real-time monitoring of oxidative stress induced by inflammation is of great significance for investigating the pathology and early diagnosis of related diseases. Considering possible clinical needs in the future, we believe that NIR-II fluorescent probes, targeting specific areas or organs, drug safety evaluation, and application for more types of inflammation models are areas requiring additional research.

#### 4.2 Organ injury

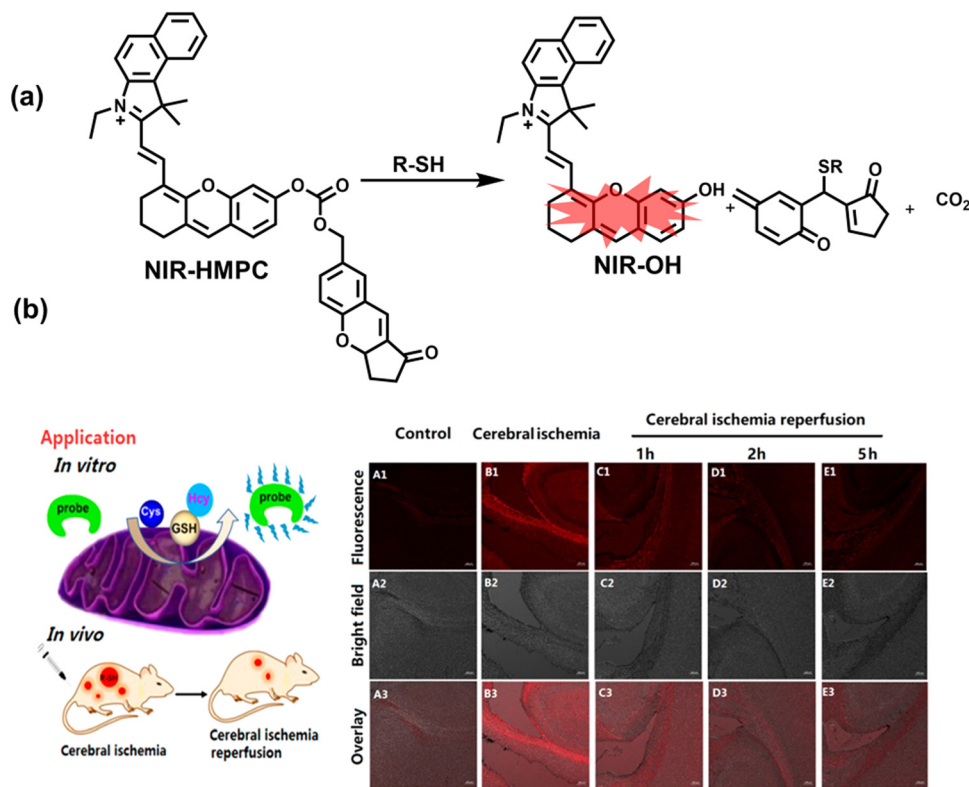
Oxidative stress can activate intracellular signals and destroy a variety of active components, thereby inducing cell over differentiation and apoptosis leading to organ dysfunction.<sup>169</sup> Ischemia/Reperfusion Injury (IRI) and drug-induced organ injury are closely related to oxidative stress.<sup>170,171</sup> IRI is a common clinical complication, which is caused by long-term ischemic injury of vital organs and secondary injury induced by blood perfusion recovery of ischemic organs.<sup>172</sup> Although the pathogenesis of IRI includes many factors, IRI-induced bursts of reactive oxygen species in the mitochondria play a key role in

destroying cellular components and triggering cell death.<sup>170</sup> Clinical drugs for various diseases, including acetaminophen (APAP), *cis*-platinum (*cis*-diamminedichloroplatinum), and anthracyclines, have been shown to induce oxidative damage in different organs.<sup>171</sup> In order to evaluate the side effects of IRI and drugs on organs, the detection of alanine aminotransferase in the blood and positron emission computed tomography (PET) imaging are commonly used.<sup>173,174</sup> Compared with these methods, fluorescence imaging as a safe, non-invasive and sensitive imaging method can achieve precise imaging of specific oxidants and reductants at the injured site through the use of appropriately designed probes, therefore providing a new and effective technology to evaluate the drug toxicity and recovery after surgery. As such, many fluorescent probes are being developed to study IRI and drug-induced organ oxidative damage.

**4.2.1 Ischemia/reperfusion injury (IRI).** As one of the high-rate metabolic organs, the brain is particularly vulnerable to the adverse effects of IRI-induced oxidative stress.<sup>175</sup> When IRI occurs, an excessive production of RONS in the mitochondria will induce the death of neuronal cells and cause brain damage. As the main antioxidants, thiols play a vital role in this process.







**Fig. 15** (a) Fluorescence turn 'on' mechanism of NIR-HMPC in the presence of thiols. (b) NIR-HMPC was used for fluorescence imaging of endogenous thiols in cerebral ischemia (2 h) and reperfusion brain tissue slices at different times (1–5 h). Reproduced with permission from ref. 176. Copyright (2020) American Chemical Society.

In order to observe the fluctuation of thiol levels during oxidative stress, apoptosis and cerebral ischemia/reperfusion in real time, Yin *et al.* designed a NIR fluorescent probe (NIR-HMPC) based on the hemicyanine dye and chromene.<sup>176</sup> NIR-HMPC was composed of two parts: (i) hemicyanine dye O-HD as the host NIR fluorophore; (ii) 7-hydroxymethyl-2,3-dihydro-1*H*-cyclopenta[*b*]chromene-1-one as the recognition site (Fig. 15(a)). Even in a complex physiological environment, NIR-HMPC could specifically, rapidly and sensitively respond to a variety of thiols in the mitochondria through a nucleophilic reaction. The probe was used to image the dynamic changes of thiols during 2 h of brain ischemia followed by 5 h reperfusion (Fig. 15(b)). The results indicated that oxidative stress induced by ischemia could increase the level of thiols in the brain of mice. As the blood perfusion time increased, the level of thiols returned to normal.

Glutathione is the most abundant thiol in cells. Significant reduction of GSH levels can lead to severe mitochondrial damage and induce a variety of diseases.<sup>177</sup> Chen *et al.* designed and synthesized a novel NIR fluorescent probe (BCy-SeSe) based on BCy-Keto fluorophore and GSH-specific diselenide or disulfide recognition group (Fig. 16(a)).<sup>178</sup> As the perfusion time was extended, the fluorescence intensity of BCy-SeSe in cells and (adult/aging) mouse brains decreased significantly. Similarly, the activity of GSH peroxidase in the brain was also reduced. Low levels of glutathione were positively correlated with aggravation of apoptosis and cerebral infarction, these observations were more significant in the aged group.

I/R injury often occurs in liver surgery and has become one of the important factors affecting the success rate of surgery and postoperative survival.<sup>179</sup> In order to explore the relationship between liver I/R injury and O<sub>2</sub><sup>•−</sup> concentrations, Chen *et al.* developed a NIR fluorescent probe (Mito-Cy-Tfs) based on heptamethine cyanine fluorophore and trifluoromethanesulfonamide recognition group (Fig. 16(b)).<sup>180</sup> Using the co-incubation of Mito-Cy-Tfs with cells subjected to different perfusion methods, it was found that compared with glucose or serum deprivation/reperfusion, hypoxia/reperfusion was the main factor that induces apoptosis. When Mito-Cy-Tfs was used to image O<sub>2</sub><sup>•−</sup> in a liver model of I/R mice, a significant increase in the fluorescence signal indicated that I/R could induce bursts of O<sub>2</sub><sup>•−</sup> in the liver and severe liver tissue damage. The fluorescence intensity in the liver region was significantly reduced after ischemic preconditioning (IPC) and postconditioning (IPTC), suggesting that these measures can protect the liver from oxidative damage. In addition to O<sub>2</sub><sup>•−</sup>, H<sub>2</sub>O<sub>2</sub> is considered as an important oxidative stress marker in liver I/R. As such Chen *et al.* developed a NIR fluorescent probe (Cy-ArB) based on heptamethine cyanine fluorophore and benzyl boronic ester (Fig. 16(c)) and used the probe to image the changes in H<sub>2</sub>O<sub>2</sub> levels in the mitochondria and mouse liver during I/R.<sup>181</sup> Confocal imaging indicated that the fluorescence intensity of the cells in the glucose–serum–oxygen deprivation/reperfusion group was significantly higher than that of the control group. A significant increase in the rate of cell apoptosis indicated that the I/R process induces an increase in the level of

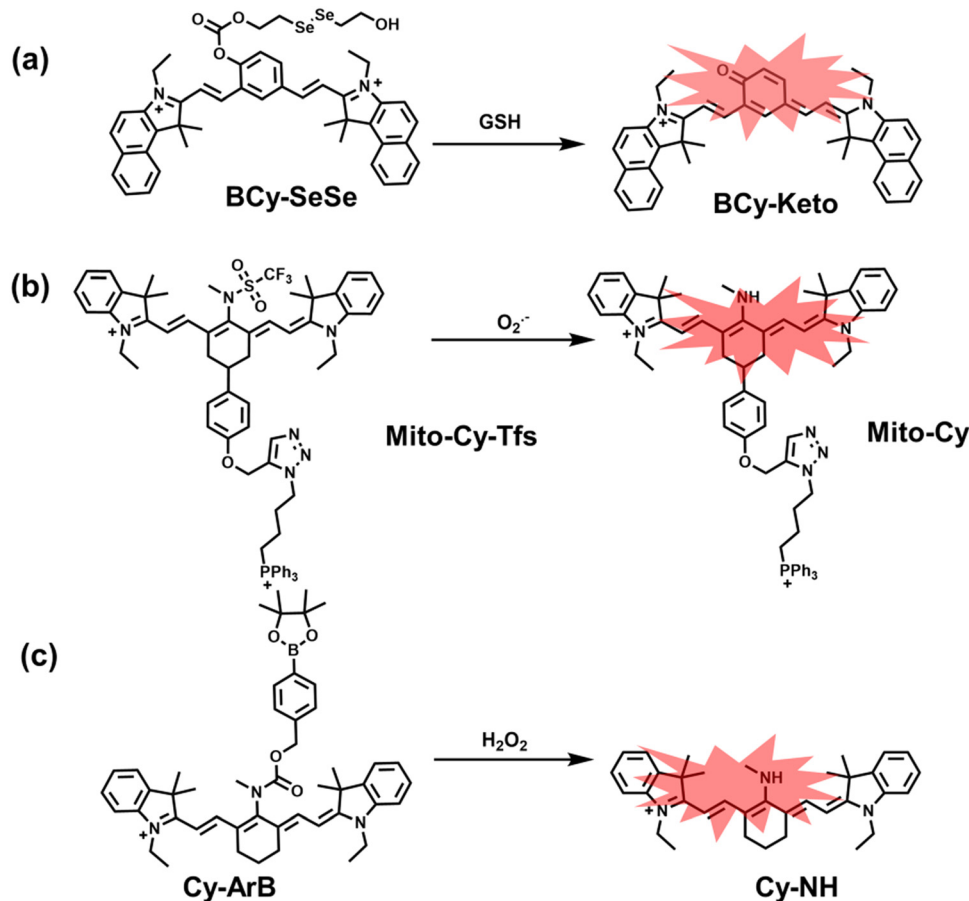


Fig. 16 (a) Structures of BCy-SeSe and sensing mechanism for discrimination of GSH. (b) Structures of Mito-Cy-Tfs and sensing mechanism for discrimination of  $O_2^{\bullet-}$ . (c) Structures of Cy-ArB and sensing mechanism for discrimination of  $H_2O_2$ .

$H_2O_2$ , leading to cell oxidative damage. In addition, the fluorescence signal of the liver of I/R mice increases with the time of ischemia (0.5–2.5 h) and the perfusion time (3–6 h). Confirming that the process of liver ischemia and reperfusion in mice can induce  $H_2O_2$  bursts and organ oxidative damage.

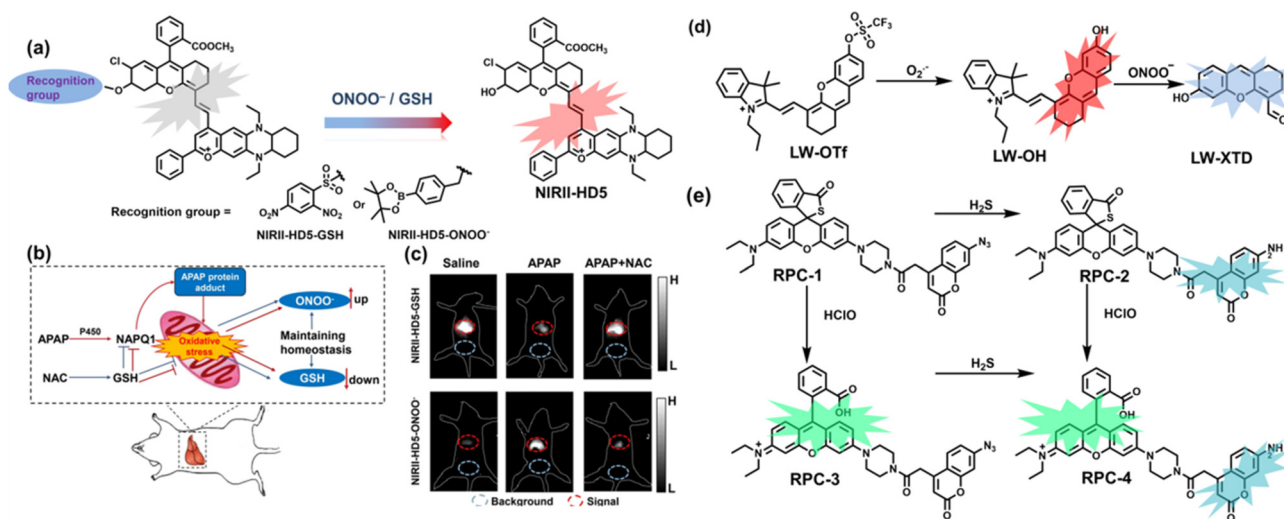
**4.2.2 Drug-induced organ injury.** The liver is an important organ for human metabolism. According to World Health Organization (WHO) statistics, drug-induced liver injury (DILI) has risen to be the fifth leading worldwide cause of death from liver disease.<sup>182</sup> With the continuous development of modern medicine, DILI has become an important indicator in drug toxicity evaluations.<sup>183</sup> A common cause of DILI is the excessive use of acetaminophen (APAP, a commonly used antipyretic/analgesic drug) that causes severe oxidative stress in the liver.<sup>184</sup>

To achieve high-contrast real-time imaging of DILI *in vivo*, Yuan *et al.* developed an efficient activatable NIR-II platform.<sup>185</sup> Compared with the previously reported hemicyanine dye O-HD, a 1,4-diethyl-decahydroquinoxaline (DQ) benzopyran group with electron-rich characteristics replaces the original indole heterocycle; the introduction of a chlorine atom at the *ortho*-position of the hydroxyl group reduces the  $pK_a$  and the benzoic acid or methyl benzoate at the 9-position of the xanthene ring improves the stability of the fluorophore. Amongst the NIRII-HDs platforms prepared, NIRII-HD5 was selected for *in vivo*

imaging due to its high molar absorptivity, excellent quantum yield (0.28%) and  $pK_a$  (6.5) (Fig. 17(a)). Two NIR-II probes (NIRII-HD5-ONOO<sup>-</sup> and NIRII-HD5-GSH) responsive to ONOO<sup>-</sup> and GSH were developed by introducing benzyl boronic ester and 2,4-dinitrobenzenesulfonyl recognition groups at the hydroxyl position (Fig. 17(a)). In the liver of mice injected with excess APAP, the fluorescence signal of NIRII-HD5-ONOO<sup>-</sup> achieved a 2-fold enhancement, while the fluorescence signal of NIRII-HD5-GSH was only 60% of the control group (Fig. 17(b) and (c)). In addition, when mice were injected with excessive APAP and hepatoprotective drug *N*-acetylcysteine (NAC) at the same time, the fluorescence signals of the two probes in the liver were almost restored to the level of the control group (Fig. 17(c)). These results indicated that excessive use of APAP induces abnormal levels of ONOO<sup>-</sup> and depletion of GSH in the liver, while NAC can effectively improve DILI. This research provided a versatile NIR-II fluorescence platform for real-time imaging of DILI.

Considering that DILI is often involved in abnormally elevated levels of ROS and RNS oxidants, James *et al.* developed LW-OTf for monitoring the dynamic levels of  $O_2^{\bullet-}$  and ONOO<sup>-</sup> in the liver of DILI mice.<sup>186</sup> LW-OTf consists of two parts: (i) hemicyanine-based NIR emitting fluorophore LW-OH; (ii)  $O_2^{\bullet-}$  reactive trifluoromethylsulfonyl (triflyl, Tf) recognition group.





**Fig. 17** (a) Based on the NIR-II-HD5 structure, two probes were designed for ONOO<sup>-</sup> and GSH detection, respectively. (b) Schematic illustration of APAP-induced liver injury and treatment with *N*-acetyl cysteine (NAC). (c) NIR-II fluorescence imaging of NIR-II-HD5-GSH and NIR-II-HD5-ONOO<sup>-</sup> in mouse liver regions under different stimulation conditions. (d) Structures of LW-OTf and sensing mechanism for discrimination of O<sub>2</sub><sup>•-</sup> and ONOO<sup>-</sup>. (e) Structures of RPC-1 and sensing mechanism for discrimination of HClO and H<sub>2</sub>S. Reproduced with permission from ref. 185. Copyright (2022) Wiley-VCH Verlag GmbH & Co. KGaA, Weinheim.

In the presence of O<sub>2</sub><sup>•-</sup>, the triflyl group was deprotected to release the NIR fluorophore LW-OH (Fig. 17(d)). Subsequently, ONOO<sup>-</sup> could be added to remove the indole heterocycle and formed the fluorophore LW-XTD which exhibited two-photon properties. Bright red and blue fluorescence could be observed in cells stimulated by cisplatin and APAP, respectively. In the liver area of DILI mice, both near-infrared fluorescence signals and two-photon fluorescence signals increased with an increase in the dose of APAP, which indicated that an overdose of APAP can cause abnormally high levels of ROS and RNS in the liver area. This study provided direct evidence for a positive correlation between APAP-induced DILI and oxidative stress.

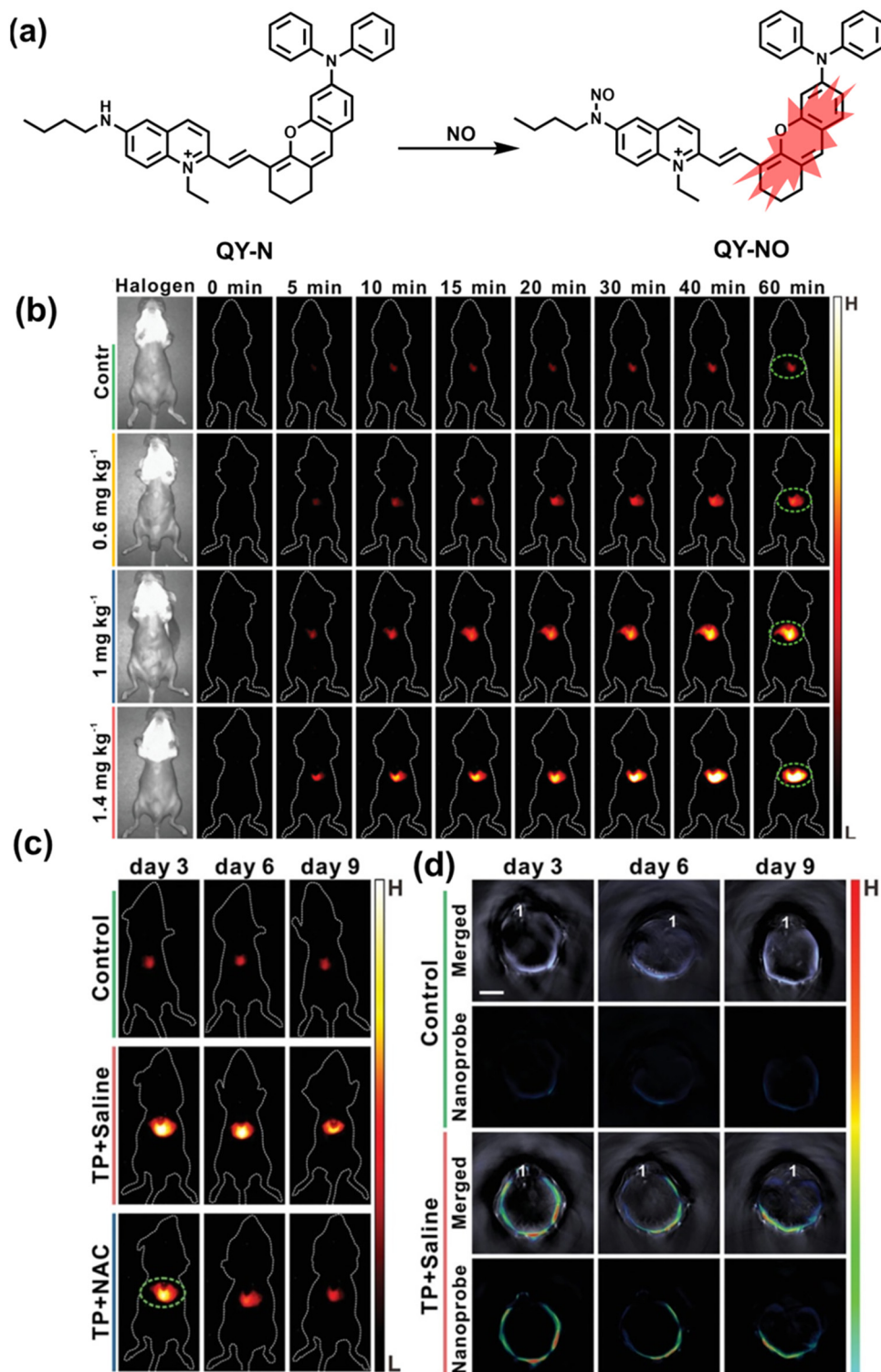
Unlike the low hepatotoxicity induced by a single administration, the wrong combination of some drugs can significantly increase liver injury. Tang *et al.* developed a two-photon fluorescent probe (RPC-1) that can simultaneously image HClO and H<sub>2</sub>S then evaluated the liver damage and relief caused by duloxetine and fluoxetine (antidepressants).<sup>187</sup> RPC-1 consists of two parts: (i) thiorhodamine ( $\lambda_{\text{em}} = 580 \text{ nm}$ ) that specifically responds to HClO; (ii) 7-aminocoumarin with an azide group that specifically responds to H<sub>2</sub>S ( $\lambda_{\text{em}} = 445 \text{ nm}$ ) (Fig. 17(e)). Using RPC-1 to image cells and mouse liver regions, the use of a single drug (duloxetine or fluoxetine) resulted in a slight increase in fluorescence signal and did not cause significant liver damage. However, a combination of the two drugs (duloxetine and fluoxetine) could significantly increase the fluorescence intensity ( $\lambda_{\text{em}} = 580 \text{ nm}$ ) of the green channel, which indicated a significant up-regulation of HClO levels and significant liver injury. Furthermore, *N*-acetylcysteine (NAC) pretreatment could significantly increase the fluorescence intensity of the blue channel ( $\lambda_{\text{em}} = 445 \text{ nm}$ ) and decrease the fluorescence intensity of green channel and mouse liver area. This result indicated that NAC pretreatment could lead to an increase of endogenous H<sub>2</sub>S levels to alleviate liver injury.

Herbs are widely used in health care and the treatment of chronic diseases, but excessive or incorrect use may cause severe liver injury.<sup>188</sup> The overexpression of NO is closely related to liver inflammation caused by liver injury. Wu *et al.* designed a dual-modal activatable probe (QY-N) to detect triptolide (TP)-induced liver injury using photoacoustic imaging and NIR-II fluorescence imaging.<sup>189</sup> QY-N was composed of three parts: (i) bismethoxyphenyl-amine-containing dihydroxanthene was selected as the electron donor; (ii) a quinolinium acted as an electron acceptor; (iii) butylamine acted as a NO recognition group and fluorescence quencher (Fig. 18(a)). When NO was present in the liver, QY-NO the nitrosation product of the imine, exhibited a red-shift in the absorption band (700–850 nm) for photoacoustic imaging and a strong emission (910–1110 nm) for NIR-II fluorescence imaging. Notably, the NIR-II fluorescence of QY-N was significantly enhanced in triptolide-induced liver injured mice and was positively correlated with the dosage of the drug (Fig. 18(b)). The spatio-temporal information provided by three-dimensional multispectral optoacoustic tomography (MSOT) images was able to size and locate the liver injury. In addition, after continuous use of the therapeutic drug *N*-acetylcysteine (NAC) (3 days, 6 days and 9 days), the fluorescence and photoacoustic signals in the liver area of the mice was significantly reduced (Fig. 18(c and d)).

The kidney plays a vital role in removing wastes and toxins from the body. However, the kidney often suffers from drug induced injury. At present, the commonly used clinical methods for monitoring acute kidney injury (AKI), such as blood tests (serum creatinine (CREA) and blood urea nitrogen (BUN)), have problems of low sensitivity and are slow.<sup>190,191</sup> As such, the emergence of FL/PA dual-modality imaging probes provides an effective way to solve these problems.

Cisplatin is a widely used anticancer drug. Tan *et al.* designed and synthesized a mitochondrial-targeted FL/PA dual-modal probe (SiRho-HD) based on hemicyanine dyes and Si-rhodamine dyes





**Fig. 18** (a) Structures of QY-N and sensing mechanism for discrimination of NO. (b) Representative NIR-II fluorescence images at different time points for DILI mice from different groups. (c) Representative NIR-II fluorescent images of the mice from the control group, the “TP + Saline” group and the “TP + NAC” group at 3 days, 6 days and 9 days. (d) Representative cross-sectional MSOT images of the livers from the different groups of mice at 3 days, 6 days and 9 days. Reproduced with permission from ref. 189. Copyright (2021) Wiley-VCH Verlag GmbH & Co. KGaA, Weinheim.

(Fig. 19(a)) and used the probe to image endogenous  $\text{ONOO}^-$  of cisplatin-induced AKI mice.<sup>192</sup> In the presence of  $\text{ONOO}^-$ , SiRho-HD exhibited ratiometric fluorescence, based on the FRET

principle. The specific oxidation of the hemicyanine dye resulted in a reduction of the PA signal and release of Si-rhodamine fluorescence. Confocal imaging indicated that the fluorescence



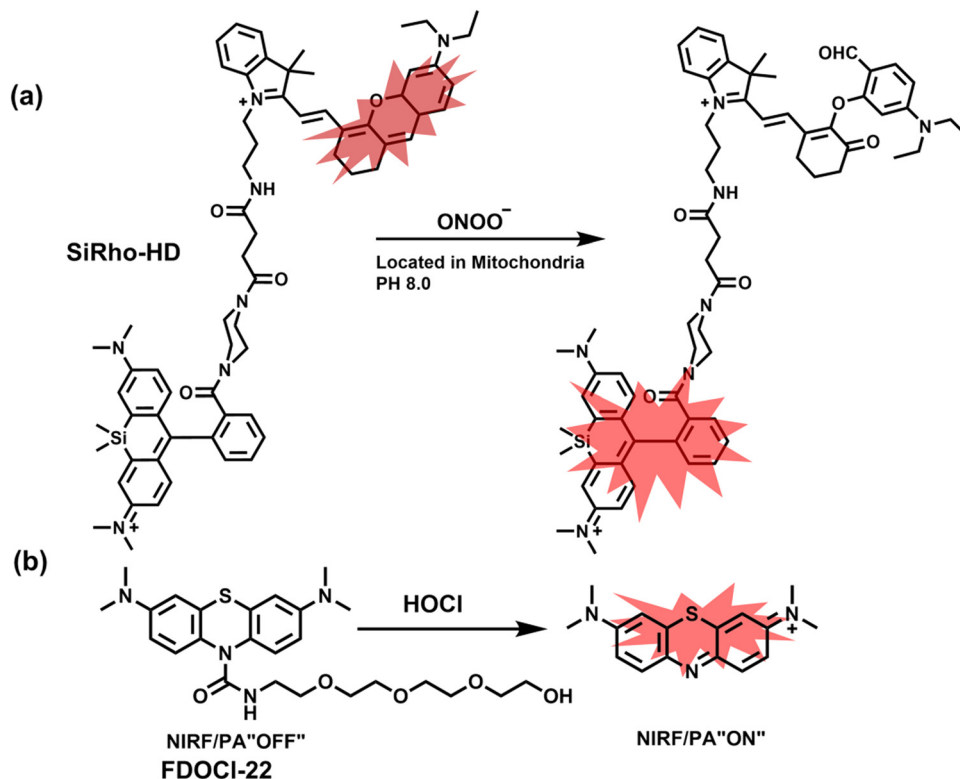


Fig. 19 (a) Structures of SiRho-HD and sensing mechanism for discrimination of  $\text{ONOO}^-$ . (b) Structures of FDOCI-22 and sensing mechanism for discrimination of  $\text{HOCl}$ .

intensity of SiRho-HD in the green channel ( $\lambda_{\text{em}} = 645\text{--}710\text{ nm}$ ) was enhanced, and the fluorescence intensity of the red channel was significantly reduced ( $\lambda_{\text{em}} = 720\text{--}780\text{ nm}$ ) for HK-2 cells in a cisplatin-caused nephrotoxicity model. The signal intensity was positively correlated with the concentration of cisplatin. In general, molecules with high hydrophilicity tend to be enriched in the kidney. The PA and fluorescence signals of the hemicyanine of SiRho-HD in the kidney area of the cisplatin-induced AKI mouse decreased, and the fluorescence signal intensity of SiR increased.

Hypochlorous acid is considered to be closely related to cisplatin-induced AKI. To monitor endogenous  $\text{HOCl}$  in the kidney area of drug-induced AKI mice, Yi *et al.* developed a water-soluble fluorescent/photoacoustic dual-modal probe (FDOCI-22) based on methylene blue (MB) and urea derivatives with long glycol chains (Fig. 19(b)).<sup>193</sup> In the presence of  $\text{HOCl}$ , the cleavage of the amide bond releases MB, which significantly enhanced the absorption and emission signals. Combined with confocal imaging, the fluorescence intensity of FDOCI-22 in cisplatin-stimulated macrophages was significantly increased, and the apoptosis rate was positively correlated with the dosage of cisplatin. Moreover, FDOCI-22 was specifically enriched in the kidneys, and the fluorescence and photoacoustic signals of a cisplatin-induced AKI mouse model were significantly enhanced. Under the same dosage and incubation time, FDOCI-22 could detect AKI 24 h earlier than the standard clinical method (Table 3).

## 5. Fluorescent probes for oxidative stress imaging in diseases

It is known that oxidative stress is closely related to the pathophysiological process of many diseases. However, there has been a lack of effective means for real-time imaging of oxidative stress *in vivo*. To better meet the requirements of medical and clinical research, real-time imaging for the pathological process using fluorescent probes for various diseases is an important area that needs additional development. Considering the biological environment and the background fluorescence of biological tissues, skin and blood, a limited number of fluorescent probes have been used for *in vivo* imaging of related diseases. Therefore, we selected several diseases closely related to oxidative stress, such as neurodegenerative diseases, epilepsy, depression, diabetes, and cancer, where the application of fluorescent probes in monitoring these diseases has been achieved.

### 5.1 Alzheimer's disease

Alzheimer's disease (AD), as the most common neurodegenerative disease, poses a serious threat to human health and is a large economic burden on society.<sup>194</sup> The most common clinical symptoms of AD patients are short-term and long-term memory loss, as well as the deterioration of progressive learning, reasoning, exercise, and communication skills as the disease develops.<sup>195</sup> The extracellular amyloid plaques formed by abnormal accumulation of  $\beta$ -amyloid and neurofibrillary tangles formed by the deposition



**Table 3** Summary of references, chemical structures, maximum absorption/emission wavelengths, analytes, detection limit, and application in pathological process

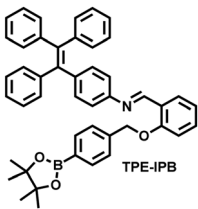
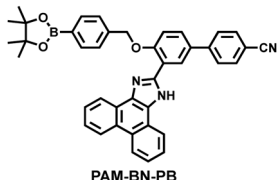
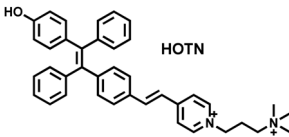
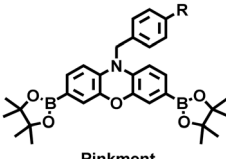
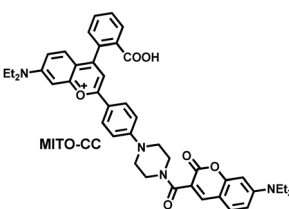
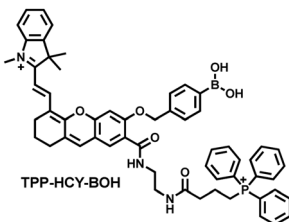
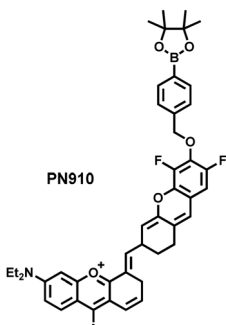
Ref.	Chemical structure	Analyte	Response time	Detection limit ( $\mu\text{M}$ )	$\lambda_{\text{ex}}/\lambda_{\text{em}}$ (nm)	Application in pathological process
160	 TPE-IPB	$\text{ONOO}^-$	30 min	100	377/538	Accumulate at the inflammation site of mice and visualize an increase of $\text{ONOO}^-$ levels
161	 PAM-BN-PB	$\text{H}_2\text{O}_2$	8 min	0.148	410/480	Visualisation of $\text{H}_2\text{O}_2$ levels in ischemia-reperfusion injured cells and mice with peritonitis.
162	 HOTN	$\text{ClO}^-$	30 s	0.108	350/535	Visualisation of $\text{HClO}$ signalling in mouse models of peritonitis, arthritis and hepatocellular carcinoma.
163	 Pinkment	$\text{ONOO}^-$	—	—	550/590	Visualization of $\text{ONOO}^-$ in a LPS-induced peritonitis mouse and the evaluation of the drug
165	 MITO-CC	$\text{ONOO}^-$	20 s	0.0113	420/651 420/473	Visualization of changes in the levels of $\text{ONOO}^-$ in cells, liver tissues, and inflammation mouse model
166	 TPP-HCY-BOH	$\text{H}_2\text{O}_2$	30 min	0.348	685/716	FL/PA dual-modal imaging of $\text{H}_2\text{O}_2$ in LPS-induced acute abdominal inflammation of mice.
167	 PN910	$\text{H}_2\text{O}_2/\text{ONOO}^-$	—	—	870/908	Visualization of changes in the levels of $\text{H}_2\text{O}_2$ and $\text{ONOO}^-$ in an alkaline inflammatory environment (cystitis and acute colitis)



Table 3 (continued)

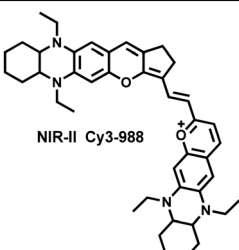
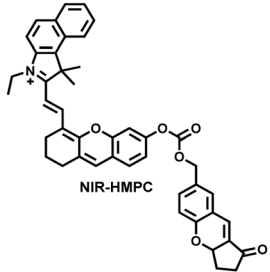
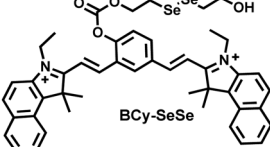
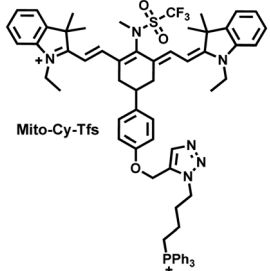
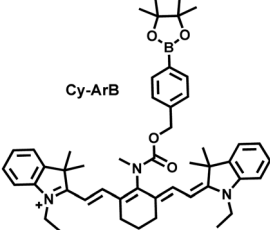
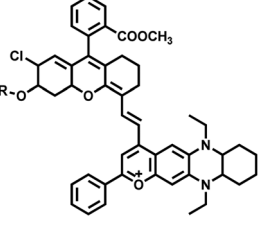
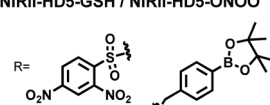
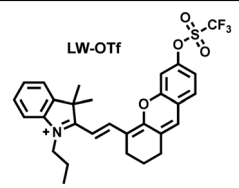
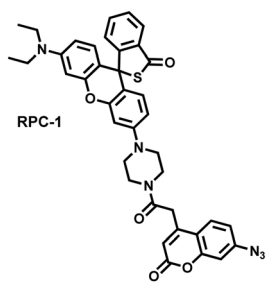
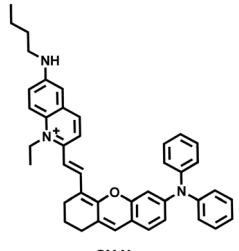
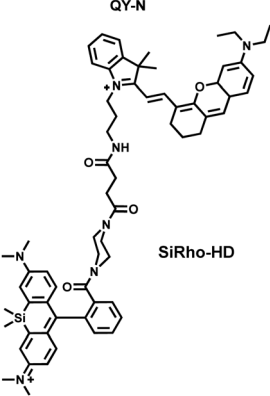
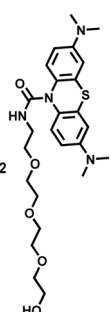
Ref.	Chemical structure	Analyte	Response time	Detection limit ( $\mu\text{M}$ )	$\lambda_{\text{ex}}/\lambda_{\text{em}}$ (nm)	Application in pathological process
168		HClO H <sub>2</sub> S	— —	0.056 0.046	988/1058 824/No fluorescent signal 980/1040	Reversible monitoring of the HClO/RSS-mediated redox process in a model of acute inflammation
176		RSH (Cys, Hcy, GSH)	93 s 85 s 88 s	0.39 0.54 0.59	711/731	Real-time observation of fluctuations in thiol levels during apoptosis and cerebral ischaemia/reperfusion in the mouse brain
178		GSH	80 s	20	654/728	Visualization of mitochondrial GSH changes during the cerebral I/R process.
180		O <sub>2</sub> <sup>•−</sup>	180 s	10	762/790 606/742	Real-time imaging of O <sub>2</sub> <sup>•−</sup> Concentration in liver of I/R mice model
181		H <sub>2</sub> O <sub>2</sub>	70 min	20	780/806 605/758	Visualization of mitochondrial the fluctuations of H <sub>2</sub> O <sub>2</sub> in cells and <i>in vivo</i> during the I/R process
185		GSH ONOO <sup>−</sup>	— —	15.8 0.08	854/895, 936 854/895, 936	Evaluated the redox potential of liver tissue during a liver injury <i>in vivo</i>
						



Table 3 (continued)

Ref.	Chemical structure	Analyte	Response time	Detection limit ( $\mu\text{M}$ )	$\lambda_{\text{ex}}/\lambda_{\text{em}}$ (nm)	Application in pathological process
186		$\text{O}_2^{\bullet-}$ $\text{ONOO}^-$	10 min —	0.465 0.382	675/710 360/461	Visualization of an increase in levels of both $\text{O}_2^{\bullet-}$ and $\text{ONOO}^-$ in mouse livers during APAP-induced DILI
187		$\text{HClO}$ $\text{H}_2\text{S}$	Seconds 900 s	0.0198 0.192	360/445 545/580	Simultaneously image $\text{HClO}$ and $\text{H}_2\text{S}$ then evaluated the liver damage and relief caused by duloxetine and fluoxetine
189		$\text{NO}$	10 min	0.023	780/935	Visualization of herbal-medicine-induced liver injury by detecting hepatic $\text{NO}$
192		$\text{ONOO}^-$	200 s	0.36	635/750 635/680	Mapping the fluctuation of $\text{ONOO}^-$ in cisplatin-induced acute kidney injury
193		$\text{HOCl}$	25 s	0.0207	664/680	Mapping the fluctuation of $\text{ONOO}^-$ in cisplatin-induced acute kidney injury

of tau protein in neurons are the main histopathological features of AD.<sup>196,197</sup> In addition to the pathological brain aggregation of proteins, the homeostasis of metal ions, oxidative stress, and loss of cholinergic transmission are also considered as important

pathogenic factors for AD.<sup>198</sup> As a disease involving multiple pathological processes, the current treatment plans for a single pathological factor have all failed.<sup>199,200</sup> However, significant evidence has pointed to the important role played by oxidative stress





which may together with other pathological factors promote the emergence and progression of AD. Schubert *et al.* found that A $\beta$  protein increased the levels of H<sub>2</sub>O<sub>2</sub> and lipid peroxides, which gradually accumulated in cells.<sup>201</sup> Butterfield *et al.* found that H<sub>2</sub>O<sub>2</sub> and carbonyl protein levels increased in various AD transgenic mice (carrying APP and PS-1 mutants) models and were directly related to soluble A $\beta$  levels.<sup>202</sup> In addition, Markesbery *et al.* found abnormal levels of Cu, Zn, and Fe in the hippocampus and amygdala of AD patients, and these areas exhibited severe histopathological changes.<sup>203</sup> In fact, abnormal levels of Fe/Cu in organisms can directly react with oxygen to produce superoxide anions, leading to the production of H<sub>2</sub>O<sub>2</sub>. At present, an explanation of the specific link between oxidative stress and pathological factors remains unknown. Therefore, fluorescent probes are urgently required to help provide new insight and facilitate new approaches for solving these problems.

A $\beta$  peptides activate microglia to produce high levels of ONOO<sup>−</sup> causing oxidative damage to neurons.<sup>204</sup> Considering the complex biological environment in the AD brain, James *et al.* developed a class of 3-hydroxyflavone boronate-based fluorescent probes (Fig. 20(a)), in particular 3-HF could respond ratiometrically to ONOO<sup>−</sup> after binding to A $\beta$  aggregates (*I*<sub>530</sub>/*I*<sub>420</sub>).<sup>205</sup> In order to evaluate the potential for *in vivo* application, 3-HF was used for the fluorescence imaging of A $\beta$  aggregates in AD brain slices (Fig. 20(b)). A $\beta$  aggregates in brain slices exhibited blue fluorescence, while A $\beta$  aggregates in brain slices treated with ONOO<sup>−</sup> exhibited green fluorescence. In general, 3-HF could accurately image A $\beta$  aggregates in AD

brain using two fluorescence channels in the absence/presence of ONOO<sup>−</sup>. Recently, Wang *et al.* reported a novel two-photon fluorescent probe (BTNPO) that could monitor the distribution and changes of A $\beta$  aggregates and ONOO<sup>−</sup> through two independent fluorescence channels (Fig. 21).<sup>206</sup> BTNPO consisted of two parts: (i) the benzothiazole-naphthalene derivative BTNPO was selected as the recognition group for A $\beta$  aggregates due the structural similarity with thioflavin T; (ii) oxindole was selected as a recognition group for ONOO<sup>−</sup> (Fig. 21(a)). In the presence of A $\beta$  aggregates/ONOO<sup>−</sup>, BTNPO produced significant fluorescence enhancement at 418 nm/506 nm (Fig. 21(a)). When the two analytes coexisted, the two reactions did not interfere with each other. As such using this probe, A $\beta$  aggregate-induced ONOO<sup>−</sup> formation in neurons could be visualized and confirmed that ONOO<sup>−</sup> levels were positively correlated with the co-incubation time and concentration of A $\beta$  aggregates (Fig. 21(b)). Furthermore, by co-imaging the dynamics of A $\beta$  aggregates and ONOO<sup>−</sup> levels in brain slices at different ages (months), it was found that high levels of ONOO<sup>−</sup> were generated earlier than A $\beta$  aggregates in AD mouse brains (Fig. 21(c)).

As an important signaling molecule and oxidant, H<sub>2</sub>O<sub>2</sub> has been closely associated with the pathology of Alzheimer's disease. Ran *et al.* reported a cascade signal amplification fluorescent probe (CRANAD-88) that could be used to detect H<sub>2</sub>O<sub>2</sub> and A $\beta$  aggregates in the brain of AD mice.<sup>207</sup> CRANAD-88 consisted of two parts: (i) an analog of curcumin-58 (A $\beta$  aggregates recognition group) was used as the main fluorophore; (ii) benzyl boronic ester was used as the recognition

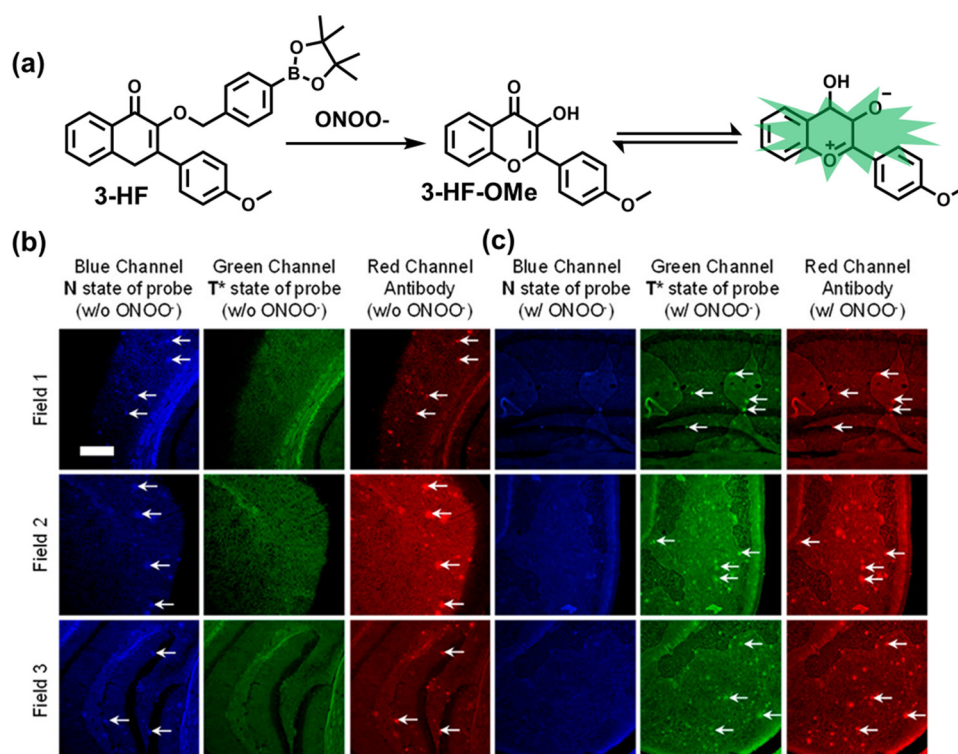


Fig. 20 (a) Structure of 3-HF and reaction with ONOO<sup>−</sup>. (b) Fluorescence imaging of a brain section of a transgenic mouse treated with 3-HF (20  $\mu$ M) without (w/o) (b) and with (w/) (c) ONOO<sup>−</sup> (30  $\mu$ M). Reproduced with permission from ref. 205. Copyright (2018) American Chemical Society.



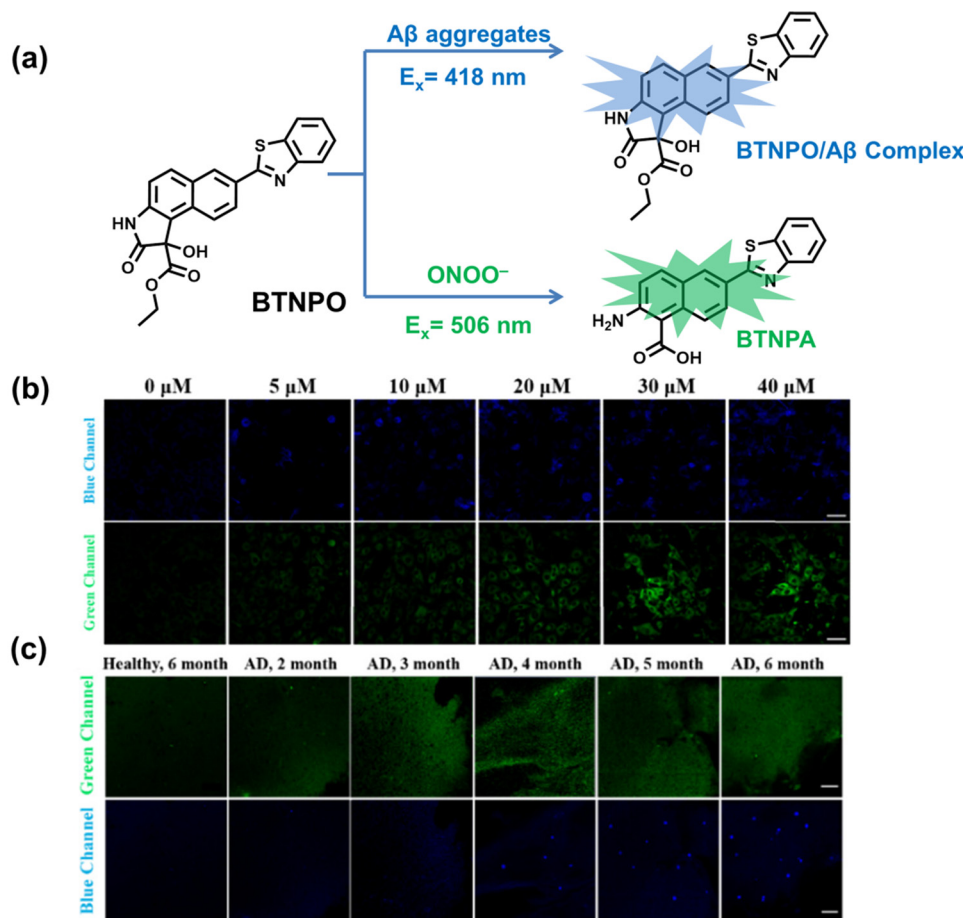


Fig. 21 (a) Dual-Color fluorescence responses of BTNPO to A $\beta$  aggregates and ONOO<sup>-</sup>. (b) PC12 cells were treated with A $\beta$  aggregates (0, 5, 10, 20, 30, or 40  $\mu$ M) for 12 h and then incubated with 10  $\mu$ M BTNPO for 30 min. (c) Representative two-photon images of ONOO<sup>-</sup> and A $\beta$  aggregates in brain tissues of AD mouse. Reproduced with permission from ref. 206. Copyright (2021) American Chemical Society.

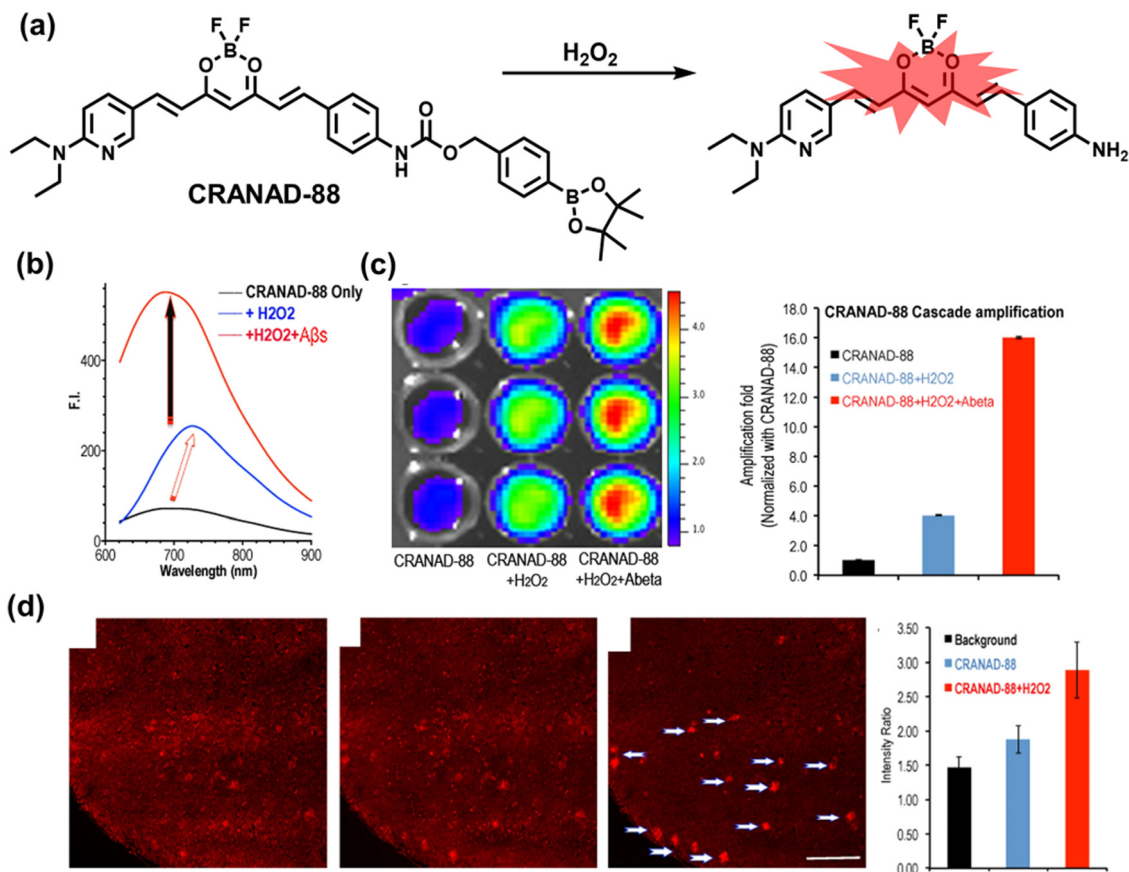
group for H<sub>2</sub>O<sub>2</sub> (Fig. 22(a)). The two parts were combined using a carbamate linkage. Due to the electron withdrawing effect of the carbamate, the excitation/emission wavelength of curcumin-58 underwent a hypsochromic shift and part of the fluorescence was quenched. In the presence of H<sub>2</sub>O<sub>2</sub>, CRANAD-88 exhibited a bathochromic shift of fluorescence excitation/emission and a 4-fold increase in fluorescence intensity. The reaction product associated with A $\beta$  aggregates achieved a 16-fold increase in fluorescence intensity (Fig. 22(b)). This probe was then used for the *in vitro* microscopic imaging of AD mouse brain slices, and the signal with A $\beta$  plaques and H<sub>2</sub>O<sub>2</sub> was increased by about 2 times (Fig. 22(c)). Based on *in vivo* imaging experiments, CRANAD-88 successfully crossed the blood-brain barrier and exhibited stronger fluorescent signals in AD mouse brains. This was the first time that fluorescent probes were used to detect H<sub>2</sub>O<sub>2</sub> in AD mouse brains.

The mitochondrial respiratory chain is the main pathway for the generation of ROS, and mitochondrial dysfunction induced by oxidative stress is an important factor in the pathogenesis of AD.<sup>208,209</sup> Liu *et al.* designed a NIR fluorescent probe (Mito-NIRHV) (Fig. 23(a)), which was used to detect mitochondrial viscosity and H<sub>2</sub>O<sub>2</sub> in the brain of AD mice.<sup>210</sup> In the presence

of H<sub>2</sub>O<sub>2</sub>, Mito-NIRHV exhibited a strong absorption peak at 440 nm, and the fluorescence signal at 700 nm was significantly enhanced. In addition, an increase of environmental viscosity enhanced the maximum absorption peak at 570 nm, and the fluorescence signal at 800 nm increased significantly. Mito-NIRHV exhibited low cytotoxicity, mitochondrial targeting (Pearson coefficient of 0.968) and a suitable lipid-water partition coefficient ( $\log P = 1.57$ ). Importantly, the fluorescence signal of Mito-NIRHV in an AD brain was stronger than that of healthy mice for both the 700 nm and 800 nm fluorescence channels. The results indicated that H<sub>2</sub>O<sub>2</sub> levels and mitochondrial viscosity increased in AD brains.

There has been a lack of comprehensive biological evidence linking AD with oxidative stress. Ran *et al.* designed a NIR fluorescent probe (CRANAD-61) based on oxalate-curcumin, which could be used for macroscopic and microscopic detection of ROS levels in the brain of AD.<sup>211</sup> CRANAD-61 was composed of two parts: (i) curcumin was selected as the host fluorophore; (ii) oxalate borate as a ROS recognition group which shifted the excitation and emission wavelength into the NIR region ( $\lambda_{\text{ex}}/\lambda_{\text{em}} = 675/810$  nm) (Fig. 23(b)). An appropriate lipid-water partition coefficient ( $\log P = 2.4$ ) enabled





**Fig. 22** (a) Structures of CRANAD-88 and reaction with  $H_2O_2$ . (b) Fluorescence intensity changes of CRANAD-88 with  $H_2O_2$  and with  $H_2O_2$  + Aβ aggregates. (c) Cascade signal amplification validation of CRANAD-88 on a plate and quantitative analysis of the image. (d)  $H_2O_2$ -treated/untreated brain sections were evaluated for staining using CRANAD-88 and quantification histograms. Reproduced with permission from ref. 207. Copyright (2016) Springer Nature.

CRANAD-61 to efficiently pass through the BBB. In the presence of ROS, the cleavage of the oxalic acid caused a blue shift in the excitation and emission wavelengths ( $\lambda_{ex}/\lambda_{em}$  = 500/570 nm) (Fig. 23(c)). In addition, active Aβ plaques produce a large amount of ROS during the growth process, which is expected to have stronger neurotoxicity than silent Aβ plaques.<sup>212</sup> At the microscopic level, using CRANAD-61 and fluorostyrylbenzene (FSB, commercial Aβ plaque marker dye), the distinction between the two types of plaques and the local concentration of ROS around Aβ plaques could be evaluated. The areas with higher conversion efficiency were active Aβ plaques with higher ROS concentrations, while areas with bright red fluorescence and extremely low conversion rate were silent Aβ plaques (Fig. 23(d)). At the macroscopic level, the brain fluorescence intensity of AD mice was significantly lower than that of healthy mice at 30, 60, 120, and 240 minutes (Fig. 23(e)). This study provides important biological evidence for the relationship between Alzheimer's disease and oxidative stress.

## 5.2 Parkinson's disease

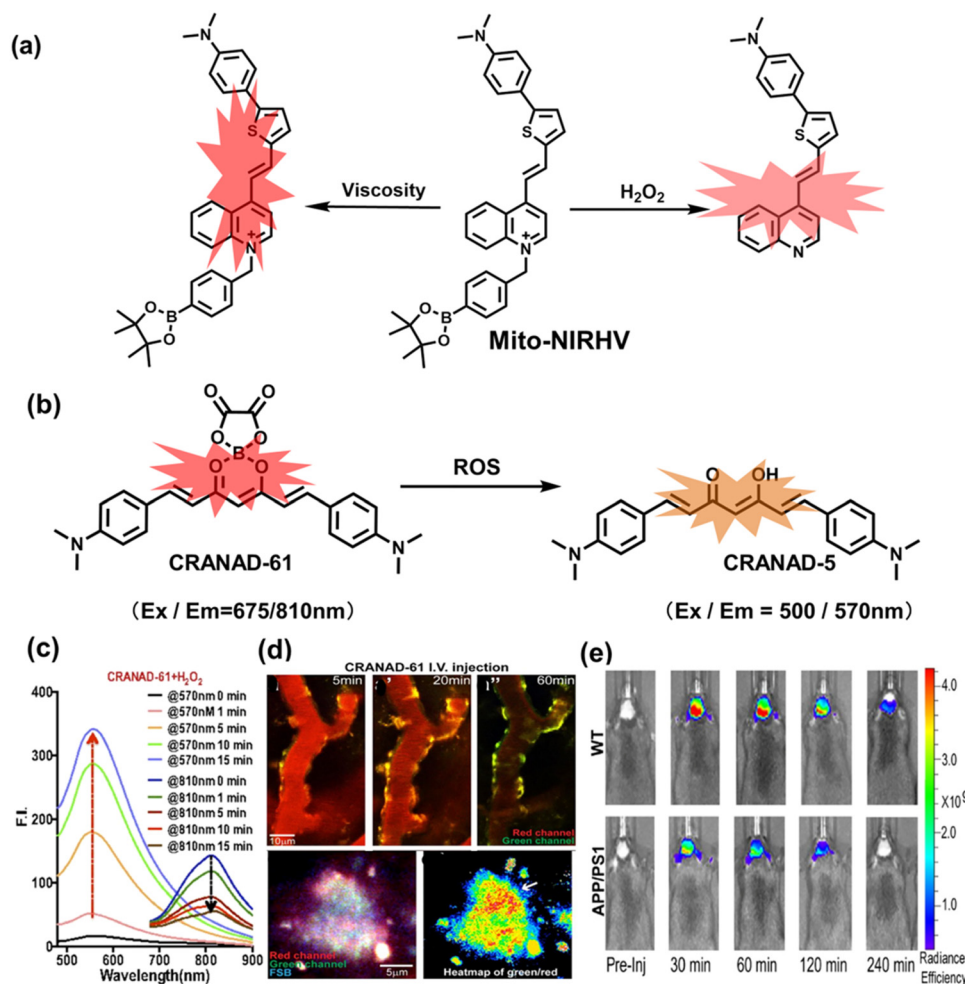
Parkinson's disease (PD) is the second largest neurodegenerative disease, threatening the lives of millions of people worldwide. There are still a lack of effective therapeutic drugs and early

diagnostic methods available for clinical practice.<sup>213</sup> The loss of dopaminergic neurons in the substantia nigra (SN) area is the main histopathological feature of PD.<sup>214</sup> The imbalance of redox homeostasis in neuronal cells often leads to the destruction of normal physiological processes and ultimately leads to cell apoptosis. To date, significant evidence for oxidative damage to numerous key cell components of PD patients has been accumulated (Such as protein, lipid, DNA and RNA oxidation and lower levels of reduced glutathione).<sup>215–220</sup> In addition, a variety of toxins that can cause oxidative stress induce the recurrence of the important features of PD in laboratory animals.<sup>221,222</sup> This evidence indicates that oxidative stress plays an important role in the degradation of dopaminergic neurons in PD. However, there is still a lack of methods that can detect oxidative stress in the brain of PD patients in real time, whether for clinical testing or the evaluation of drug efficacy. As such, the development of suitable fluorescent probes will provide appropriate methods to help improve the prognosis of PD patients.

Mitochondrial dysfunction and oxidative stress play a vital role in the pathogenesis of PD, and the mitochondrial micro-environment and  $H_2O_2$  levels are two key parameters for evaluating mitochondrial function.<sup>223</sup> Yu *et al.* designed a two-photon (TP) fluorescent probe (Mito-LX), which could







**Fig. 23** (a) Structure of Mito-NIRHV and sensing mechanism for the discrimination of H<sub>2</sub>O<sub>2</sub> and viscosity. (b) Structure of CRANAD-61 and sensing mechanism for the discrimination of ROS. (c) The fluorescence intensity at 570 nm and 810 nm of CRANAD-61 co-incubated with H<sub>2</sub>O<sub>2</sub> at different time points. (d) CRANAD-61 was used for the fluorescence imaging of brain CAA (amyloid cerebrovascular disease) and amyloid plaques in AD mice. (e) CRANAD-61 was used for real-time imaging of AD mice and healthy mice at 30, 60, 120, and 240 min. Reproduced with permission from ref. 211. Copyright (2017) Published by National Academy of Sciences.

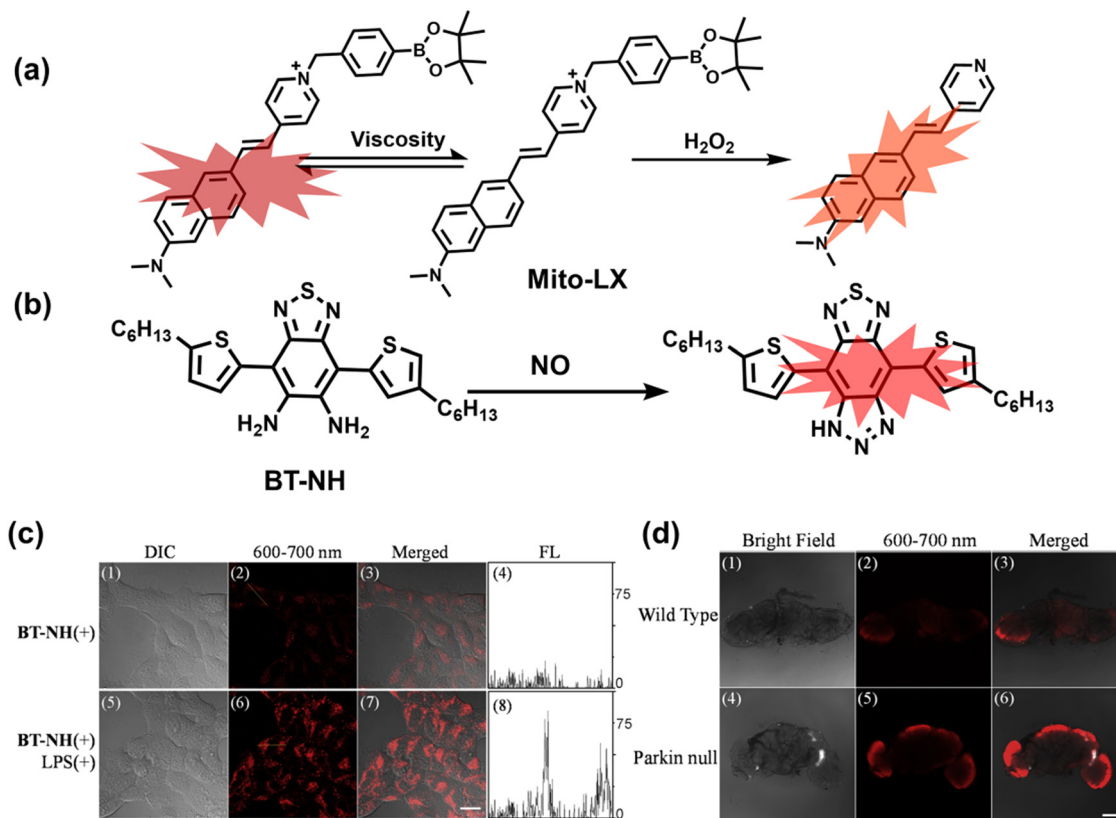
simultaneously monitor the dynamic changes of mitochondrial viscosity and H<sub>2</sub>O<sub>2</sub> levels in the brain of PD animals.<sup>224</sup> Mito-LX was composed of four parts: (i) *N,N*-dimethylamino as electron donor; (ii) pyridine salt cation as electron acceptor; (iii) naphthalene ring with extended conjugated structure; (iv) benzyl boronic ester as H<sub>2</sub>O<sub>2</sub> recognition group (Fig. 24(a)). In the presence of H<sub>2</sub>O<sub>2</sub>, the cleavage of the benzyl boronic ester results in a significant increase in fluorescence intensity at 585 nm. In addition, with Mito-LX the fluorescence intensity at 730 nm increases as the viscosity (0.60–945 cp) increased. Moreover, by incubating Mito-LX with wild-type drosophila and PD drosophila respectively, the PD Drosophila brain exhibited a >2-fold enhanced fluorescence signal at 585 nm and a 1.5-fold enhanced fluorescence signal at 730 nm. The H<sub>2</sub>O<sub>2</sub> levels and mitochondrial viscosity in PD brains were significantly higher than those for normal brains.

Abnormally high levels of nitric oxide can react with reactive oxygen to generate a variety of reactive nitrogen species to induce oxidative stress in organisms. To achieve specific and

highly sensitive detection of NO in the brain of PD animal models, Huang *et al.* designed and synthesized a fluorescent probe (BT-NH) (Fig. 24(b)).<sup>225</sup> The structural design was derived from diamino fluorescein and benzobis (1,2,5-thiadiazole). The two ortho amino groups on the benzene ring can react with NO to increase the fluorescence intensity and generate an emission wavelength red shift (20 nm). Importantly, BT-NH had an extremely low detection limit (LOD = 6.96 nM), high selectivity for NO and exhibited pH insensitivity. To further evaluate the ability to detect NO, BN-TH was used to image endogenous NO in HepG2 cells (Fig. 24(c)) and PD Drosophila brains (Fig. 24(d)), respectively. The cells (LPS stimulated) and PD Drosophila brains all exhibited stronger fluorescence signals than the control groups, indicating that PD and inflammatory conditions can cause an abnormal increase in the NO levels. In addition, Huang *et al.* developed a ratiometric near-infrared fluorescent probe NIR-HP1 for exploring the dynamic changes of H<sub>2</sub>O<sub>2</sub> flux in a PD model.<sup>226</sup> NIR molecule 1 with ESIPT fluorescence mechanism was selected as the fluorophore, and







**Fig. 24** (a) Structures of Mito-LX and sensing mechanism for discrimination of  $\text{H}_2\text{O}_2$  and viscosity. (b) Structures of BT-NH and sensing mechanism for the discrimination of NO. (c) Confocal fluorescence imaging of exogenous NO levels in living SH-SY5Y cells using BT-NH. (d) Fluorescence imaging of endogenous NO levels in drosophila brain tissues using BT-NH. Reproduced with permission from ref. 225. Copyright (2019) Elsevier B.V.

benzyl boronic ester was used as the recognition site for  $\text{H}_2\text{O}_2$  (Fig. 25(a)). NIR-HP1 exhibited significant ratiometric selectivity towards  $\text{H}_2\text{O}_2$ , and the ratio of fluorescence intensity at 650 and 500 nm ( $F_{650}/F_{500}$ ) increased linearly with an increase in  $\text{H}_2\text{O}_2$  concentrations. *In vitro* and *in vivo* experiments indicated that NIR-HP1 could accurately detect endogenous  $\text{H}_2\text{O}_2$  in cells and zebrafish. Moreover, a higher fluorescence ratio in PD Drosophila brains was observed indicating high levels of  $\text{H}_2\text{O}_2$ .

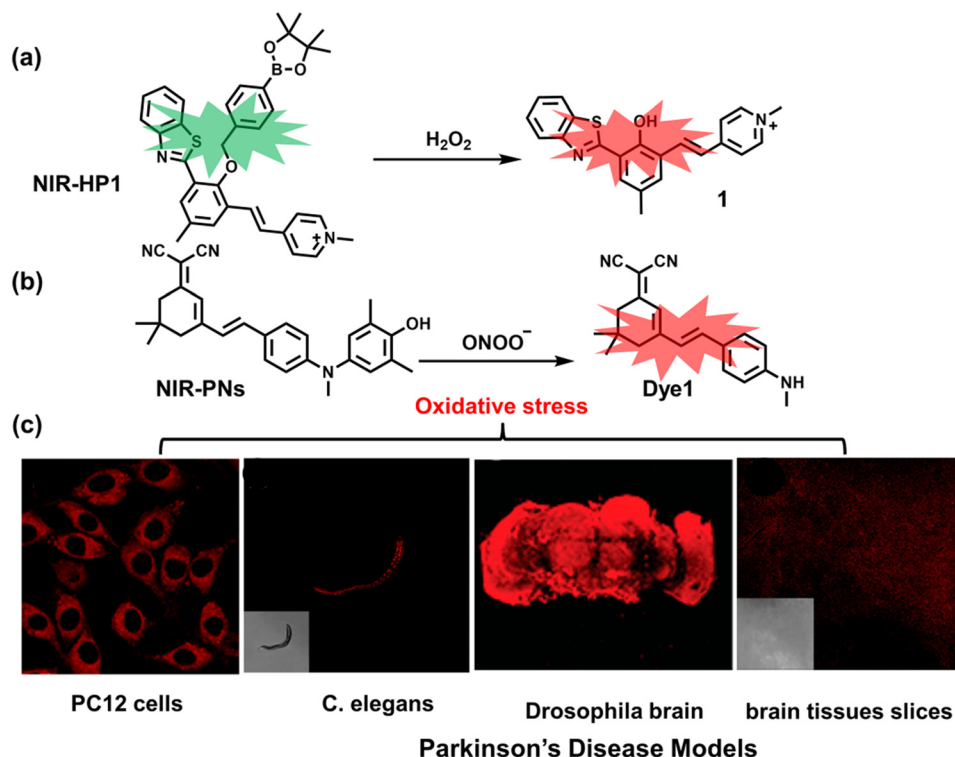
The overproduction of  $\text{ONOO}^-$  is considered to be a key neurotoxic factor and potential biomarker of oxidative stress in the brain of PD patients.<sup>227</sup> Liu *et al.* developed a series of near-infrared probes (NIR-PNs), which could be used for the ultra-fast (within a few seconds) and highly selective detection of  $\text{ONOO}^-$  in a variety of PD animal models.<sup>228</sup> A dicyanoisophorone with a donor (D)- $\pi$ -acceptor(A) structure was selected as the host fluorophore, and methoxy-substituted *p*-aminophenol was used as the specific reaction site for  $\text{ONOO}^-$  (Fig. 25(b)). In the presence of  $\text{ONOO}^-$ , the *p*-aminophenol group can undergo a cleavage reaction to release *p*-benzoquinone. The disappearance of the PET effect results in rapid recovery of the fluorescence signal ( $\lambda_{\text{ex}}/\lambda_{\text{em}} = 520/670 \text{ nm}$ ). Cell imaging indicated that NIR-PNs could detect dynamic changes of endogenous  $\text{ONOO}^-$ , with a 5.86-fold increase in fluorescence intensity. Moreover, NIR-PNs exhibited 4–7 fold fluorescence increase in various PD animal models and

tissues (including parkin null drosophila, mice brain slices, and WLZ3 *C. elegans*) (Fig. 25(c)).

### 5.3 Epilepsy

Epilepsy is one of the most serious neurological diseases of the brain, and nearly 50 million people in the world suffer from this disease. Epilepsy is divided into three types according to the cause, namely idiopathic, induced, or symptomatic epilepsy. Symptomatic epilepsy is caused by disease or trauma; induced epilepsy is caused by drug stimulation or external environmental stimulation; and idiopathic epilepsy is linked to genetic factors.<sup>229</sup> In addition, patients with epilepsy associated with these causes often have no neuroanatomical or neuropathological abnormalities.<sup>230,231</sup> A significant amount of evidence indicates that the pathogenesis of epilepsy is closely related to oxidative stress.<sup>232</sup> It has been reported that drug-induced epilepsy rats brain lipid and DNA exhibit significant oxidative damage, and blood antioxidants (such as cysteine, glutathione) levels are reduced.<sup>233–237</sup> Compared with wild-type mice, transgenic mice lacking superoxide dismutase exhibited an increased incidence of spontaneous and handling-induced seizures.<sup>238</sup> As such the development of fluorescent probes facilitating the early diagnosis of epilepsy will provide useful tools for understanding the pathological mechanisms linking epilepsy with oxidative stress.





**Fig. 25** (a) Structures of NIR-HP1 and sensing mechanism for determination of  $\text{H}_2\text{O}_2$ . (b) Fluorescence turn 'on' mechanism of NIR-PNs in the presence of  $\text{ONOO}^-$ . (c) NIR-PNs was used for the detection of  $\text{ONOO}^-$  in PC12 cells and different PD models. Reproduced with permission from ref. 228. Copyright (2020) American Chemical Society.

Myeloperoxidase is believed to play an important role in the pathological dysfunction of the epileptic brain.<sup>239</sup> Qian *et al.* developed an efficient two-photon fluorescent probe (HCP), which could be used to detect endogenous  $\text{HClO}$  generated by myeloperoxidase (MPO) in the brain of epileptic mice.<sup>240</sup> The quinoline skeleton was used as the host fluorophore and recognition site (Fig. 26(a)). The chlorination reaction with  $\text{HClO}$  resulted in a 100 nm blue-shifted emission wavelength and a 138-fold increase in fluorescence intensity. In addition, HCP also exhibited effective BBB permeability, high photostability, and excellent two-photon excitation characteristics. Through tail vein injection of HCP, enhanced fluorescence in the brain of epileptic mice could be directly observed, indicating that MPO-mediated oxidative stress was positively correlated with severe neuronal damage and epilepsy (Fig. 26(c and d)). Significantly, HCP was used to construct a simple high-throughput screening method to quickly screen potential anti-epileptic drugs (Fig. 26(b)). It was observed that the flavonoid compound apigenin can relieve MPO-mediated oxidative stress and inhibit neuronal cell hypertrophy (ferroptosis). This work not only provided a powerful fluorescent tool for understanding the pathological mechanism between hypochlorous acid-induced oxidative stress and epilepsy, but also elucidated a general strategy for screening anti-epileptic drugs.

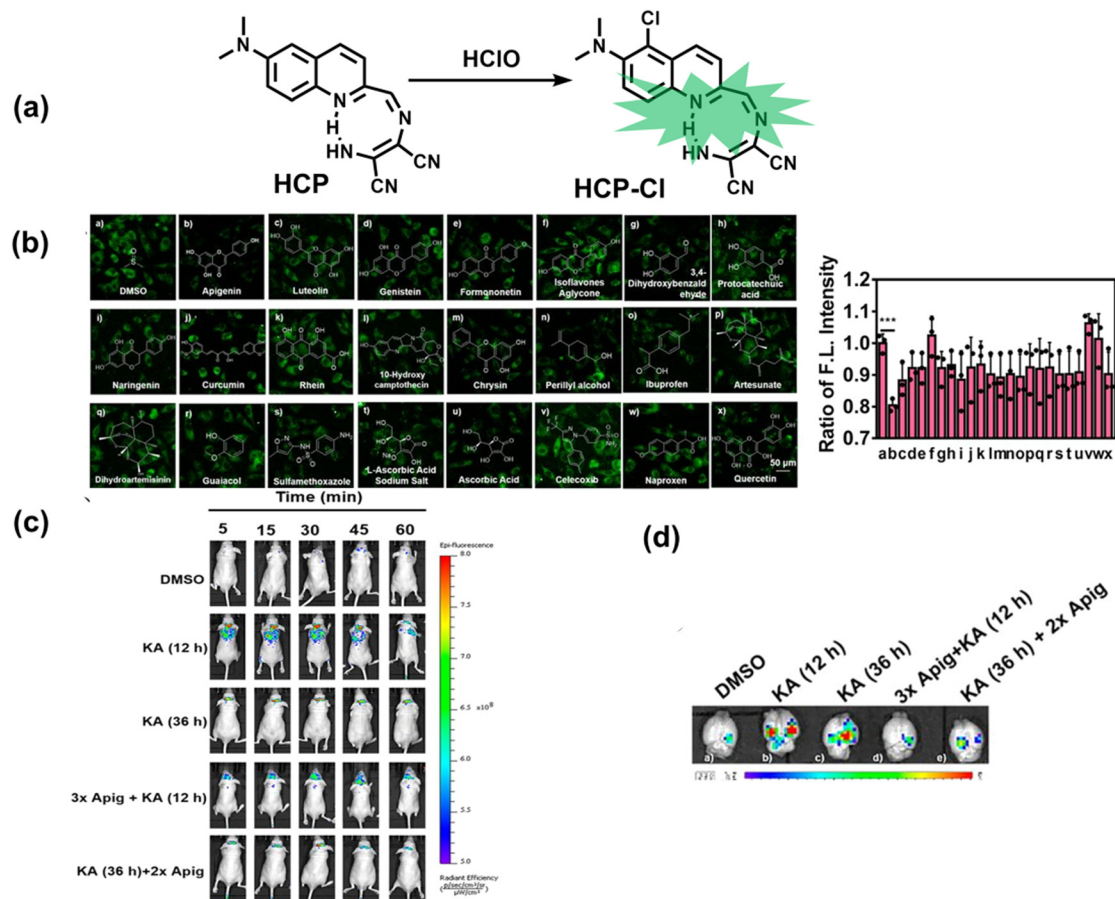
Abnormally high levels of  $\text{ONOO}^-$  are considered to be a key neurotoxic factor and may serve as a potential biomarker for the early diagnosis of epilepsy and evaluation of drug efficacy.<sup>241,242</sup> In order to monitor dynamic changes of the  $\text{ONOO}^-$  signal in the brain of epileptic rats in real time, Yu *et al.* developed a two-

photon fluorescent probe (DCM- $\text{ONOO}$ ) based on the DCM fluorophore and the  $\text{ONOO}^-$  specific diphenylphosphonamide (Fig. 27(a)).<sup>243</sup> Spectroscopic analyses indicated that DCM- $\text{ONOO}$  exhibited high sensitivity, specificity, and rapid response. Combined with TP fluorescence imaging, the fluorescence intensity of DCM- $\text{ONOO}$  in the brain of epileptic rats was significantly higher than that of healthy rats and epileptic rats treated using resveratrol. In addition, the brain tissue slices of the epileptic rats exhibited higher fluorescence intensity and a large amount of neuron loss, which confirmed that overexpression of  $\text{ONOO}^-$  was positively correlated with seizures and neuronal damage.

To design potential screening tools for anti-epileptic drugs, Qian *et al.* designed an  $\text{ONOO}^-$  responsive fluorescent probe (ONP) based on methylene blue and benzyl boronic ester group (Fig. 27(b)).<sup>244</sup> ONP displays effective BBB permeability, extremely low cytotoxicity, and excellent temporal and spatial resolution. Using ONP, the dynamic changes of endogenous  $\text{ONOO}^-$  flux in the epileptic brain of mice could be quickly and sensitively monitored. *In vitro* and *in vivo* imaging of the hippocampus of epileptic mice indicated that higher concentrations of  $\text{ONOO}^-$  were positively correlated with severe neuronal damage and epilepsy. In addition, a high-throughput screening method for anti-epileptic inhibitors was constructed by combining high-content analysis (HCA) and ONP. In addition it was found that curcumin could effectively inhibit the overexpression of  $\text{ONOO}^-$  in the brains of epileptic mice.

Cysteine (Cys) is an important free radical scavenger in organisms and plays an important role in regulating redox





**Fig. 26** (a) Fluorescence turn 'on' mechanism of HCP in the presence of HClO. (b) HCP was used for the high-throughput screening of natural products in live H-SY5Y human neuroblastoma cells to control MPO-mediated oxidative stress. (c) HCP was used to detect hypochlorous acid in the brain of epileptic mice (kainic acid (KA)-induced epileptic seizure) and evaluate the therapeutic effect of apigenin. Reproduced with permission from ref. 240. Copyright (2020) Published by National Academy of Sciences.

homeostasis. Liu *et al.* designed probe (Mito-CP) that could be used to monitor the dynamic changes of endogenous cysteine levels in the brain of mice with epilepsy.<sup>245</sup> Mito-Q with near-infrared emission was selected as the host fluorophore, and acrylate was used as the recognition site for Cys (Fig. 27(c)). In addition, Mito-CP exhibited effective BBB permeability, mitochondrial targeting, and a large Stokes shift of approximately 260 nm. Using Mito-CP, Cys could be detected without interference from other thiols in PC12 cells and zebrafish (Fig. 27(d)). Importantly, changes in the dynamic flux of Cys in an epileptic brain was observed for the first time (Fig. 27(e and f)). This research confirmed that curcumin was beneficial for the recovery of Cys levels in epileptic brains.

#### 5.4 Depression

Depression is a common mental illness. Significant and lasting depression is the main clinical feature. The manifestations of depressive episodes can be divided into core symptoms, psychological symptoms, and somatic symptoms.<sup>246</sup> A depressed mood, slow thinking, and decreased volitional activity are typical symptoms of major depression.<sup>246</sup> Global estimates indicated that there are approximately 322 million patients

with depression in the world, with a prevalence rate of 4.4%.<sup>247</sup> As such this disease has undoubtedly become one of the serious health problems that plague the world. However, there is still a lack of effective means for the rapid diagnosis of depression in clinical practice.<sup>248,249</sup> Compared to other chronic diseases caused by a variety of pathological factors, the pathophysiology of depression is still in its infancy.<sup>250,251</sup> In recent years, a large amount of evidence has shown that oxidative stress is closely related to the pathological process of depression.<sup>252</sup> It has been found that the levels of peroxides and xanthine oxidase in the plasma of patients with depression is enhanced, while the plasma concentrations of many key antioxidants are significantly reduced (*e.g.*, vitamin E, glutathione, zinc and coenzyme Q10).<sup>253–257</sup> In addition, some key cellular components in the brain of depression (*e.g.*, protein, fatty acid, DNA) exhibit varying degrees of oxidative damage.<sup>258–260</sup> Although oxidative stress has attracted more and more attention in the investigation of the pathology of depression, there is still a lack of clinical tools that can be used for real-time imaging of RONSS in the brain of patients with depression. Recently, due to the excellent temporal and spatial resolution of fluorescence imaging technology, researchers have begun to use fluorescent probes for imaging





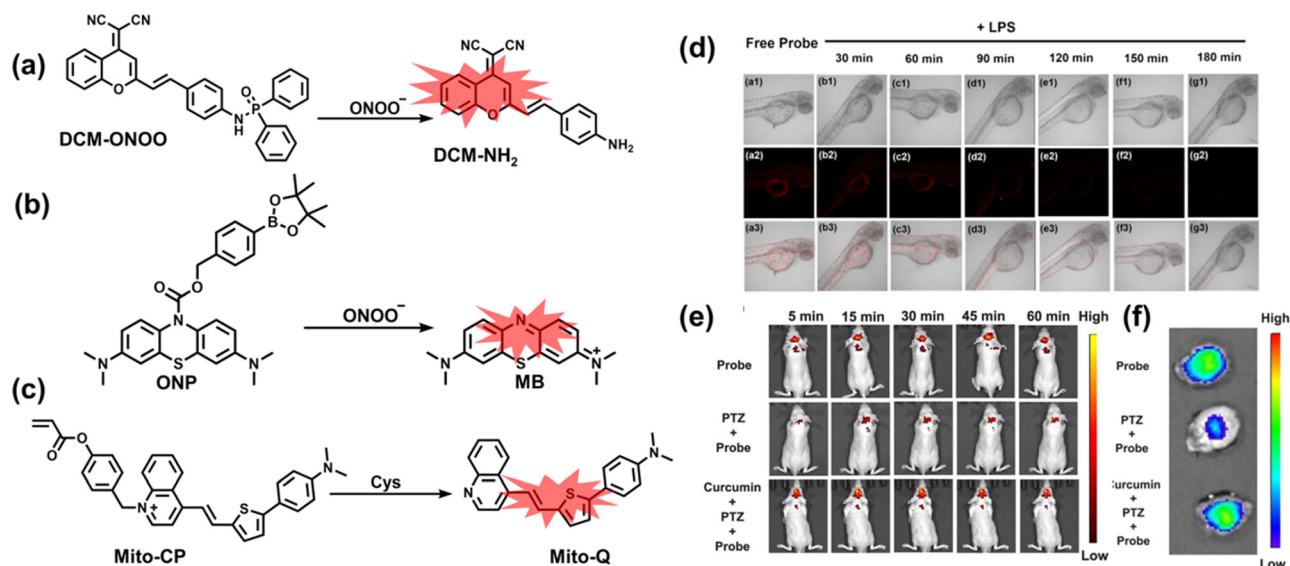


Fig. 27 (a) Fluorescence turn 'on' mechanism of DCM-ONOO in the presence of  $\text{ONOO}^-$ . (b) Fluorescence turn 'on' mechanism of ONP in the presence of  $\text{ONOO}^-$ . (c) Fluorescence turn 'on' mechanism of Mito-CP in the presence of Cys. (d) Fluorescence images of Mito-CP responding to Cys in living zebrafish under oxidative stress (e) Mito-CP was used to image Cys in the brains of mice in epilepsy/treatment group. (f) Fluorescence imaging of dissected epilepsy/treated mouse brains. Reproduced with permission from ref. 245. Copyright (2020) American Chemical Society.

oxidative stress in the brains of patients suffering from depression.

As one of the reactive oxygen species with high reactivity and strong oxidizing properties, the accurate detection of  $\cdot\text{OH}$  in the brain has always been a challenge. Li *et al.* developed a two-photon fluorescent probe (MD-B), which could be used for the imaging of  $\cdot\text{OH}$  in the brains of depressed mice.<sup>261</sup> Coumarin with excellent two-photon properties was selected as the host fluorophore, 3-methylpyrazolone was used as the specific

recognition site and electron donor group for  $\cdot\text{OH}$  (Fig. 28(a and b)). The introduction of the strong electron withdrawing group trifluoromethyl increased the push-pull electron effect of the conjugated system. MD-B exhibited rapid response, good BBB permeability and high sensitivity (detection limit was 2.4 nM). Using MD-B, dynamic changes of  $\cdot\text{OH}$  in cells and the brains of mice with depression were imaged, and it was found that an increase of  $\cdot\text{OH}$  flux in the brain was positively correlated with the severity of the depression phenotype

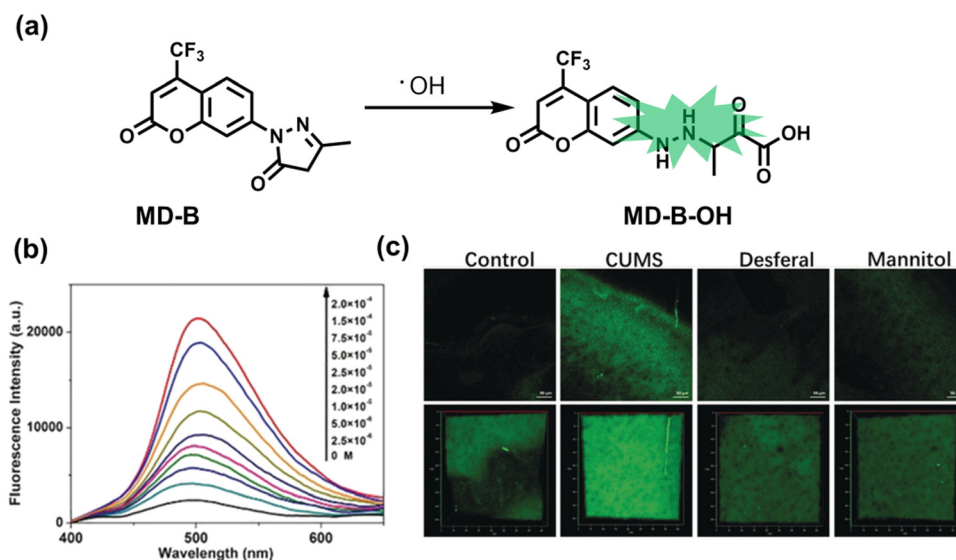


Fig. 28 (a) Fluorescence turn 'on' mechanism of MD-B in the presence of  $\cdot\text{OH}$ . (b) The fluorescence emission spectrum of MD-B changes with the addition of different concentrations of  $\cdot\text{OH}$  (2.5–200  $\mu\text{M}$ ). (c) Two-photon fluorescence imaging of MD-B using a mouse cranial window. CUMS (Chronic unpredictable mild stress): mice exhibit depression-like behavior. Desferal: The susceptible mice injected desferrioxamine (iron scavenger). Mannitol: The susceptible mice injected with mannitol ( $\cdot\text{OH}$  scavenger). Reproduced with permission from ref. 261. Copyright (2019) Wiley-VCH Verlag GmbH & Co. KGaA, Weinheim.





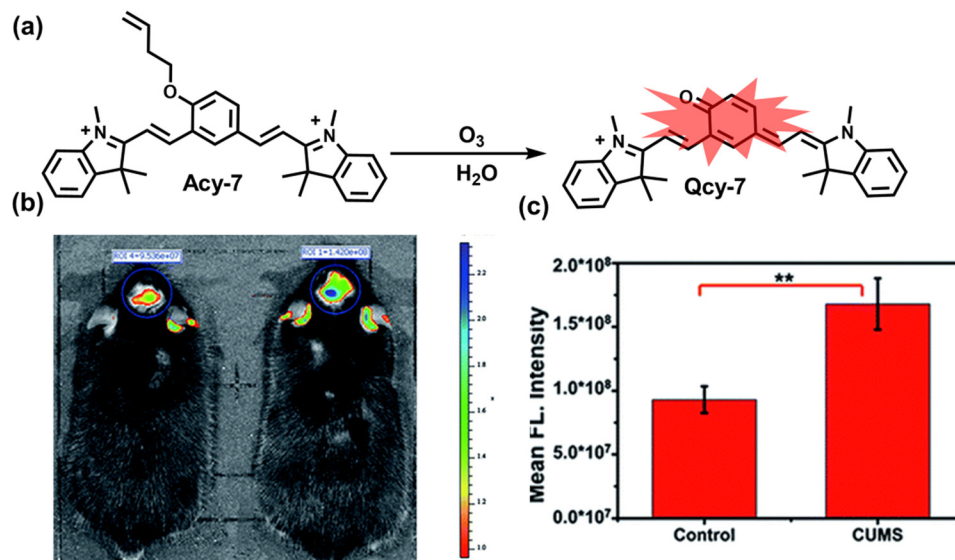


Fig. 29 (a) Fluorescence turn 'on' mechanism of Acy-7 in the presence of  $O_3$ . (b) Fluorescence imaging of  $O_3$  in the brains of depression mice. (c) Quantification of images in (b). Reproduced with permission from ref. 264. Copyright (2019) The Royal Society of Chemistry.

(Fig. 28(c)). In addition, MD-B was used to demonstrate that the strong oxidizing properties of  $\cdot OH$  could inactivate the deacetylase SIRT1, resulting in the development of the depressive phenotype.

As a reactive oxygen species, ozone is believed to be closely related to the pathogenesis of many mental diseases including depression.<sup>262,263</sup> Tang *et al.* designed and synthesized a cyanine dye-based probe (Acy-7) that can be used to visualize  $O_3$  in the brains of depressed mice.<sup>264</sup> Acy-7 was constructed using a Cy7 fluorophore locked using a 3-butenyl group recognition group (Fig. 29(a)). Acy-7 exhibited good sensitivity (detection limit of 10 nM) and selectivity for  $O_3$ . This study successfully visualized the overproduction of  $O_3$  in PC12 cells and macrophages under oxidative stress. Importantly, Acy-7 was used to monitor the increase in  $O_3$  in the brains of mice with depression for the first time (Fig. 29(b and c)). In addition, fluorescence imaging combined with enzyme-linked immunosorbent assay (ELISA) successfully confirmed that the overproduction of  $O_3$  in the mouse brain could promote the production of pro-inflammatory cytokine interleukin-8 (IL-8), which is one of the important factors leading to depression in mice.

As key antioxidants in the body against oxidative stress, thiols are closely related to the pathological process of depression. Li *et al.* designed and synthesized a two-photon fluorescent probe (ER-SH), which could be used to detect a variety of thiols in the brains of depressed mice.<sup>265</sup> ER-SH was composed of three parts: (i) 1,8-naphthalene dimethylamine with good two-photon performance was selected as the fluorophore; (ii) 2,4-dinitrobenzene sulfonamide (DNBS) was used as the thiol specific recognition site; (iii) toluene sulfonamide served as the targeting group of the Golgi apparatus (Fig. 30(a)). ER-SH exhibited excellent sensitivity to three common thiols (Cys, GSH and Hcy), and was not affected by other biological species (including ROS, RNS and metal ions). This study successfully visualized endogenous thiols in the endoplasmic

reticulum of PC12 cells and endogenous thiols in the brains of depressed mice. Meanwhile, it was found that the fluorescence signal of the brains of depressed mice was 2.6 times lower than normal mice.

In addition, to accurately detect changes in the levels of a single thiol in a brain of model, Tang *et al.* recently reported a two-photon fluorescent probe (TCS) with high specificity for cysteine in the brain of depressed mice.<sup>266</sup> Coumarin 120, which has excellent two-photon properties, was selected as the fluorophore. The thiobenzoate was used as a specific recognition site for cysteine (Fig. 30(b)). In the presence of Cys, a stable five-membered ring is formed through a selective nucleophilic addition reaction, thereby triggering a significant fluorescence enhancement. TCS exhibited effective BBB permeability, superior sensitivity, and biocompatibility. Importantly, TCS was used to directly observe the dynamic changes of Cys in the brains of depressed mice, and successfully revealed a negative correlation between Cys levels and the degree of depressive behavior. However, the emission wavelengths of ER-SH and TCS cannot reach the near-infrared region, which limited their application for *in vivo* imaging.

## 5.5 Diabetes

Diabetes is a metabolic disease characterized by hyperglycemia and insufficient endogenous insulin secretion or action.<sup>267</sup> Defective or impaired insulin secretion can lead to elevated blood sugar levels in the body, while long-term hyperglycemia can induce complications including heart disease, stroke, vascular disease, and kidney disease.<sup>268</sup> In particular, oxidative stress induced by hyperglycemia is thought to play an important role in the development of diabetic complications.<sup>269</sup> Abnormally high levels of radicals can cause severe oxidative damage to a variety of biological components in cells, and ultimately lead to damage of cell function or death. Glucose oxidation is



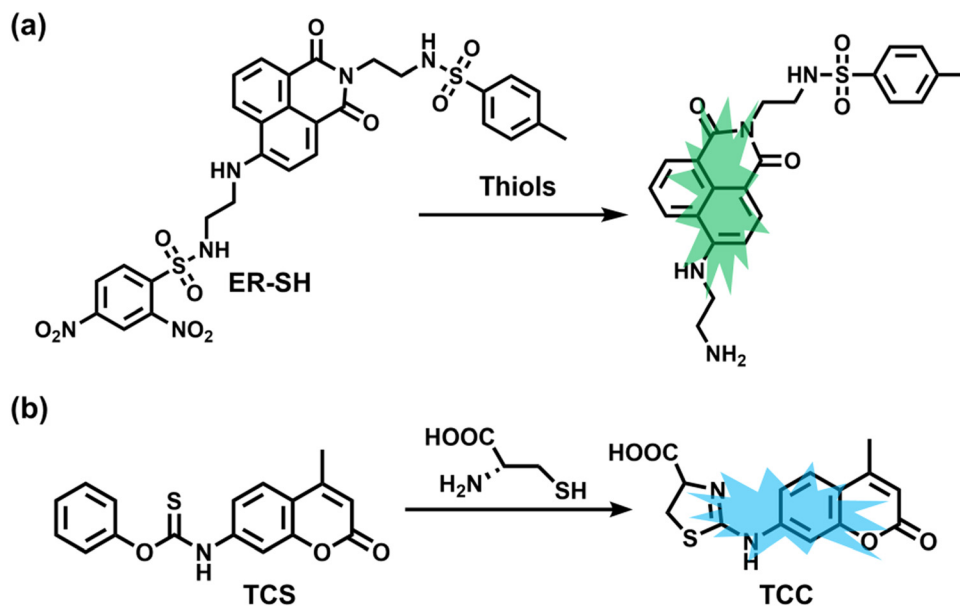


Fig. 30 (a) Fluorescence turn 'on' mechanism of ER-SH in the presence of thiols. (b) Fluorescence turn 'on' mechanism of TCS in the presence of Cys.

one of the main sources of radicals. The enediol radical anion is the main product of the glucose oxidation reaction, and this anion is rapidly converted into reactive ketoaldehydes and superoxide anion radicals due to its unstable structure.<sup>270</sup> The radical is inherently highly oxidizing and easily decomposes to produce hydrogen peroxide or reacts with NO to produce peroxynitrite (ONOO<sup>−</sup>). In addition, by measuring the levels of oxidative stress markers in body fluids of patients and rodent disease models, it was found that lipids, proteins, enzymes, and DNA all exhibit varying degrees of oxidative damage, while the reductant levels of glutathione,  $\alpha$ -lipoic acid, vitamin C and E and so on were significantly reduced.<sup>271–277</sup> These results emphasized the link between oxidative stress and diabetes. In recent years, the development of fluorescent probes provides a promising means of revealing the link between oxidative stress and diabetes pathology.

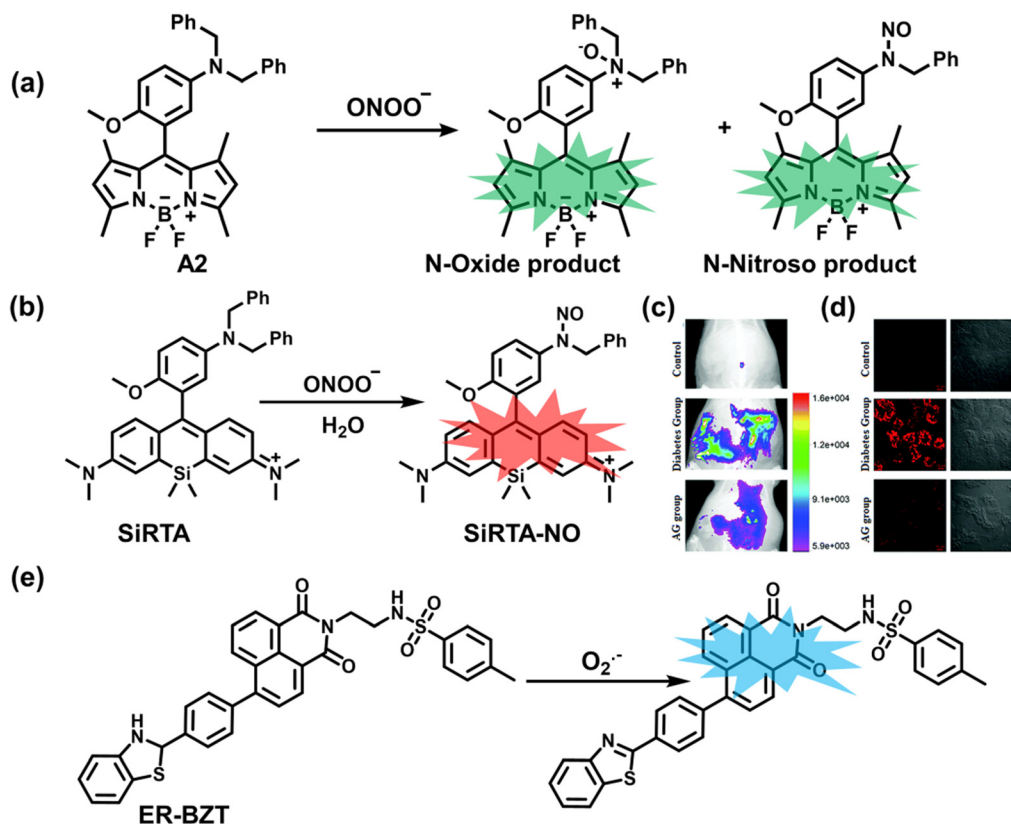
Guo *et al.* in 2016 reported a fluorescent probe (A2), which could be used to visualize the dynamic flux of ONOO<sup>−</sup> in the kidney tissue of diabetic rats.<sup>278</sup> A BODIPY dye was selected as the fluorophore, and 4-methoxy-substituted *N,N*-dibenzylaniline was selected as the specific recognition group for ONOO<sup>−</sup> (Fig. 31(a)). A2 exhibited off-on fluorescence response (within seconds) and exhibited ultrasensitive detection (detection limit: <2 nM). Using A2 endogenous ONOO<sup>−</sup> in RAW264.7 mouse macrophages and oxygen glucose deprivation (OGD) endothelial cells could be visualized. Importantly, the fluorescence intensity of the organs and tissues of the diabetic mouse were significantly higher than for the healthy mouse, which indicated that the concentration of ONOO<sup>−</sup> was higher than the normal level in the kidney tissue of the diabetic mouse. Sadly, the excitation and emission wavelengths of A2 were both in the visible region, which was not conducive to *in vivo* imaging. Therefore, Guo *et al.* subsequently developed a near-infrared fluorescent probe (SiRTA) and achieved ONOO<sup>−</sup> specific imaging of the abdominal

cavity of diabetic mice.<sup>279</sup> SiRTA was obtained by the direct conjugation of a NIR fluorophore Si-rhodamine with an aromatic tertiary amine (Fig. 31(b)). In the presence of ONOO<sup>−</sup>, SiRTA reacts to produce the *N*-nitroso product, thereby rapidly turning on the fluorescence within 30 s due to inhibition of the PeT effect. This research was able to directly monitor high levels of endogenous ONOO<sup>−</sup> in streptozotocin (STZ)-induced pancreatic  $\beta$  cells (INS-1 cells), shedding light on the role of ONOO<sup>−</sup> in the pathophysiological processes of pancreatic  $\beta$  cell death and diabetes (Fig. 31(d)). In addition, SiRTA exhibited an enhanced fluorescence signal in the liver and kidney sections of diabetic mice than in healthy mice (Fig. 31(c)).

Superoxide anion (O<sub>2</sub><sup>•−</sup>) is the first ROS produced in organisms and as such plays an important role in oxidative stress and the pathological process of diabetes. Tang *et al.* designed and synthesized a two-photon fluorescent probe (ER-BZT) targeting the endoplasmic reticulum, which could be used to observe the differences in O<sub>2</sub><sup>•−</sup> levels in healthy/diabetic mice.<sup>280</sup> ER-BZT was comprised of three parts: (i) 1,8-naphthalimide with excellent two-photon properties was selected as the main fluorophore; (ii) benzothiazoline was used as the recognition unit for O<sub>2</sub><sup>•−</sup>; (iii) methyl sulfonamide was chosen as the targeting group for the endoplasmic reticulum (Fig. 31(e)). Spectroscopic analysis indicated that ER-BZT exhibited a low detection limit (60 nM), rapid response time (within a few seconds), and good biocompatibility. Combined with *in vivo* fluorescence imaging, this probe highlighted the abnormally high levels of endogenous O<sub>2</sub><sup>•−</sup> in the abdominal cavity and liver tissue of diabetic mice. The use of the hypoglycemic drug metformin (MERF) resulted in a significant decrease in fluorescence intensity, indicating that the production of O<sub>2</sub><sup>•−</sup> was reduced.

As a metabolite of O<sub>2</sub><sup>•−</sup>, H<sub>2</sub>O<sub>2</sub> is closely associated with the pathological process of diabetes. To explore the relationship between H<sub>2</sub>O<sub>2</sub> and diabetes, Li *et al.* developed a NIR





**Fig. 31** (a) Fluorescence turn 'on' mechanism for A2 in the presence of  $\text{ONOO}^-$ . (b) Fluorescence turn 'on' mechanism for SiRTA in the presence of  $\text{ONOO}^-$ . (c) Fluorescence imaging of  $\text{ONOO}^-$  in the different groups of the peritoneal cavity of rats. AG: the NO synthase inhibitor aminoguanidine. (d) Representative confocal images of the kidney slices of rats in the control group, the diabetic group, and the AG group, respectively. Reproduced with permission from ref. 279. Copyright (2018) The Royal Society of Chemistry. (e) Fluorescence turn 'on' mechanism of ER-BZT in the presence of  $\text{O}_2^{\cdot-}$ .

fluorescent probe (QX-B) based on quinolinium-xanthene dye and benzyl boronic ester recognition group for  $\text{H}_2\text{O}_2$  (Fig. 32(a)).<sup>281</sup> QX-B exhibited high sensitivity and excellent selectivity and could image endogenous  $\text{H}_2\text{O}_2$  in cells and zebrafish (Fig. 32(b)). Furthermore, QX-B was used to monitor abnormally high levels of  $\text{H}_2\text{O}_2$  in the kidney and liver of diabetic mice and used to evaluate the efficacy of the hypoglycemic drug MERF using dynamic changes in the levels of  $\text{H}_2\text{O}_2$  (Fig. 32(c and d)).

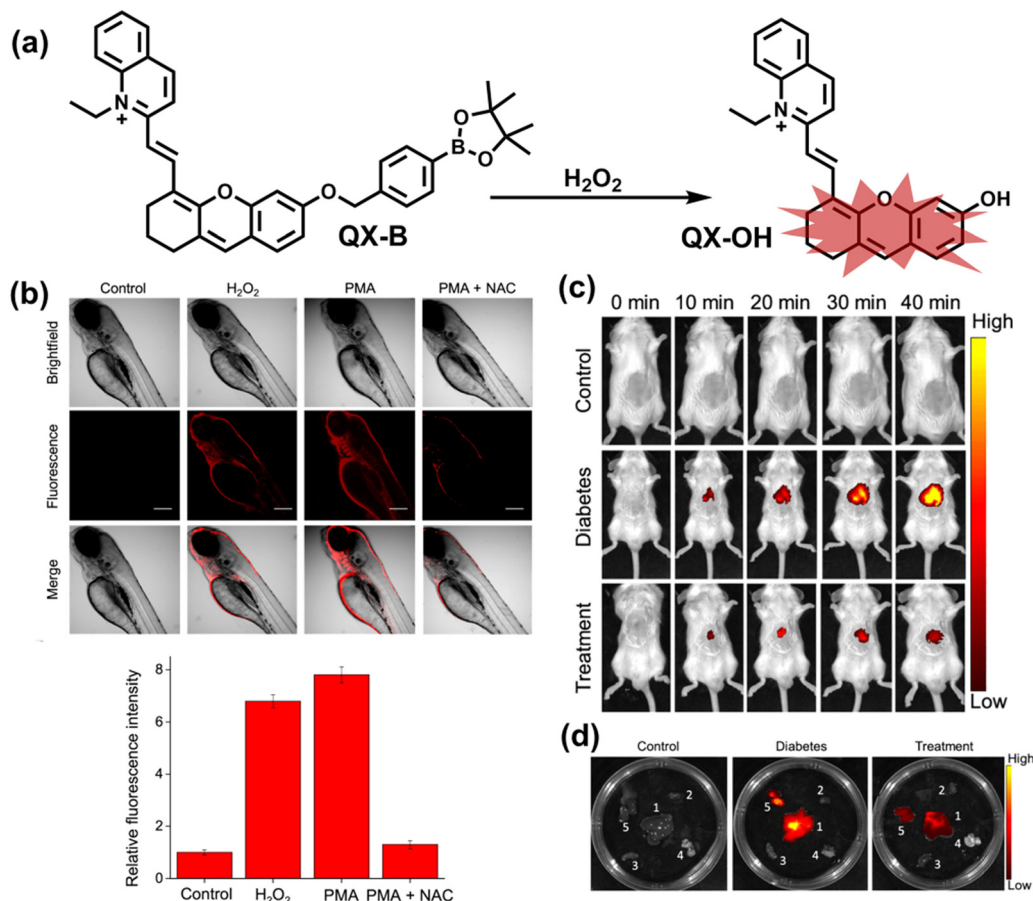
## 5.6 Cancer

Cancer is a ubiquitous fatal disease that threatens human health. Although the rapid diagnosis and treatment of cancer have developed greatly over the past 30 years, the mortality rate associated with cancer has not improved significantly.<sup>282</sup> In recent years, the relationship between oxidative stress and cancer has been given more and more attention. In general, the pathogenesis of cancer is divided into at least three stages: initiation, promotion, and progression.<sup>283</sup> Many studies indicate that oxidative stress can be involved with three stages of the process.<sup>284</sup> At the initial stage, RONS attacks the DNA of the nucleus and mitochondria, leading to nucleoside oxidation and DNA damage. At the promotion stage, RONS induce abnormal gene expression, intercellular communication disruption and oxidative damage to the second messenger system, and then

causes abnormal cell proliferation.<sup>283</sup> Finally, RONS can increase cell proliferation, survival, and migration therefore promoting tumor cell survival and growth.<sup>285</sup> However, due to the limitations of low abundance and short lifespan of RONS, limited of methods exists to observe the oxidative stress of tumors in the clinic. The continuous development of fluorescent probes and dual-mode probes is an area of research that offers significant promise for monitoring highly reactive oxygen species associated with cancer.

Quinone oxidoreductase-1 (NQO1) is a key enzyme whose expression in cancer cells is enhanced when compared to normal cells (5–200 times).<sup>286</sup> As a novel anticancer drug,  $\beta$ -Lap can rapidly produce a large amount of ROS by catalyzing NQO1 to induce cancer cell apoptosis. Guo *et al.* reported a novel near-infrared fluorescent probe (PSiR1) targeting lysosomes, which could image *in vivo* three highly reactive oxygen species (hROS:  $\cdot\text{OH}$ ,  $\text{ONOO}^-$ , and  $\text{ClO}^-$ ) in mouse tumors.<sup>287</sup> PSiR1 was composed of two parts: (i) the silanthracene dye was selected as the fluorophore; (ii) 2,4-dimethyl-3-ethylpyrrole for PeT was used as hROS recognition group (Fig. 33(a)). When hROS were present, PSiR1 reacted to generate *N*-hydroxyl products resulting in rapid fluorescence turn on in a few seconds ( $\lambda_{\text{ex}}/\lambda_{\text{em}} = 650/680 \text{ nm}$ ). This probe was able to image endogenous hROS in cancer cells and indicated that  $\beta$ -Lap could induce hROS production in cellular lysosomes. In addition, Guo *et al.*





**Fig. 32** (a) Fluorescence turn 'on' mechanism of QX-B in the presence of  $\text{H}_2\text{O}_2$ . (b) QX-B was used for fluorescence imaging of endogenous and exogenous hydrogen peroxide in zebrafish. (c) QX-B was used for real-time imaging of hydrogen peroxide in healthy mice, diabetic mice and mice in the treatment group, respectively. (d) Fluorescence imaging in the main organs of the mice. Reproduced with permission from ref. 281. Copyright (2021) American Chemical Society.

developed PSiR3 with a higher signal-to-noise ratio to improve the differentiation between cancer cells and normal tissues.<sup>288</sup> Replacing the  $\text{Me}_2\text{Si}$ -unit of PSiR1 with the  $(\text{Me}_2\text{CH})_2\text{Si}$ -unit, the aggregation induced fluorescence quenching in aqueous solution was partly inhibited (Fig. 33(a)). Using a combination of PSiR3 and  $\beta$ -Lap, high contrast differentiation was achieved for cancer cells/normal cells, and tumor tissues/healthy tissues, respectively (Fig. 33(b and c)). The lung tissue sections and thyroid tissue sections exhibited bright red fluorescence, while healthy tissue exhibited only a weak fluorescence. Notably, the combination of PSiR3 and  $\beta$ -Lap exhibited a weak fluorescent signal in inflammatory tissues, which indicated that the system could effectively distinguish tumor tissue from inflammatory tissue (Fig. 33(c)). These two systems provided an effective protocol for the study of the pathological mechanism of oxidative stress in cancer and the effective differentiation of cancer cells/healthy cells.

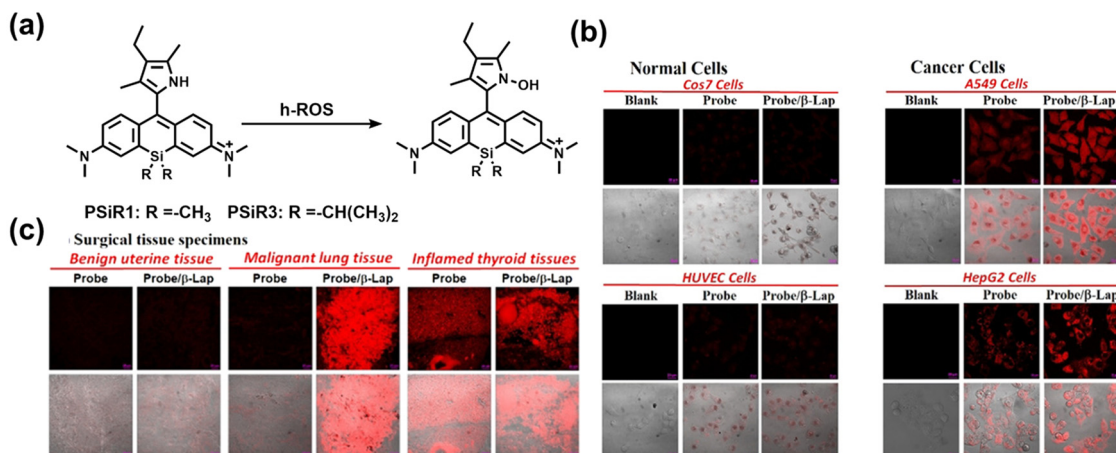
Two-photon fluorescence imaging technology has the advantage of deep tissue imaging, low background fluorescence and high three-dimensional (3D) resolution. Mao *et al.* reported a two-photon near-infrared fluorescent probe (DHQ-RD-PN), which could be used to accurately *in vivo* image  $\text{ONOO}^-$  in

mouse tumors.<sup>289</sup> DHQ-RD-PN was composed of two parts: (i) rhodol was selected as the fluorophore; (ii) the 1-methylindoline-2,3-dione was selected as the recognition site (Fig. 34(a)). Furthermore, 1,4-diethylpiperazine extended the near-infrared emission, and the introduction of the *ortho* F atom to the phenol improved the pH-sensitivity of the rhodol fluorophore. In the presence of  $\text{ONOO}^-$ , the fluorescence intensity of DHQ-RD-PN was significantly increased ( $F/F_0 = 17$ ). Cell imaging experiments indicated that DHQ-RD-PN could specifically detect changes of endogenous  $\text{ONOO}^-$  in drug-stimulated RAW 264.7 cells. Notably, the fluorescence increased with the number of days of tumor growth (Fig. 34(b and c)).

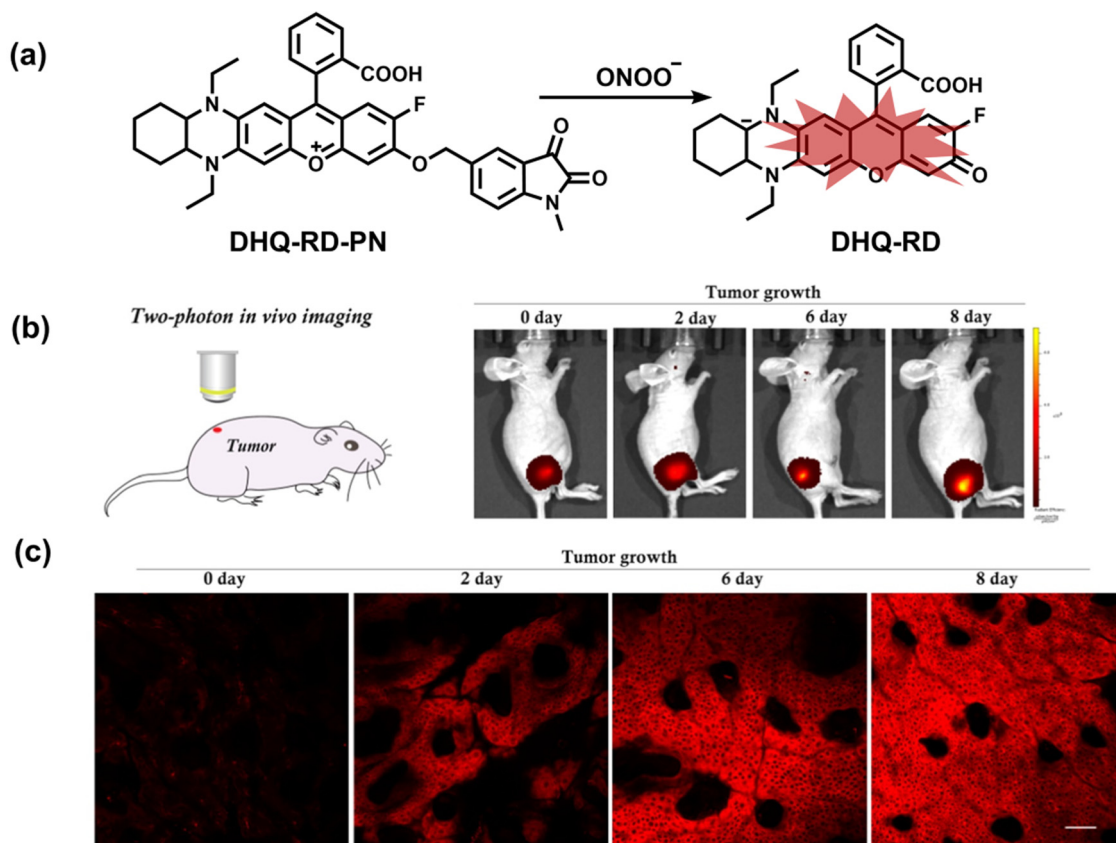
Dual-modal probes combining fluorescence and photoacoustic (PA) measurements result in high spatial and temporal resolution, satisfactory imaging depth and high contrast for optical imaging.<sup>290</sup> Pu *et al.* reported probe ( $\text{CySO}_3\text{CF}_3$ ), using NIR-Fluorescence and PA dual-modal imaging techniques to *in vivo* detect endogenous  $\text{ONOO}^-$  in mouse tumors.<sup>291</sup>  $\text{CySO}_3\text{CF}_3$  was composed of two parts: (i) a caged NIR hemicyanine dye with a zwitterionic structure was used as the host fluorophore; (ii) trifluoromethyl ketone was used as the recognition group (Fig. 35(a)). In the presence of  $\text{ONOO}^-$ , a new







**Fig. 33** (a) Fluorescence turn 'on' mechanism of PSiR1 and PSiR3 in the presence of h-ROS. (b) Confocal fluorescence images of normal cells (COS7 and HUVEC cells) and cancer cells (A549 and HepG2 cells) after co-incubation with PSiR3 (PSiR) and  $\beta$ -Lap. (c) Confocal fluorescence images of the benign uterine tissue sections, malignant lung tissue sections, and inflammatory thyroid tissue sections after co-incubation with PSiR3 (PSiR) and  $\beta$ -Lap. Reproduced with permission from ref. 288. Copyright (2021) Wiley-VCH Verlag GmbH & Co. KGaA, Weinheim.



**Fig. 34** (a) Fluorescence turn 'on' mechanism of DHQ-RD-PN in the presence of ONOO<sup>-</sup>. (b) NIR fluorescence *in vivo* imaging of a tumor-bearing mouse at 0, 2, 6, and 8 days with intratumoral injection of DHQ-RD-PN. (c) Two-photon NIR *in vivo* imaging of a tumor-bearing mouse at 0, 2, 6, and 8 days with intratumoral injection of DHQ-RD-PN. Reproduced with permission from ref. 289. Copyright (2020) American Chemical Society.

absorption peak at 686 nm and new fluorescence emission peak at 712 nm evolved. Meanwhile, the intensity of the PA at 680 nm was 5.1-fold higher than for the initial state. In addition,  $\text{CySO}_3\text{CF}_3$  could accumulate in tumors after tail vein injection.

*In vivo* real-time imaging data indicated that the fluorescence and photoacoustic signal intensity of tumor-bearing mice plateaued within 3 hours, the signal intensity was 2.1-fold and 5.3-fold higher than that of healthy mice, respectively (Fig. 35(b and c)).



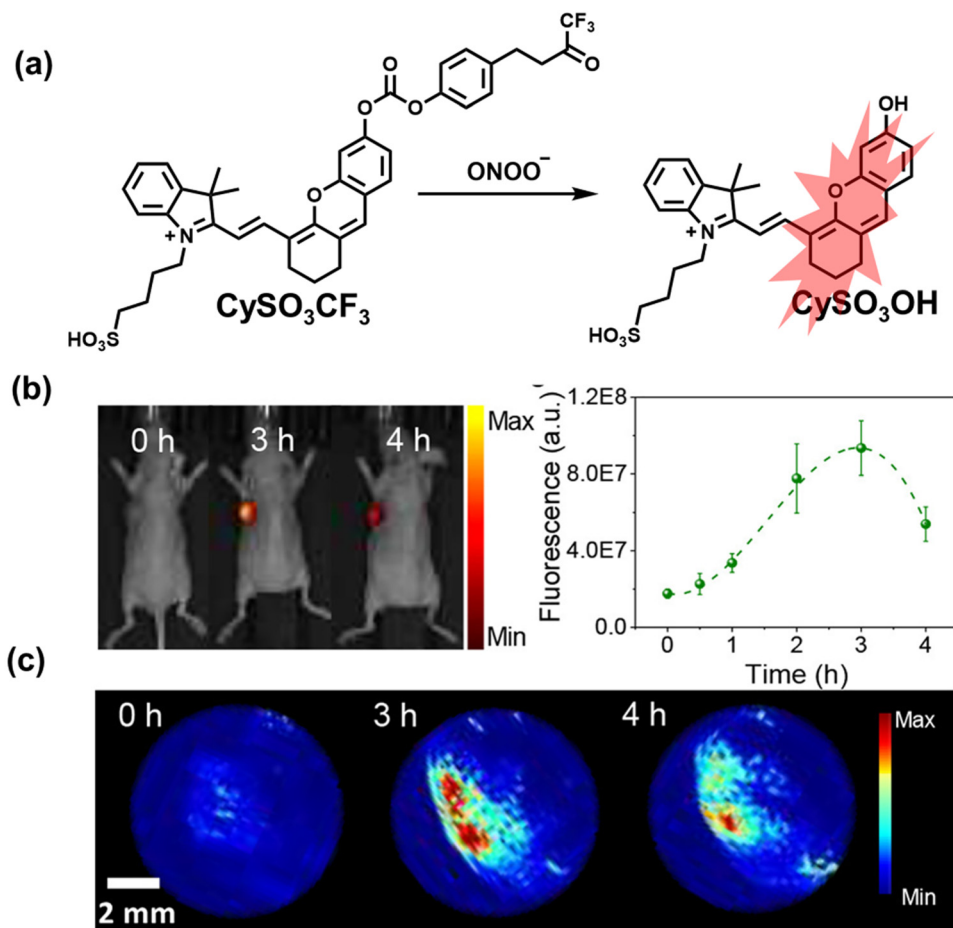


Fig. 35 (a) Fluorescence and PA turn 'on' mechanism of CySO<sub>3</sub>CF<sub>3</sub> in the presence of ONOO<sup>-</sup>. (b) NIR fluorescence *in vivo* imaging of a tumor-bearing mouse at 0, 3 and 4 h with systemic administration of CySO<sub>3</sub>CF<sub>3</sub>. (c) PA maximum imaging projection (MIP) of tumor at 0, 3 and 4 h with systemic administration of CySO<sub>3</sub>CF<sub>3</sub>. Reproduced with permission from ref. 291. Copyright (2018) American Chemical Society.

As the most common ROS in organisms, the specific detection and quantification of H<sub>2</sub>O<sub>2</sub> in tumors is necessary for understanding the relationship between oxidative stress and cancer. Bohndiek *et al.* designed a photoacoustic and fluorescent dual-modal probe (JW41) for detecting H<sub>2</sub>O<sub>2</sub>, that was successfully applied *in vivo* and for tumors.<sup>292</sup> JW41 was composed of three parts: (i) heptamethine carbocyanine dye as the signal transmitter; (ii) benzyl boronic ester connected to the dye backbone through a piperazine linker; (iii) a saccharide which acted as a targeting group for tumors (Fig. 36(a)). In the presence of H<sub>2</sub>O<sub>2</sub>, a significant increase in fluorescence signal at 825 nm was observed, and the photoacoustic emission peak moved from 705 nm to 785 nm (Fig. 36(c)). Real-time fluorescence (Fig. 36(d)) and photoacoustic imaging (Fig. 36(b)) of H<sub>2</sub>O<sub>2</sub> mouse tumors and organs was demonstrated. Moreover, the specific accumulation and retention of JW41 in tumors and liver were confirmed by H&E staining (Fig. 36(e)) and mass spectrometry of tumor tissues (Fig. 36(f)). The total probe concentration in the liver was ~4-fold higher than that in the tumor. The conversion of JW41 into JW35 in mice was calculated to be 36 ± 4% in tumor tissue, while the conversion of in the liver tissue was negligible (3 ± 3%). The data provided

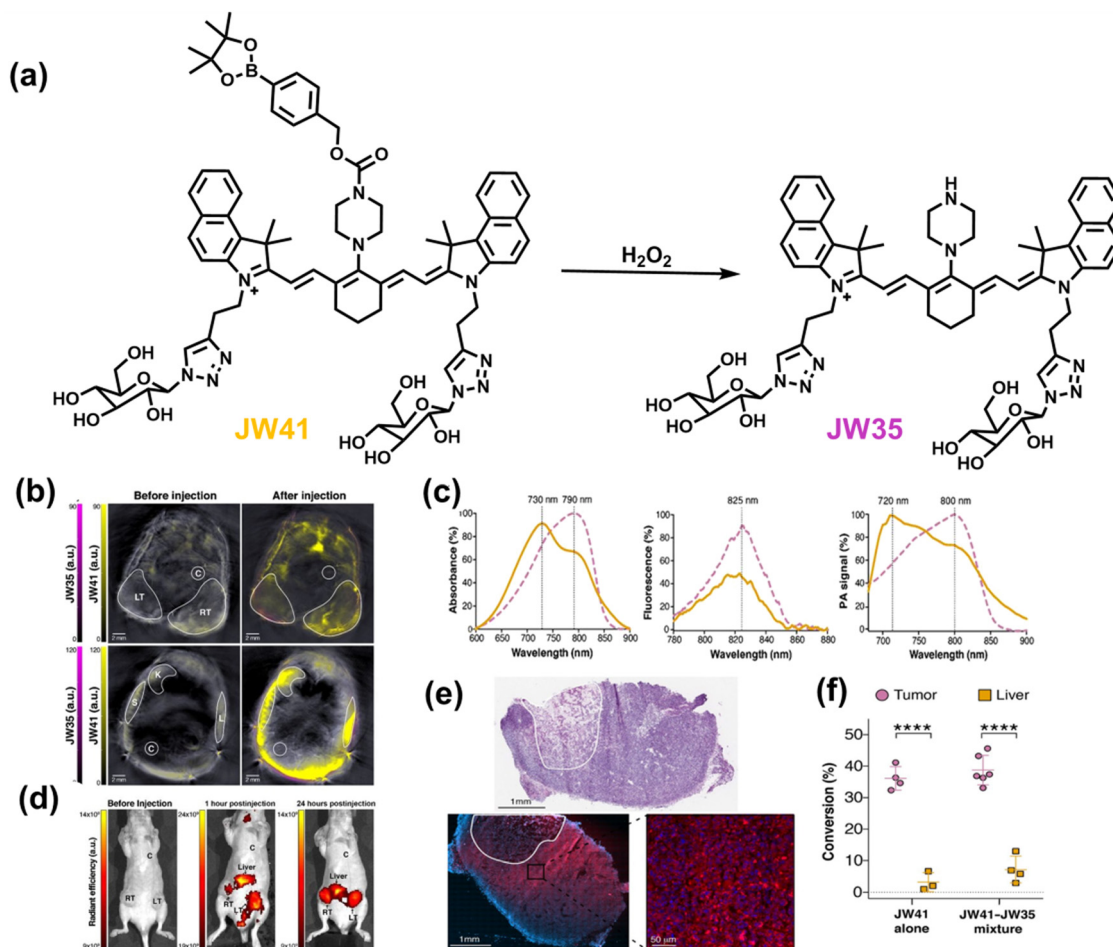
direct evidence for the presence of high levels of H<sub>2</sub>O<sub>2</sub> in tumors (Table 4).

## 6. Conclusion and outlook

Considering that abnormal changes in the levels of oxidants and reductants are an immediate manifestation of oxidative stress, we have delineated the basic structure and design ideas of conventional RONSS fluorescent probes, as well as the need to be alert to problems associated with off-targeting. Furthermore, various fluorescent probes reported over past six years for detecting ROS, RNS and RSS in cells, pathophysiological processes, and diseases models have been comprehensively summarized. According to different applications, the probes introduced in this review are divided into the following categories:

1. Fluorescent probes that simultaneously visualize the dynamic changes between oxidants, reductants, and related active species in cells. As such multi-species imaging can better reflect the dynamic changes of redox in physiological and pathological processes than single-species imaging techniques.
2. Fluorescent probes that are used for RONSS imaging in pathological processes including inflammation, drug-induced





**Fig. 36** (a) Structures of JW41 dye and its reaction with  $\text{H}_2\text{O}_2$ . (b) Representative PAI sections of mouse subcutaneous tumors (top) and liver (bottom) before and 15 to 20 minutes after injection of JW41. (c) Absorption, fluorescence ( $\lambda_{\text{ex}} = 740 \text{ nm}$ ) and photoacoustic spectra of JW41 and JW35 in aqueous solution. (d) Fluorescence images before, 1 and 24 hours post injection of JW41. (e) A representative H&E stained section of a mouse tumor injected with JW41, a serial tumor section (blue) after fixing with formaldehyde and staining with DAPI. The necrotic area is circled with a white line. (f) Quantification of the amount of JW41 present in the tumor and liver converted to JW35 by MRM-MS analysis based on LC/MS-MS (conversion rate, in mol%). Reproduced with permission from ref. 292. Copyright (2019) American Association for Cancer Research.

organ damage and IRI. By monitoring the dynamics of endogenous RONSS during different drug treatments, it is possible to understand the toxicity and therapeutic effects of the drugs. The safety and side effects of some surgical procedures can also be understood by monitoring the outbreak of RONS in different organs induced by IRI.

3. Fluorescent probes that are used for RONSS imaging in specific diseases including AD, PD, epilepsy, depression, diabetes and cancer. Evidence from fluorescence imaging facilitates understanding of the mechanisms of the onset and progression of oxidative stress-related diseases, as well as the therapeutic effects of the drugs used.

Compared with traditional methods used in clinical practice, fluorescent probes can image RONSS as biomarkers, providing researchers with important pathophysiological information related to oxidative stress through non-invasive, highly sensitive and real-time imaging. However, this imaging method is still limited by many factors. Here we summarize some common problems associated with most fluorescent probes:

1. The depth of fluorescence imaging *in vivo* is limited. Although the depth of fluorescence imaging in the near-infrared area is significantly increased, it still cannot meet the needs of clinical detection and imaging.

2. Multi-species detection using a single fluorescent probe remains a challenge. Accommodating two or more recognition groups with opposite/similar reactivity in a single chemical structure are the main challenges for the design of such probes.

3. Most fluorescent probes cannot target specific disease areas. *In situ* injection remains the most effective way for fluorescent probes to reach the diseased area, but this method is impractical for future clinical applications.

4. As tools for biological imaging, current probes are not suitable for in-depth biomedical applications. Since, they have only been used to draw conclusions in similar animal models, for example the association of RONS with peritonitis, arthritis and liver damage.

Considering the rapid development of fluorescent probes in the field of biological imaging in recent years, we end this



**Table 4** Summary of references, chemical structures, maximum absorption/emission wavelengths (TP: two-photon), analytes, detection limit, and application in diseases

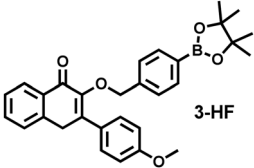
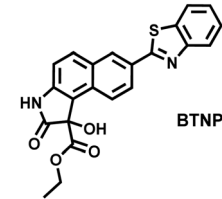
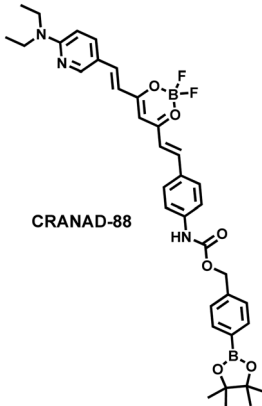
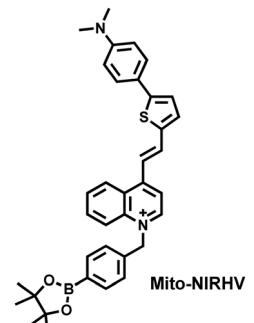
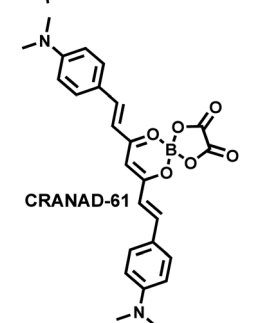
Ref.	Chemical structure	Analyte	Response time	Detection limit ( $\mu\text{M}$ )	$\lambda_{\text{ex}}/\lambda_{\text{em}}$ (nm)	Application in diseases
205		ONOO <sup>−</sup> (A $\beta$ -aggregates) A $\beta$ -Aggregates	— —	0.0655 (variation with A $\beta$ preparation time) —	370/530 370/420	Visualization of A $\beta$ 42 aggregates in AD brain slices using two fluorescence channels in the absence/presence of ONOO <sup>−</sup> .
206		ONOO <sup>−</sup> A $\beta$ -Aggregates	10 s —	— —	380/506 340/418	Visualization of the distribution and variation of A $\beta$ plaques and ONOO <sup>−</sup> through two independent fluorescence channels
207		H <sub>2</sub> O <sub>2</sub> A $\beta$ -Aggregates	10 min —	— —	630/730 640/700	Detection of H <sub>2</sub> O <sub>2</sub> and A $\beta$ aggregates in brain slices and the brains of AD mice
210		H <sub>2</sub> O <sub>2</sub> Viscosity	40 min —	0.003 —	440/700 570/800	Simultaneous imaging of mitochondrial viscosity and hydrogen peroxide in brains of AD mice
211		ROS A $\beta$ -Monomer A $\beta$ -Oligomer A $\beta$ -Aggregates	— — — —	— 0.0032 0.0038 0.0381	675/810 500/570 675/740 675/740	Visualization of high ROS concentrations in AD brains in animal studies at micro- and macrolevels.





Table 4 (continued)

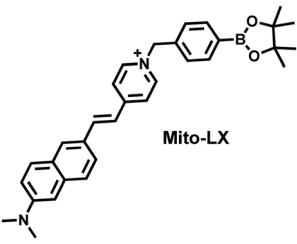
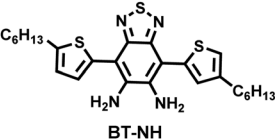
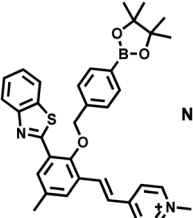
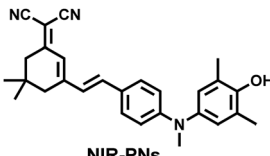
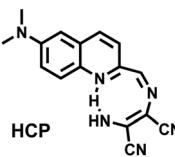
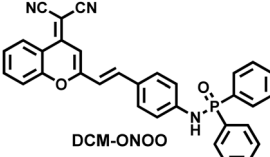
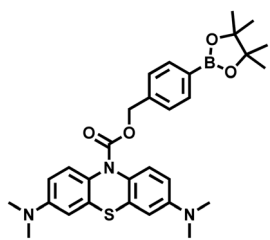
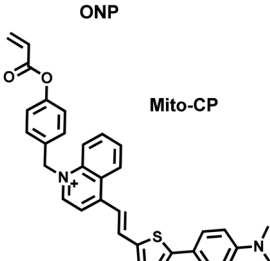
Ref.	Chemical structure	Analyte	Response time	Detection limit ( $\mu\text{M}$ )	$\lambda_{\text{ex}}/\lambda_{\text{em}}$ (nm)	Application in diseases
224	 <b>Mito-LX</b>	$\text{H}_2\text{O}_2$ Viscosity	30 min —	0.00498 —	380/585 TP760/585 480/730 TP800/730	Simultaneous imaging of mitochondrial viscosity and hydrogen peroxide in cells and PD Drosophila brains
225	 <b>BT-NH</b>	NO	5 min	0.00696	525/620	Detection of NO in HepG2 cells and PD drosophila brains
226	 <b>NIR-HP1</b>	$\text{H}_2\text{O}_2$	—	0.27	405/500 405/650	Visualization of the dynamic changes of $\text{H}_2\text{O}_2$ flux in a PD model
228	 <b>NIR-PNs</b>	$\text{ONOO}^-$	A few seconds	0.00459	520/670	Visualization of the dynamic changes of $\text{ONOO}^-$ flux in various PD animal models.
240	 <b>HCP</b>	HClO	5 s	0.104	390/581 TP800/581	Detection of HClO generated by myeloperoxidase (MPO) in the brain of epileptic mice
243	 <b>DCM-ONOO</b>	$\text{ONOO}^-$	10 min	0.151	512/685	Visualization of dynamic changes of the $\text{ONOO}^-$ signal in the brain of epileptic rats
244	 <b>ONP</b>	$\text{ONOO}^-$	15 min	0.094	665/692	Visualization of the dynamic changes of $\text{ONOO}^-$ flux in the epileptic brain of mice and screening of inhibitors
245	 <b>Mito-CP</b>	Cys	15 min	0.0208	440/700	Detection of the dynamic changes of endogenous cysteine levels in the brain of mice with epilepsy



Table 4 (continued)

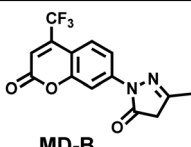
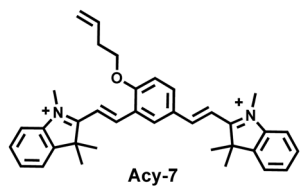
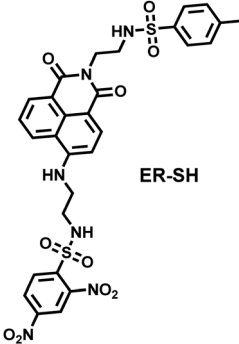
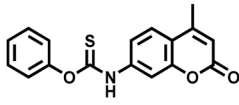
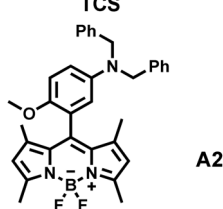
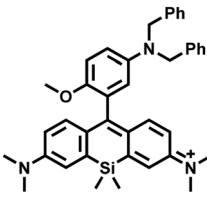
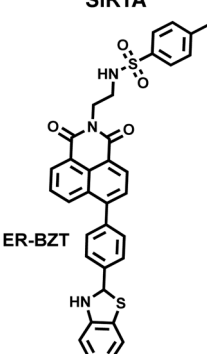
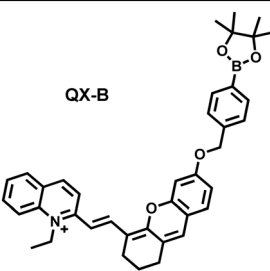
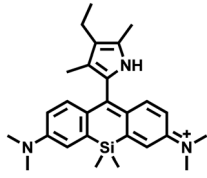
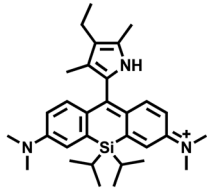
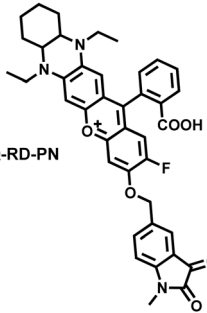
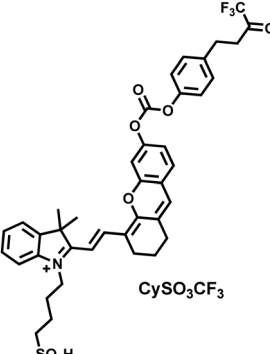
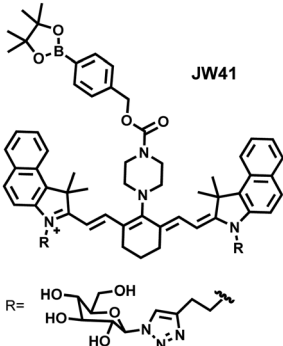
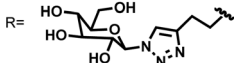
Ref.	Chemical structure	Analyte	Response time	Detection limit ( $\mu\text{M}$ )	$\lambda_{\text{ex}}/\lambda_{\text{em}}$ (nm)	Application in diseases
261	 <b>MD-B</b>	$\cdot\text{OH}$	A few seconds	0.0024	380/500 TP800/500	Visualization of the dynamic changes of $\cdot\text{OH}$ in the brains of depressed mice
264	 <b>Acy-7</b>	$\text{O}_3$	40 min	0.01	570/690	Visualization of the dynamic changes of $\text{O}_3$ in the brains of depressed mice
265	 <b>ER-SH</b>	Thiols Cys Hcy GSH	— — —	0.167 0.962 4.7	420/525 TP800/525	Detection of various thiols in the brains of depressed mice.
266	 <b>TCS</b>	Cys	14 min	0.16	340/443 TP754/443	Visualization of the dynamic changes of Cys in the brains of depressed mice
278	 <b>A2</b>	$\text{ONOO}^-$	A few seconds	0.002	517/485	Visualization of the dynamic flux of $\text{ONOO}^-$ in the kidney tissue of diabetic rats
279	 <b>SiRTA</b>	$\text{ONOO}^-$	20 s	0.003	650/680	Visualization of the dynamic flux of $\text{ONOO}^-$ in the abdominal cavity of diabetic mice and kidney slices
280	 <b>ER-BZT</b>	$\text{O}_2^{\cdot-}$	A few seconds	0.06	375/450 TP700/450	Visualization of abnormally high levels of endogenous $\text{O}_2^{\cdot-}$ in the abdominal cavity and liver tissue of diabetic mice



Table 4 (continued)

Ref.	Chemical structure	Analyte	Response time	Detection limit ( $\mu\text{M}$ )	$\lambda_{\text{ex}}/\lambda_{\text{em}}$ (nm)	Application in diseases
281	 QX-B	$\text{H}_2\text{O}_2$	5 min	0.17	725/772	Visualization of abnormally high levels of $\text{H}_2\text{O}_2$ in the kidney and liver of diabetic mice and evaluate the efficacy of the drug(Merf)
287	 PSiR1	h-ROS $\text{ONOO}^-$ $\bullet\text{OH}$ $\text{HClO}$	A few seconds	0.0079 0.14 0.0106	650/680	Imaging to discriminate cancer cells from normal cells, and tumors from healthy tissues.
288	 PSiR3	h-ROS $\text{ONOO}^-$ $\bullet\text{OH}$ $\text{HClO}$	10 s	0.00539 0.12 0.00686	650/680	Using $\beta$ -Lap, high contrast differentiation was achieved for cancer cells from normal cells, and tumor tissues from healthy tissues,
289	 DHQ-RD-PN	$\text{ONOO}^-$	240 s	0.072	564/651	Visualization of the dynamic flux of $\text{ONOO}^-$ in the in mouse tumors.
291	 CySO <sub>3</sub> CF <sub>3</sub>	$\text{ONOO}^-$	100 s	0.053	686/712	NIRF and photoacoustic dual-modal imaging of $\text{ONOO}^-$ in the tumors of living mice.



Ref.	Chemical structure	Analyte	Response time	Detection limit ( $\mu\text{M}$ )	$\lambda_{\text{ex}}/\lambda_{\text{em}}$ (nm)	Application in diseases
292	 <p><b>JW41</b></p> <p><math>\text{H}_2\text{O}_2</math></p> <p>R = </p>	$\text{H}_2\text{O}_2$	10 min	—	790/825	NIRF and photoacoustic dual-modal imaging of $\text{H}_2\text{O}_2$ in the tumors of living mice.

- 1 H. Sies, C. Berndt and D. P. Jones, *Annu. Rev. Biochem.*, 2017, **86**, 715–748.
- 2 Q. Kong and Cl. G. Lin, *Cell. Mol. Life Sci.*, 2010, **67**, 1817–1829.
- 3 L. H. Sanders and J. T. Greenamyre, *Free Radical Biol. Med.*, 2013, **62**, 111–120.
- 4 D. P. Jones, *Antioxid. Redox Signaling*, 2006, **8**, 1865–1879.
- 5 E. E. Battin and J. L. Brumaghim, *Cell Biochem. Biophys.*, 2009, **55**, 1–23, DOI: [10.1007/s12013-009-9054-7](https://doi.org/10.1007/s12013-009-9054-7).
- 6 G. I. Giles, K. M. Tasker and C. Jacob, *Free Radical Biol. Med.*, 2001, **31**, 1279–1283.
- 7 A. Chandrasekaran, M. D. P. S. Idelchik and J. A. Melendez, *Redox Biol.*, 2017, **11**, 91–102.
- 8 L. C. D. Pomatto and K. J. A. Davies, *Free Radical Biol. Med.*, 2018, **124**, 420–430.



- 9 S. K. Powers, L. L. Ji, A. N. Kavazis and M. J. Jackson, *Compr. Physiol.*, 2011, **1**, 941–969, DOI: [10.1002/cphy.c100054](https://doi.org/10.1002/cphy.c100054).
- 10 Z. Jie, J. Liu, M. Shu, Y. Ying and H. Yang, *Talanta*, 2022, **236**, 122892.
- 11 M. F. Beal, *Curr. Opin. Neurobiol.*, 1996, **6**, 661–666.
- 12 D. C. Malins, N. L. Polissar and S. J. Gunselman, *Proc. Natl. Acad. Sci. U. S. A.*, 1996, **93**, 2557–2563.
- 13 M. Genestra, *Cell. Signaling*, 2007, **19**, 1807–1819.
- 14 L. Lamattina, C. G. Mata, M. Graziano and G. Pagnussat, *Annu. Rev. Plant Biol.*, 2003, **54**, 109–136.
- 15 B. Alvarez and R. Radi, *Amino Acids*, 2003, **25**, 295–311.
- 16 M. C. H. Gruhlke and A. J. Slusarenko, *Plant Physiol. Biochem.*, 2012, **59**, 98–107.
- 17 B. Geng, J. Yang, Y. Qi, J. Zhao, Y. Pang, J. Du and C. Tang, *Biochem. Biophys. Res. Commun.*, 2003, **313**, 362–368.
- 18 T. Mishanina, M. Libiad and R. Banerjee, *Nat. Chem. Biol.*, 2015, **11**, 457–464.
- 19 L. Adams, M. C. Franco and A. G. Estevez, *Exp. Biol. Med.*, 2015, **240**, 711–717.
- 20 P. C. Dedon and S. R. Tannenbaum, *Arch. Biochem. Biophys.*, 2004, **423**, 12–22.
- 21 H. Bayır, *Crit. Care Med.*, 2005, **33**, 498–501.
- 22 D. A. Butterfield and B. Halliwell, *Nat. Rev. Neurosci.*, 2019, **20**, 148–160.
- 23 A. V. Ivanov, B. Bartosch, O. A. Smirnova, M. G. Isagulians and S. N. Kochetkov, *Viruses*, 2013, **5**, 439–469.
- 24 V. Sosa, T. Moliné, R. Somoza, R. Paciucci, H. Kondoh and M. E. LLeonart, *Ageing Res. Rev.*, 2013, **12**, 376–390.
- 25 A. Hald and J. Lotharius, *Exp. Neurol.*, 2005, **193**, 279–290.
- 26 R. Kinscherf, K. Cafaltzis, F. Röder, W. Hildebrandt, L. Edler, H.-P. Deigner, R. Breitreutz, G. Feussner, J. Kreuzer, E. Werle, G. Michel, J. Metz and W. Dröge, *Free Radical Biol. Med.*, 2003, **35**, 1286–1292.
- 27 L. P. Liang and M. Patel, *Redox Biol.*, 2016, **9**, 45–49.
- 28 L. L. Wu, C. C. Chiou, P. Y. Chang and J. T. Wu, *Clin. Chim. Acta*, 2004, **339**, 1–9.
- 29 J. L. Ravanat, P. Guicherd, Z. Tuce and J. Cadet, *Chem. Res. Toxicol.*, 1999, **12**, 802–808.
- 30 J. Frijhoff, P. G. Winyard, N. Zarkovic, S. S. Davies, R. Stocker, D. Cheng, A. R. Knight, E. L. Taylor, J. Oettrich, T. Ruskovska, A. C. Gasparovic, A. Cuadrado, D. Weber, H. E. Poulsen, T. Grune, H. H. H. W. Schmidt and P. Ghezzi, *Antioxid. Redox Signaling*, 2015, **23**, 1144–1170.
- 31 L. Wu, J. Liu, P. Li, B. Tang and T. D. James, *Chem. Soc. Rev.*, 2021, **50**, 702–734.
- 32 J. Yan, S. Lee, A. Zhang and J. Yoon, *Chem. Soc. Rev.*, 2018, **47**, 6900–6916.
- 33 H. B. Cheng, Y. Li, B. Z. Tang and J. Yoon, *Chem. Soc. Rev.*, 2020, **49**, 21–31.
- 34 H. Tian, A. C. Sedgwick, H. H. Han, S. Sen, G. R. Chen, Y. Zang, J. L. Sessler, T. D. James, J. Li and X. P. He, *Coord. Chem. Rev.*, 2021, **427**, 213577.
- 35 L. Wu, C. Huang, B. P. Emery, A. C. Sedgwick, S. D. Bull, X. P. He, H. Tian, J. Yoon, J. L. Sessler and T. D. James, *Chem. Soc. Rev.*, 2020, **49**, 5110–5139.
- 36 Y. Geng, G. Zhang, Y. Chen, Y. Peng, X. Wang and Z. Wang, *Anal. Chem.*, 2022, **94**, 1813–1822.
- 37 X. Jiao, Y. Li, J. Niu, X. Xie, X. Wang and B. Tang, *Anal. Chem.*, 2018, **90**, 533–555.
- 38 X. Jiang, L. Wang, S. L. Carroll, J. Chen, M. C. Wang and J. Wang, *Antioxid. Redox Signaling*, 2018, **29**, 518–540.
- 39 L. Wu, A. C. Sedgwick, X. Sun, S. D. Bull, X. P. He and T. D. James, *Acc. Chem. Res.*, 2019, **52**, 2582–2597.
- 40 X. Chen, X. Tian, I. Shin and J. Yoon, *Chem. Soc. Rev.*, 2011, **40**, 4783–4804.
- 41 D. Wu, A. C. Sedgwick, T. Gunnlaugsson, E. U. Akkaya, J. Yoon and T. D. James, *Chem. Soc. Rev.*, 2017, **46**, 7105–7123.
- 42 J. Hou, K. Yu, K. Sunwoo, W. Y. Kim, S. Koo, J. Wang, W. X. Ren, S. Wang, X. Yu and J. S. Kim, *Chem.*, 2020, **6**, 832–866.
- 43 J. Zhou and H. Ma, *Chem. Sci.*, 2016, **7**, 6309–6315.
- 44 D. J. Zheng, Y. S. Yang and H. L. Zhu, *TrAC, Trends Anal. Chem.*, 2019, **118**, 625–651.
- 45 C. J. Chang, T. D. James, E. J. New and B. Z. Tang, *Acc. Chem. Res.*, 2020, **53**(1), 1.
- 46 L. Wu, A. C. Sedgwick, X. Sun, S. D. Bull, X. P. He and T. D. James, *Acc. Chem. Res.*, 2019, **52**, 2582–2597.
- 47 L. D. Lavis and R. T. Raines, *ACS Chem. Biol.*, 2008, **3**, 142–155.
- 48 L. Wang, W. Du, Z. Hu, K. Uvdal, L. Li and W. Huang, *Angew. Chem., Int. Ed.*, 2019, **131**, 14164–14181.
- 49 X. Chen, T. Pradhan, F. Wang, J. S. Kim and J. Yoon, *Chem. Rev.*, 2012, **112**, 1910–1956.
- 50 A. Mishra, R. K. Behera, P. K. Behera, B. K. Mishra and G. B. Behera, *Chem. Rev.*, 2000, **100**, 1973–2012.
- 51 W. Sun, S. Guo, C. Hu, J. Fan and X. Peng, *Chem. Rev.*, 2016, **116**, 7768–7817.
- 52 C. Sun, W. Du, B. Wang, B. Dong and B. Wang, *BMC Chem.*, 2020, **14**, 21.
- 53 Z. Guo, S. Park, J. Yoon and I. Shin, *Chem. Soc. Rev.*, 2014, **43**, 16–29.
- 54 D. A. Jose, R. Sakla, N. Sharma, S. Gadiyaram, R. Kaushik and A. Ghosh, *ACS Sens.*, 2020, **5**, 3365–3391.
- 55 L. Yuan, W. Lin, S. Zhao, W. Gao, B. Chen, L. He and S. Zhu, *J. Am. Chem. Soc.*, 2012, **134**, 13510–13523.
- 56 V. N. Nguyen, J. Ha, M. Cho, H. Li, K. M. K. Swamy and J. Yoon, *Coord. Chem. Rev.*, 2021, **439**, 213936.
- 57 Z. Shi, X. Han, W. Hu, H. Bai, B. Peng, L. Ji, Q. Fan, L. Li and W. Huang, *Chem. Soc. Rev.*, 2020, **49**, 7533–7567.
- 58 J. Mei, Y. Huang and H. Tian, *ACS Appl. Mater. Interfaces*, 2018, **10**, 12217–12261.
- 59 Y. Wang, B. Xia, Q. Huang, T. Luo, Y. Zhang, P. Timashev, W. Guo, F. Li and X. J. Liang, *Adv. Healthcare Mater.*, 2021, **10**, 2100945.
- 60 K. S. S. Kumar, Y. R. Girish, M. Ashrafizadeh, S. Mirzaei, K. P. Rakesh, M. H. Gholami, A. Zabolian, K. Hushmandi, G. Orive, F. B. Kadumudi, A. D. Pirouz, V. K. Thakur, A. Zarrabi, P. Makvandi and K. S. Rangappa, *Coord. Chem. Rev.*, 2021, **447**, 214135.
- 61 N. L. C. Leung, N. Xie, W. Yuan, Y. Liu, Q. Wu, Q. Peng, Q. Miao, J. W. Y. Lam and B. Z. Tang, *Chem. – Eur. J.*, 2014, **20**, 15349–15353.



- 62 Y. Chen, W. Ai, X. Guo, Y. Li, Y. Ma, L. Chen, H. Zhang, T. Wang, X. Zhang and Z. Wang, *Small*, 2019, **15**, 1902352.
- 63 Y. Ma, W. Ai, J. Huang, L. Ma, Y. Geng, X. Liu, X. Wang, Z. Yang and Z. Wang, *Anal. Chem.*, 2020, **92**, 14444–14451.
- 64 W. Ai, Z. Yang, Y. Ma, X. Han, Y. Chen, K. Zhu and Z. Wang, *Analyst*, 2020, **145**, 6435–6440.
- 65 Y. Ma, H. Wang, S. Su, Y. Chen, Y. Li, X. Wang and Z. Wang, *Analyst*, 2019, **144**, 3381–3388.
- 66 Y. Song, Z. Chen and H. Li, *Curr. Org. Chem.*, 2012, **16**, 2690–2707.
- 67 D. Cao, Z. Liu, P. Verwilt, S. Koo, P. Jangjili, J. S. Kim and W. Lin, *Chem. Rev.*, 2019, **119**, 10403–10519.
- 68 L. Wu, Y. Shi, H. Yu, J. Zhang, Z. Li and X. F. Yang, *Sens. Actuators, B*, 2021, **337**, 129790.
- 69 S. L. Shen, X. Zhao, X. F. Zhang, X. Li Liu, H. Wang, Y. Y. Dai, J. Y. Miaoc and B. X. Zhao, *J. Mater. Chem. B*, 2017, **5**, 289–295.
- 70 Y. Bai, M. X. Wu, Q. J. Ma, C. Y. Wang, J. G. Sun, M. J. Tiana and J. S. Li, *New J. Chem.*, 2019, **43**, 14763–14771.
- 71 C. Geraghty, C. Wynne and R. B. P. Elmes, *Coord. Chem. Rev.*, 2021, **437**, 213713.
- 72 D. Jacquemin, E. A. Perpète, G. Scalmani, I. Ciofini, C. Peltier and C. Adamo, *Chem. Phys.*, 2010, **372**, 61–66.
- 73 H. Q. Dong, T. B. Wei, X. Q. Ma, Q. Y. Yang, Y. F. Zhang, Y. J. Sun, B. B. Shi, H. Yao, Y. M. Zhang and Q. Lin, *J. Mater. Chem. C*, 2020, **8**, 13501–13529.
- 74 H. Zhu, C. Liu, M. Su, X. Rong, Y. Zhang, X. Wang, K. Wang, X. Li, Y. Yu, X. Zhang and B. Zhu, *Coord. Chem. Rev.*, 2021, **448**, 214153.
- 75 L. Zhou, L. Xie, C. Liu and Y. Xiao, *Chin. Chem. Lett.*, 2019, **30**, 1799–1808.
- 76 A. R. Lippert, G. C. Van de Bittner and C. J. Chang, *Acc. Chem. Res.*, 2011, **44**, 793–804.
- 77 Y. Liu, C. Jiao, W. Lu, P. Zhang and Y. Wang, *RSC Adv.*, 2019, **9**, 18027–18041.
- 78 H. Guo, G. Chen, M. Gao, R. Wang, Y. Liu and F. Yu, *Anal. Chem.*, 2019, **91**, 1203–1210.
- 79 M. Abo, Y. Urano, K. Hanaoka, T. Terai, T. Komatsu and T. Nagano, *J. Am. Chem. Soc.*, 2011, **133**, 10629–10637.
- 80 J. F. Turrens, *J. Physiol.*, 2003, **552**, 335–344.
- 81 R. Q. Li, Z. Q. Mao, L. Rong, N. Wu, Q. Lei, J. Y. Zhu, L. Zhuang, X. Z. Zhang and Z. H. Liu, *Biosens. Bioelectron.*, 2017, **87**, 73–80.
- 82 H. Xiao, W. Zhang, P. Li, W. Zhang, X. Wang and B. Tang, *Angew. Chem., Int. Ed.*, 2020, **59**, 4216–4230.
- 83 W. Zhang, P. Li, F. Yang, X. Hu, C. Sun, W. Zhang, D. Chen and B. Tang, *J. Am. Chem. Soc.*, 2013, **135**, 14956–14959.
- 84 H. Maeda, K. Yamamoto, Y. Nomura, I. Kohno, L. Hafsi, N. Ueda, S. Yoshida, M. Fukuda, Y. Fukuyasu, Y. Yamauchi and N. Itoh, *J. Am. Chem. Soc.*, 2005, **127**, 68–69.
- 85 J. J. Hu, N. K. Wong, S. Ye, X. Chen, M. Y. Lu, A. Q. Zhao, Y. Guo, A. C. H. Ma, A. Y. H. Leung, J. Shen and D. Yang, *J. Am. Chem. Soc.*, 2015, **137**, 6837–6843.
- 86 K. Xu, X. Liu, B. Tang, G. Yang, Y. Yang and L. An, *Chem. – Eur. J.*, 2007, **13**, 1411–1416.
- 87 C. C. Winterbourn, *Nat. Chem. Biol.*, 2008, **4**, 278–286.
- 88 J. T. Hou, M. Zhang, Y. Liu, X. Ma, R. Duan, X. Cao, F. Yuan, Y. X. Liao, S. Wang and W. X. Ren, *Coord. Chem. Rev.*, 2020, **421**, 213457.
- 89 L. Yuan, W. Lin and J. Song, *Chem. Commun.*, 2010, **46**, 7930–7932.
- 90 H. Li, X. Li, W. Shi, Y. Xu and H. Ma, *Angew. Chem., Int. Ed.*, 2018, **57**, 12830–12834.
- 91 F. Liu, J. Du, D. Song, M. Xu and G. Sun, *Chem. Commun.*, 2016, **52**, 4636–4639.
- 92 S. Dong, L. Zhang, Y. Lin, C. Ding and C. Lu, *Analyst*, 2020, **145**, 5068–5089.
- 93 J. T. Hou, N. Kwon, S. Wang, B. Wang, X. He, J. Yoon and J. Shen, *Coord. Chem. Rev.*, 2022, **450**, 214232.
- 94 Y. Chen, *Nitric Oxide*, 2020, **98**, 1–19, DOI: [10.1016/j.niox.2020.02.002](https://doi.org/10.1016/j.niox.2020.02.002).
- 95 J. Miao, Y. Huo, X. Lv, Z. Li, H. Cao, H. Shi, Y. Shi and W. Guo, *Biomaterials*, 2016, **78**, 11–19.
- 96 (a) S. Wang, L. Chen, P. Jangili, A. Sharma, W. Li, J. T. Hou, C. Qin, J. Yoon and J. S. Kim, *Coord. Chem. Rev.*, 2018, **374**, 36–54; (b) H. Li, X. Li, X. Wu, W. Shi and H. Ma, *Anal. Chem.*, 2017, **89**, 5519–5525.
- 97 T. Peng, N. K. Wong, X. Chen, Y. K. Chan, D. H. H. Ho, Z. Sun, J. J. Hu, J. Shen, H. E. Nezami and D. Yang, *J. Am. Chem. Soc.*, 2014, **136**, 11728–11734.
- 98 C. Zhao, J. An, L. Zhou, Q. Fei, F. Wang, J. Tan, B. Shi, R. Wang, Z. Guo and W. H. Zhu, *Chem. Commun.*, 2016, **52**, 2075–2078.
- 99 S. Wang, Y. Huang and X. Guan, *Molecules*, 2021, **26**, 3575.
- 100 T. Matsumoto, Y. Urano, T. Shoda, H. Kojima and T. Nagano, *Org. Lett.*, 2007, **9**(17), 3375–3377.
- 101 H. Chen, Y. Tang, M. Ren and W. Lin, *Chem. Sci.*, 2016, **7**, 1896–1903.
- 102 J. Wang, B. Li, W. Zhao, X. Zhang, X. Luo, M. E. Corkins, S. L. Cole, C. Wang, Y. Xiao, X. Bi, Y. Pang, C. A. McElroy, A. J. Bird and Y. Dong, *ACS Sens.*, 2016, **1**, 882–887.
- 103 L. Long, W. Lin, B. Chen, W. Gao and L. Yuan, *Chem. Commun.*, 2011, **47**, 893–895.
- 104 L. Y. Niu, Y. Z. Chen, H. R. Zheng, L. Z. Wu, C. H. Tung and Q. Z. Yang, *Chem. Soc. Rev.*, 2015, **44**, 6143–6160.
- 105 H. Chen, Y. Tang and W. Lin, *TrAC, Trends Anal. Chem.*, 2016, **76**, 166–181.
- 106 J. Liu, Y. Q. Sun, Y. Huo, H. Zhang, L. Wang, P. Zhang, D. Song, Y. Shi and W. Guo, *J. Am. Chem. Soc.*, 2014, **136**, 574–577.
- 107 S. Han, H. Zhang, X. Yue, J. Wang, L. Yang, B. Wang and X. Song, *Anal. Chem.*, 2021, **93**, 10934–10939.
- 108 V. S. Lin, W. Chen, M. Xian and C. J. Chang, *Chem. Soc. Rev.*, 2015, **44**, 4596–4618.
- 109 L. He, X. Yang, K. Xu, X. Kong and W. Lin, *Chem. Sci.*, 2017, **8**, 6257–6265.
- 110 M. Ren, B. Deng, X. Kong, K. Zhou, K. Liu, G. Xua and W. Lin, *Chem. Commun.*, 2016, **52**, 6415–6418.
- 111 Z. Wu, D. Liang and X. Tang, *Anal. Chem.*, 2016, **88**, 9213–9218.
- 112 Q. Wu, C. Yin, Y. Wen, Y. Zhang and F. Huo, *Sens. Actuators, B*, 2019, **288**, 507–511.



- 113 S. Gong, E. Zhou, J. Hong and G. Feng, *Anal. Chem.*, 2019, **91**, 13136–13142.
- 114 M. Qian, L. Zhang, Z. Pu, J. Xia, L. Chen, Y. Xia, H. Cui, J. Wang and X. Peng, *J. Mater. Chem. B*, 2018, **6**, 7916–7925.
- 115 Q. Yang, T. Lan and W. He, *Dyes Pigm.*, 2021, **186**, 108997.
- 116 Y. Fang, W. Chen, W. Shi, H. Li, M. Xian and H. Ma, *Chem. Commun.*, 2017, **53**, 8759–8762.
- 117 Q. Han, Z. Mou, H. Wang, X. Tang, Z. Dong, L. Wang, X. Dong and W. Liu, *Anal. Chem.*, 2016, **88**, 7206–7212.
- 118 H. Zhou, J. Tang, L. Sun, J. Zhang, B. Chen, J. Kan, W. Zhang, J. Zhang and J. Zhou, *Sens. Actuators, B*, 2019, **278**, 64–72.
- 119 Y. Q. Sun, J. Liu, J. Zhang, T. Yang and W. Guo, *Chem. Commun.*, 2013, **49**, 2637–2639.
- 120 Y. Liu, J. Nie, J. Niu, W. Wang and W. Lin, *J. Mater. Chem. B*, 2018, **6**, 1973–1983.
- 121 Q. Sun, W. Zhang and J. Qian, *Talanta*, 2017, **162**, 107–113.
- 122 X. Cheng, H. Jia, J. Feng, J. Qin and Z. Li, *Sens. Actuators, B*, 2013, **184**, 274.
- 123 X. Kong, M. Li, B. Dong, N. Zhang, W. Song, Y. Lua and W. Lin, *Analyst*, 2019, **144**, 4371–4379.
- 124 S. D. Meo, T. T. Reed, P. Venditti and V. M. Victor, *Oxid. Med. Cell. Longevity*, 2016, **2016**, e1245049, DOI: [10.1155/2016/1245049](https://doi.org/10.1155/2016/1245049).
- 125 P. Monostori, G. Wittmann, E. Karg and S. Túri, *J. Chromatogr. B: Anal. Technol. Biomed. Life Sci.*, 2009, **877**, 3331–3346.
- 126 Y. Iwasaki, Y. Saito, Y. Nakano, K. Mochizuki, O. Sakata, R. Ito, K. Saito and H. Nakazawa, *J. Chromatogr. B: Anal. Technol. Biomed. Life Sci.*, 2009, **877**, 3309–3317.
- 127 D. G. Searcy and M. A. Peterson, *Anal. Biochem.*, 2004, **324**, 269–275.
- 128 P. R. Bérubé, P. D. Parkinson and E. R. Hall, *J. Chromatogr. A*, 1999, **830**, 485–489.
- 129 U. Pantke, T. Volk, M. Schmutzler, W. J. Kox, N. Sitte and T. Grune, *Free Radical Biol. Med.*, 1999, **27**, 1080–1086.
- 130 M. Tarvin, B. McCord, K. Mount, K. Sherlach and M. L. Miller, *J. Chromatogr. A*, 2010, **1217**, 7564–7572.
- 131 J. L. Kolanowski, F. Liu and E. J. New, *Chem. Soc. Rev.*, 2018, **47**, 195–208.
- 132 H. Kimura, *Antioxid. Redox Signaling*, 2010, **12**, 1–13, DOI: [10.1089/ars.2009.2919](https://doi.org/10.1089/ars.2009.2919).
- 133 L. Yang, Y. Zhang, X. Ren, B. Wang, Z. Yang, X. Song and W. Wang, *Anal. Chem.*, 2020, **92**, 4387–4394.
- 134 Y. Kimura, Y. Mikami, K. Osumi, M. Tsugane, J. Oka and H. Kimura, *FASEB J.*, 2013, **27**, 2451–2457.
- 135 Y. Huang, F. Yu, J. Wang and L. Chen, *Anal. Chem.*, 2016, **88**, 4122–4129.
- 136 M. Gao, X. Zhang, Y. Wang, Q. Liu, F. Yu, Y. Huang, C. Ding and L. Chen, *Anal. Chem.*, 2019, **91**, 7774–7781.
- 137 Y. Ma, Y. Tang, Y. Zhao and W. Lin, *Anal. Chem.*, 2019, **91**, 10723–10730.
- 138 Y. Zhang, L. Guan, H. Yu, Y. Yan, L. Du, Y. Liu, M. Sun, D. Huang and S. Wang, *Anal. Chem.*, 2016, **88**, 4426–4431.
- 139 A. Kubo, H. Saji, K. Tanaka and N. Kondo, *Plant Mol. Biol.*, 1995, **29**, 479–489.
- 140 K. Dou, Q. Fu, G. Chen, F. Yu, Y. Liu, Z. Cao, G. Li, X. Zhao, L. Xia, L. Chen, H. Wang and J. You, *Biomaterials*, 2017, **133**, 82–93.
- 141 S. C. Lu, *Mol. Aspects Med.*, 2009, **30**, 42.
- 142 A. C. Sedgwick, H. H. Han, J. E. Gardiner, S. D. Bull, X. P. He and T. D. James, *Chem. Sci.*, 2018, **9**, 3672–3676.
- 143 L. Wu, H. H. Han, L. Liu, J. E. Gardiner, A. C. Sedgwick, C. Huang, S. D. Bull, X. P. He and T. D. James, *Chem. Commun.*, 2018, **54**, 11336–11339.
- 144 T. L. Zhu, N. Ren, X. Liu, Y. Dong, R. C. Wang, J. Z. Gao, J. Sun, Y. Zhu, L. H. Wang, C. H. Fan, H. Tian, J. Li and C. C. Zhao, *Angew. Chem., Int. Ed.*, 2021, **60**, 8450–8454.
- 145 S. Lee, E. Y. Tak, J. S. Lee, M. Rashid, M. P. Murphy, J. H. Ha and S. S. Kim, *Cell Res.*, 2011, **21**, 817–834.
- 146 Z. Wu, M. M. Liu, Z. C. Liu and Y. Tian, *J. Am. Chem. Soc.*, 2020, **142**, 7532–7541.
- 147 L. L. Wu, J. H. Liu, X. Tian, R. R. Groleau, B. D. Feng, Y. G. Yang, A. C. Sedgwick, H. H. Han, Y. Wang, H. M. Wang, F. Huang, P. Li, B. Tang, T. D. James and J. L. Sessler, *J. Am. Chem. Soc.*, 2022, **144**, 174–183.
- 148 L. Ferrero-Miliani, O. H. Nielsen, P. S. Andersen and S. E. Girardin, *Clin. Exp. Immunol.*, 2007, **147**, 227–235.
- 149 M. Fioranelli, M. G. Rocca, D. Flavin and L. Cota, *Int. J. Mol. Sci.*, 2021, **22**, 5277.
- 150 G. Y. Chen and G. Nuñez, *Nat. Rev. Immunol.*, 2010, **10**, 826–837.
- 151 N. Chiang, X. D. L. Rosa, S. Libreros, H. Pan, J. M. Dreyfuss and C. N. Serhan, *Proc. Natl. Acad. Sci. U. S. A.*, 2021, **118**, e2013374118.
- 152 (a) A. de Almeida, M. de Almeida Rezende, S. H. Dantas, S. de Lima Silva, J. de Oliveira, F. de Azevedo, R. F. R. Alves, G. de Menezes, P. Santos, T. A. F. Goncalves, V. B. Schini-Kerth and I. de Medeiros, *Oxid. Med. Cell. Longevity*, 2020, **2020**, 1954398, DOI: [10.1155/2020/1954398](https://doi.org/10.1155/2020/1954398); (b) S. K. Biswas, *Oxid. Med. Cell. Longevity*, 2016, **2016**, 5698931, DOI: [10.1155/2016/5698931](https://doi.org/10.1155/2016/5698931).
- 153 G. Y. Chen and G. Nuñez, *Nat. Rev. Immunol.*, 2010, **10**, 826–837.
- 154 S. X. Liu, F. F. Hou, Z. J. Guo, R. Nagai, W. R. Zhang, Z. Q. Liu, Z. M. Zhou, M. Zhou, D. Xie, G. B. Wang and X. Zhang, *Arterioscl. Throm. Vas.*, 2006, **26**, 1156–1162.
- 155 A. Popa-Wagner, S. Mitran, S. Sivanesan, E. Chang and A. M. Buga, *Oxid. Med. Cell. Longevity*, 2013, **2013**, 963520, DOI: [10.1155/2013/963520](https://doi.org/10.1155/2013/963520).
- 156 L. M. Coussens and Z. Werb, *Nature*, 2002, **420**, 860–867.
- 157 S. Tsalamandris, A. S. Antonopoulos, E. Oikonomou, G. A. Papamikroulis, G. Vogiatzi, S. Papaioannou, S. Deftereos and D. Tousoulis, *Eur. Cardiol. Rev.*, 2019, **14**, 50–59.
- 158 J. Huang, U. M. Upadhyay and R. J. Tamargo, *Surg. Neurol.*, 2006, **66**, 232–245.
- 159 P. Libby, *Nature*, 2002, **420**, 868–874.
- 160 Z. G. Song, D. Mao, S. H. P. Sung, R. T. K. Kwork, J. W. Y. Lam, D. Kong, D. Ding and B. Z. Tang, *Adv. Mater.*, 2016, **28**, 7249–7256.
- 161 Y. Z. Chen, X. M. Shi, Z. L. Lu, X. F. Wang and Z. Wang, *Anal. Chem.*, 2017, **89**, 5278–5284.



- 162 X. M. Han, Y. F. Ma, Y. Z. Chen, X. F. Wang and Z. Wang, *Anal. Chem.*, 2020, **92**, 2830–2838.
- 163 M. Weber, H. H. Han, B. H. Li, M. L. Odyneic, C. E. F. Jarman, Y. Zang, S. D. Bull, A. B. Mackenzie, A. C. Sedgwick, J. Li, X. P. He and T. D. James, *Chem. Sci.*, 2020, **11**, 8567–8571.
- 164 L. L. Wu, C. S. Huang, B. P. Emery, A. C. Sedgwick, S. D. Bull, X.-P. He, H. Tian, J. Y. Yoon, J. L. Sessler and T. D. James, *Chem. Soc. Rev.*, 2020, **49**, 5110–5139.
- 165 D. Cheng, Y. Pan, L. Wang, Z. B. Zeng, L. Yuan, X. B. Zhang and Y. T. Chang, *J. Am. Chem. Soc.*, 2017, **139**, 285–292.
- 166 X. X. Chen, X. X. Ren, L. L. Zhang, Z. J. Liu and Z. J. Hai, *Anal. Chem.*, 2020, **92**, 14244–14250.
- 167 X. Zhang, Y. Chen, H. S. He, S. F. Wang, Z. H. Lei and F. Zhang, *Angew. Chem., Int. Ed.*, 2021, **60**, 26337–26341.
- 168 L. He, L. H. He, S. Xu, T. B. Ren, X. X. Zhang, Z. J. Qin, X. B. Zhang and L. Yuan, *Angew. Chem., Int. Ed.*, 2022, **61**, e202211409.
- 169 S. Ogura and T. Shimosawa, *Curr. Hypertens. Rep.*, 2014, **16**, 452–456, DOI: [10.1007/s11906-014-0452-x](https://doi.org/10.1007/s11906-014-0452-x).
- 170 T. Kalogeris, Y. Bao and R. J. Korthuis, *Redox Biol.*, 2014, **2**, 702–714.
- 171 K. Rashid, K. Sinha and P. C. Sil, *Food Chem. Toxicol.*, 2013, **62**, 584–600.
- 172 T. Kalogeris, C. P. Baines, M. Krenz and R. J. Korthuis, *Int. Rev. Cell Mol. Biol.*, 2012, **298**, 229–317.
- 173 A. M. Larson, J. Polson, R. J. Fontana, T. J. Davern, E. Lalani, L. S. Hynan, J. S. Reisch, F. V. Schiødt, G. Ostapowicz, A. O. Shakil and W. M. Lee, *Hepatology*, 2005, **42**, 1364–1372.
- 174 J. Salas, B. Chen, A. Wong, S. Duarte, S. Angarita, G. Lipshutz, O. Witte and P. Clark, *J. Nucl. Med.*, 2018, **59**, 1308–1315.
- 175 N. Foley, S. Marshall, J. Pikul, K. Salter and R. Teasell, *J. Neurotraum.*, 2008, **25**, 1415–1431.
- 176 Y. T. Yang, T. T. Zhou, M. Jin, K. Y. Zhou, D. D. Liu, X. Li, F. J. Huo, W. Li and C. X. Yin, *J. Am. Chem. Soc.*, 2020, **142**, 1614–1620.
- 177 A. Jain, J. Mårtensson, E. Stole, P. A. M. Auld and A. Meister, *Proc. Natl. Acad. Sci. U. S. A.*, 1991, **88**, 1913–1917.
- 178 X. Zhang, Y. Huang, X. Y. Han, Y. Wang, L. W. Zhang and L. Chen, *Anal. Chem.*, 2019, **91**, 14728–14736.
- 179 Y. Zhai, H. Petrowsky, J. C. Hong, R. W. Busuttil and J. W. Kupiec-Weglinski, *Nat. Rev. Gastroenterol. Hepatol.*, 2013, **10**, 79–89.
- 180 X. Y. Han, R. Wang, X. Y. Song, F. B. Yu, C. J. Lv and L. X. Chen, *Biomaterials*, 2018, **156**, 134–146.
- 181 R. F. Xu, Y. Wang, H. Y. You, L. W. Zhang, Y. Q. Wang and L. X. Chen, *Analyst*, 2019, **144**, 2556–2564.
- 182 R. J. Lu, Y. Zhang, F. L. Tang, Z. W. Zheng, Z. D. Fan, S. M. Zhu, X. F. Qian and N. N. Liu, *Exp. Ther. Med.*, 2016, **12**, 2606–2616, DOI: [10.3892/etm.2016.3627](https://doi.org/10.3892/etm.2016.3627).
- 183 J. R. Senior, *Drug Saf.*, 2014, **37**, 9–17, DOI: [10.1007/s40264-014-0182-7](https://doi.org/10.1007/s40264-014-0182-7).
- 184 (a) H. Jaeschke, G. J. Gores, A. I. Cederbaum, J. A. Hinson, D. Pessayre and J. J. Lemasters, *Toxicol. Sci.*, 2002, **65**, 166–176; (b) J. S. Walsh and G. T. Miwa, *Annu. Rev. Pharmacol.*, 2011, **51**, 145–167.
- 185 Z. J. Qin, T. B. Ren, H. J. Zhou, X. X. Zhang, L. He, Z. Li, X. B. Zhang and L. Yuan, *Angew. Chem., Int. Ed.*, 2022, **61**, e202201541, DOI: [10.1002/anie.202201541](https://doi.org/10.1002/anie.202201541).
- 186 L. L. Wu, J. H. Liu, X. Tian, R. R. Groleau, S. D. Bull, P. Li, B. Tang and T. D. James, *Chem. Sci.*, 2021, **12**, 3921–3928.
- 187 X. Y. Jiao, Y. S. Xiao, Y. Li, M. W. Liang, X. L. Xie, X. Wang and B. Tang, *Anal. Chem.*, 2018, **90**, 7510–7516.
- 188 N. Sandhu and V. Navarro, *Hepatol. Commun.*, 2020, **4**, 631–645.
- 189 L. H. Sun, J. Ouyang, Y. Q. Ma, Z. Zeng, C. Zeng, F. Zeng and S. Z. Wu, *Adv. Healthcare Mater.*, 2021, **10**, 2100867.
- 190 D. Sasaki, A. Yamada, H. Umeno, H. Kurihara, S. Nakatsuji, S. Fujihira, K. Tsubota, M. Ono, A. Moriguchi, K. Watanabe and J. Seki, *Biomarkers*, 2011, **16**, 553–566.
- 191 X. L. Wang, J. Lewis, L. Appel, D. Cheek, G. Contreras, M. Faulkner, H. Feldman, J. Gassman, J. Lea, J. Kopple, M. Sika, R. Toto and T. Greene, *J. Am. Soc. Nephrol.*, 2006, **17**, 2900–2909.
- 192 H. W. Liu, H. Y. Zhang, X. F. Lou, L. L. Teng, J. Yuan, L. Yuan, X. B. Zhang and W. H. Tan, *Chem. Commun.*, 2020, **56**, 8103–8106.
- 193 L. Y. Liu, L. P. Jiang, W. Yuan, Z. K. Liu, D. Y. Liu, P. Wei, X. Y. Zhang and T. Yi, *ACS Sens.*, 2020, **5**, 2457–2466.
- 194 A. Wimo, L. Jönsson, J. Bond, M. Prince and B. Winblad, *Alzheimers Dement.*, 2013, **9**, 1–11.
- 195 R. L. Buckner, *Neuron*, 2004, **44**, 195–208.
- 196 J. A. Hardy and G. A. Higgins, *Science*, 1992, **256**, 184–185.
- 197 I. Grundke-Iqbal, K. Iqbal, Y. C. Tung, M. Quinlan, H. M. Wisniewski and L. I. Binder, *Proc. Natl. Acad. Sci. U. S. A.*, 1986, **83**, 4913–4917.
- 198 M. G. Savelieff, G. Nam, J. Kang, H. J. Lee, M. Lee and M. H. Lim, *Chem. Rev.*, 2019, **119**, 1221–1322.
- 199 K. P. Kepp, *Chem. Rev.*, 2012, **112**, 5193–5239.
- 200 D. J. Bonda, H. G. Lee, J. A. Blair, X. W. Zhu, G. Perry and M. A. Smith, *Metallomics*, 2011, **3**, 267–270.
- 201 C. Behl, J. B. Davis, R. Lesley and D. Schubert, *Cell*, 1994, **77**, 817–827.
- 202 H. M. Abdul, R. Sultana, J. N. Keller, D. K. S. Clair, W. R. Markesbery and D. A. Butterfield, *J. Neurochem.*, 2006, **96**, 1322–1335.
- 203 M. A. Deibel, W. D. Ehmann and W. R. Markesbery, *J. Neurol. Sci.*, 1996, **143**, 137–142.
- 204 K. M. Boje and P. K. Arora, *Brain Res.*, 1992, **587**, 250–256.
- 205 A. C. Sedgwick, W. T. Dou, J. B. Jiao, L. L. Wu, G. T. Williams, A. T. A. Jenkins, S. D. Bull, J. L. Sessler, X. P. He and T. D. James, *J. Am. Chem. Soc.*, 2018, **140**, 14267–14271.
- 206 X. L. Xie, G. Z. Liu, Y. X. Niu, C. H. Xu, Y. Li, J. Zhang, X. Y. Jiao, X. Wang and B. Tang, *Anal. Chem.*, 2021, **93**, 15088–15095.
- 207 J. Yang, J. Yang, S. H. Liang, Y. G. Xu, A. Moore and C. Z. Ran, *Sci. Rep.*, 2016, **6**, 35613.
- 208 A. M. Aleardi, G. Benard, O. Augereau, M. Malgat, J. C. Talbot, J. P. Mazat, T. Letellier, J. Dachary-Prigent,





- G. C. Solaini and R. J. Rossignol, *J. Bioenerg. Biomembr.*, 2005, **37**, 207–225, DOI: [10.1007/s10863-005-6631-3](#).
- 209 A. Bobba, G. Amadoro, D. Valenti, V. Corsetti, R. Lassandro and A. Atlante, *Mitochondrion*, 2013, **13**, 298–311.
- 210 S. J. Li, P. P. Wang, W. Q. Feng, Y. H. Xiang, K. Dou and Z. H. Liu, *Chem. Commun.*, 2020, **56**, 1050–1053.
- 211 J. Yang, X. L. Zhang, P. Yuan, J. Yang, Y. G. Xu, J. Grutzendler, Y. H. Shao, A. Moore and C. Z. Ran, *Proc. Natl. Acad. Sci. U. S. A.*, 2017, **114**, 12384–12389.
- 212 A. I. Bush and R. E. Tanzi, *Neurotherapeutics*, 2008, **5**, 421–432.
- 213 L. V. Kalia and A. E. Lang, *Lancet*, 2015, **386**, 896–912.
- 214 Y. H. Fu, G. Paxinos, C. Watson and G. M. Halliday, *J. Chem. Neuroanat.*, 2016, **76**, 98–107, DOI: [10.1016/j.jchemneu.2016.02.001](#).
- 215 A. Yoritaka, N. Hattori, K. Uchida, M. Tanaka, E. R. Stadtman and Y. Mizuno, *Proc. Natl. Acad. Sci. U. S. A.*, 1996, **93**, 2696–2701.
- 216 E. Floor and M. G. Wetzels, *J. Neurochem.*, 1998, **70**, 268–275.
- 217 D. T. Dexter, C. J. Carter, F. R. Wells, F. Javoy-Agid, Y. Agid, A. Lees, P. Jenner and C. D. Marsden, *J. Neurochem.*, 1989, **52**, 381–389.
- 218 Z. I. Alam, A. Jenner, S. E. Daniel, A. J. Lees, N. Cairns, C. D. Marsden, P. Jenner and B. Halliwell, *J. Neurochem.*, 1997, **69**, 1196–1203.
- 219 J. Zhang, G. Perry, M. A. Smith, D. Robertson, S. J. Olson, D. G. Graham and T. J. Montine, *Am. J. Pathol.*, 1999, **154**, 1423–1429.
- 220 J. Sian, D. T. Dexter, A. J. Lees, S. Daniel, Y. Agid, F. Javoy-Agid, P. Jenner and C. D. Marsden, *Ann. Neurol.*, 1994, **36**, 348–355.
- 221 J. R. Richardson, Y. Quan, T. B. Sherer, J. T. Greenamyre and G. W. Miller, *Toxicol. Sci.*, 2005, **88**, 193–201.
- 222 J. Callio, T. D. Oury and C. T. Chu, *J. Biol. Chem.*, 2005, **280**, 18536–18542.
- 223 A. Navarro and A. Boveris, *Front. Aging Neurosci.*, 2010, **2**, 34, DOI: [10.3389/fnagi.2010.00034](#).
- 224 H. Li, C. Xin, G. Zhang, X. Han, C. Yu, L. Li and W. Huang, *J. Mater. Chem. B*, 2019, **7**, 4243–4251.
- 225 M. Weng, X. Yang, Y. Ni, C. Xu, H. Zhang, J. Shao, C. Zhang and L. Li, *Sens. Actuators, B*, 2019, **283**, 769–775.
- 226 Y. Liu, L. Bei, Y. Li, C. Xin, C. Zhang, J. Liu, Z. Liu, L. Li and W. Huang, *Sens. Actuators, B*, 2019, **279**, 38–43.
- 227 H. C. Cubukcu, M. Yurtdas, Z. E. Durak, B. Aytac, H. N. Gunes, B. G. Cokal, T. K. Yoldas and I. Durak, *Neurol. Sci.*, 2016, **37**, 1793–1798.
- 228 Q. Sun, J. Xu, C. Ji, Z. Li, K. Lim, C. Zhang, L. Li and Z. Liu, *Anal. Chem.*, 2020, **92**, 4038–4045.
- 229 C. C. T. Aguiar, A. B. Almeida, P. V. P. Araújo, R. N. D. C. Abreu, E. M. C. Chaves and O. C. Vale, *Oxid. Med. Cell. Longevity*, 2012, **2012**, 12, DOI: [10.1155/2012/795259](#).
- 230 S. D. Shorvon, *Epilepsia*, 2011, **52**, 1052–1057.
- 231 A. K. Ngugi, C. Bottomley, I. Kleinschmidt, J. W. Sander and C. R. Newton, *Epilepsia*, 2010, **51**, 883–890.
- 232 E. J. Shin, J. H. Jeong, Y. H. Chung, W. K. Kim, K. H. Ko, J. H. Bach, J. S. Hong, Y. Yoneda and H. C. Kim, *Neurochem. Int.*, 2011, **59**, 122–137.
- 233 M. Patel, L. Liang and L. J. Roberts, *J. Neurochem.*, 2001, **79**, 1065–1069.
- 234 E. Candelario-Jalil, H. H. Ajamieh, S. Sam, G. Martínez and O. S. León Fernández, *Eur. J. Pharmacol.*, 2000, **390**, 295–298.
- 235 L. P. Liang, Y. Ho and M. Patel, *Neuroscience*, 2000, **101**, 563–570.
- 236 M. Patel, *Free Radical Biol. Med.*, 2004, **37**, 1951–1962.
- 237 L. P. Liang and M. Patel, *Free Radical Biol. Med.*, 2006, **40**, 316–322.
- 238 L. P. Liang and M. Patel, *Free Radical Biol. Med.*, 2004, **36**, 542–554.
- 239 Y. Zhang, D. P. Seeburg, B. Pulli, G. R. Wojtkiewicz, L. Bure, W. Atkinson, S. Schob, Y. Iwamoto, M. Ali, W. Zhang, E. Rodriguez, A. Milewski, E. J. Keliher, C. Wang, Y. Pan, F. K. Swirski and J. W. Chen, *Radiology*, 2016, **278**, 822–830.
- 240 C. W. Shao, J. W. Yuan, Y. N. Liu, Y. J. Qin, X. A. Wang, J. Gu, J. Zhao, H. L. Zhu and Y. Qian, *Proc. Natl. Acad. Sci. U. S. A.*, 2020, **117**, 10155–10164.
- 241 J. Feng, X. Chen, B. Guan, C. Li, J. Qiu and J. Shen, *Mol. Neurobiol.*, 2018, **55**, 6369–6386.
- 242 Y. C. Chuang, S. D. Chen, C. W. Liou, T. K. Lin, W. N. Chang, S. H. Chan and A. Y. Chang, *Epilepsia*, 2009, **50**, 731–746.
- 243 X. Luo, Z. Cheng, R. Wang and F. Yu, *Anal. Chem.*, 2021, **93**, 2490–2499.
- 244 J. S. Hu, C. Shao, X. Wang, X. Di, X. Xue, Z. Su, J. Zhao, H. L. Zhu, H. K. Liu and Y. Qian, *Adv. Sci.*, 2019, **6**, 1900341.
- 245 S. Li, D. Song, W. Huang, Z. Li and Z. Liu, *Anal. Chem.*, 2020, **92**, 2802–2808.
- 246 (a) H. P. Kapfhammer, *Dialogues. Clin. Neuro.*, 2006, **8**, 227–239, DOI: [10.31887/DCNS.2006.8.2/hpkapfhammer](#); (b) C. Mulholland and S. Cooper, *Adv. Psychiatr. Treat.*, 2000, **6**, 169–177, DOI: [10.1192/apt.6.3.169](#).
- 247 (a) B. Harerimana, C. Forchuk and T. O'Regan, *Int. J. Mental. Health. Nurs.*, 2019, **28**, 657–670; (b) M. J. Knol, J. W. R. Twisk, A. T. F. Beekman, R. J. Heine, F. J. Snoek and F. Pouwer, *Diabetol.*, 2006, **49**, 837–845.
- 248 M. D. Cabana, J. L. Rushton and A. J. Rush, *Gen. Hosp. Psychiatry*, 2022, **24**, 35–42.
- 249 E. A. Phelps and J. E. LeDoux, *Neuron*, 2005, **48**, 175–187.
- 250 V. Krishnan and E. J. Nestler, *Nature*, 2008, **455**, 894–902.
- 251 E. J. Nestler, M. Barrot, R. J. Dileone, A. J. Eisch, S. J. Gold and L. M. Monteggia, *Neuron*, 2002, **34**, 13–25.
- 252 M. Maes, P. Galecki, Y. S. Chang and M. Berk, *Prog. Neuropsychopharmacol. Biol. Psychiatry*, 2011, **35**, 676–692.
- 253 M. Maes, I. Mihaylova, M. Kubera, M. Uytterhoeven, N. Vrydags and E. Bosmans, *J. Affective Disord.*, 2010, **125**, 287–294.
- 254 T. M. Michel, S. Camara, T. Tatschner, S. Frangou, A. J. Sheldrick, P. Riederer and E. Grunblatt, *World J. Biol. Psychiatry*, 2010, **11**, 314–320.
- 255 M. Maes, N. D. Vos, R. Pioli, P. Demedts, A. Wauters, H. Neels and A. Christophe, *J. Affective Disord.*, 2000, **58**, 241–246.



- 256 J. Kodydková, L. Vávrová, M. Zeman, R. Jiráček, J. Macásek and B. Stanková, *Clin. Biochem.*, 2009, **42**, 1368–1374.
- 257 M. Maes, I. Mihaylova, M. Kubera, M. Uytterhoeven, N. Vrydags and E. Bosmans, *Neuroendocrinol. Lett.*, 2009, **30**, 470–476.
- 258 A. C. Andreazza, F. Kapczinski, M. Kauer-Sant'Anna, J. C. Walz, D. J. Bond, C. A. Gonçalves and L. N. Yatham, *J. Psychiatry Neurosci.*, 2009, **34**, 263–271.
- 259 R. Edwards, M. Peet, J. Shay and D. Horrobin, *J. Affective Disord.*, 1998, **48**, 149–155.
- 260 M. J. Forlenza and G. E. Miller, *Psychosom. Med.*, 2006, **68**, 1–7.
- 261 X. Wang, P. Li, Q. Ding, C. Wu, W. Zhang and B. Tang, *Angew. Chem., Int. Ed.*, 2019, **58**, 4674–4678.
- 262 B. C. Dickinson and C. J. Chang, *Nat. Chem. Biol.*, 2011, **7**, 504–511.
- 263 J. C. Chen and J. M. Samet, *Eur. J. Epidemiol.*, 2017, **32**, 943–946.
- 264 P. Li, J. Wang, X. Wang, Q. Ding, X. Bai, Y. Zhang, D. Su, W. Zhang, W. Zhang and B. Tang, *Chem. Sci.*, 2019, **10**, 2805–2810.
- 265 P. Li, X. Shi, H. Xiao, Q. Ding, X. Bai, C. Wu, W. Zhang and B. Tang, *Analyst*, 2019, **144**, 191–196.
- 266 Y. Zhang, X. Wang, X. Bai, P. Li, D. Su, W. Zhang, W. Zhang and B. Tang, *Anal. Chem.*, 2019, **91**, 8591–8594.
- 267 M. J. Fowler, *Clin. Diabetes Res.*, 2008, **26**, 77–82, DOI: [10.2337/diaclin.26.2.77](https://doi.org/10.2337/diaclin.26.2.77).
- 268 U. Asmat, K. Abad and K. Ismail, *Saudi Pharm. J.*, 2016, **24**, 547–553.
- 269 M. Halim and A. Halim, *Diabetes Metab. Syndr.*, 2019, **13**, 1165–1172, DOI: [10.1016/j.dsx.2019.01.040](https://doi.org/10.1016/j.dsx.2019.01.040).
- 270 A. C. Maritim, R. A. Sanders and J. B. Watkins, *J. Biochem. Mol. Toxicol.*, 2003, **17**, 24–38, DOI: [10.1002/jbt.10058](https://doi.org/10.1002/jbt.10058).
- 271 L. A. Pham-Huy, H. He and C. Pham-Huy, *Int. J. Biomed. Sci.*, 2008, **4**, 89–96.
- 272 J. L. Figarola, S. Scott, S. Loera, C. Tessler, P. Chu, L. Weiss, J. Hardy and S. Rahbar, *Diabetologia*, 2003, **46**, 1140–1152, DOI: [10.1007/s00125-003-1162-0](https://doi.org/10.1007/s00125-003-1162-0).
- 273 D. Prabakaran and N. Ashokkumar, *Biochimie*, 2013, **95**, 366–373.
- 274 K. S. Park, J. H. Kim, M. S. Kim, J. M. Kim, S. K. Kim, J. Y. Choi, M. H. Chung, B. Han, S. Y. Kim and H. K. Lee, *Diabetes*, 2001, **50**, 2837–2841.
- 275 R. V. Sekhar, S. V. McKay, S. G. Patel, A. P. Guthikonda, V. T. Reddy, A. Balasubramanyam and F. Jahoor, *Diabetes Care*, 2010, **34**, 162–167, DOI: [10.2337/dc10-1006](https://doi.org/10.2337/dc10-1006).
- 276 A. R. Smith, S. V. Shenvi, M. Widlansky, J. H. Suh and T. M. Hagen, *Curr. Med. Chem.*, 2004, **11**, 1135–1146.
- 277 F. Sun, K. Iwaguchi, R. Shudo, Y. Nagaki, K. Tanaka, K. Ikeda, S. Tokumaru and S. Kojo, *Clin. Sci.*, 1999, **96**, 185–190, DOI: [10.1042/cs0960185](https://doi.org/10.1042/cs0960185).
- 278 J. Miao, Y. Huo, Q. Liu, Z. Li, H. Shi, Y. Shi and W. Guo, *Biomaterials*, 2016, **107**, 33–43.
- 279 J. Miao, Y. Huo, H. Shi, J. Fang, J. Wang and W. Guo, *J. Mater. Chem. B*, 2018, **6**, 4466–4473.
- 280 H. Xiao, X. Liu, C. Wu, Y. Wu, P. Li, X. Guo and B. Tang, *Biosens. Bioelectron.*, 2017, **91**, 449–455.
- 281 W. X. Wang, W. L. Jiang, G. J. Mao, M. Tan, J. Fei, Y. Li and C. Y. Li, *Anal. Chem.*, 2021, **93**, 3301–3307.
- 282 A. Jemal, R. Siegel, J. Xu and E. Ward, *CA-Cancer J. Clin.*, 2010, **60**, 277–300, DOI: [10.3322/caac.20073](https://doi.org/10.3322/caac.20073).
- 283 S. Reuter, S. C. Gupta, M. M. Chaturvedi and B. B. Aggarwal, *Free Radical Biol. Med.*, 2010, **49**, 1603–1616.
- 284 J. D. Hayes, A. T. Dinkova-Kostova and K. D. Tew, *Cancer Cell*, 2020, **38**, 167–197.
- 285 T. Kamata, *Cancer Sci.*, 2009, **100**, 1382–1388.
- 286 S. Danson, T. H. Ward, J. Butler and M. Ranson, *Cancer Treat. Rev.*, 2004, **30**, 437–449.
- 287 H. Zhang, J. Liu, C. Liu, P. Yu, M. Sun, X. Yan, J. Guo and W. Guo, *Biomaterials*, 2017, **133**, 60–69.
- 288 J. Liu, M. Liu, H. Zhang and W. Guo, *Angew. Chem., Int. Ed.*, 2021, **60**, 12992–12998.
- 289 W. Wang, J. Xiong, X. Song, Z. Wang, F. Zhang and Z. Mao, *Anal. Chem.*, 2020, **92**, 13305–13312.
- 290 V. Ntziachristos, *Nat. Methods*, 2010, **7**, 603–614.
- 291 J. Zhang, X. Zhen, J. Zeng and K. Pu, *Anal. Chem.*, 2018, **90**, 9301–9307.
- 292 J. Weber, L. Bollepalli, A. M. Belenguer, M. D. Antonio, N. D. Mitri, J. Joseph, S. Balasubramanian, C. A. Hunter and S. E. Bohndiek, *Cancer Res.*, 2019, **79**, 5407–5417.

